eMetN
METEOR JOURNAL

eJournal for meteor observers   **www.emetn.net**

All-sky radiant maps from six full years of CAMS meteor video observations that are color coded by meteoroid orbital element show that some orbital elements have a very organized distribution of values across the sky resulting in well-defined color zones. Here a close up is shown with radiants in Sun-centered geocentric ecliptic coordinates, color coded in function of the perihelion distance q. Read more about this interesting study page 205 in this issue (credit: David Holman).

- All-Sky distribution orbital elements
- 51-Sagittids
- Outburst of iota-Herculids
- Meteor showers needing attention
- CARMELO status report
- CAMS reports
- SWEMN fireball reports
- Radio meteor observations

Contents

The All-Sky distribution of meteoroid orbital elements

David Holman[1], Peter Jenniskens[1,2]

[1] **International Meteor Organization**
daveh@lmi.net

[2] **SETI Institute, 339 Bernardo Ave, Mountain View, CA 94043, USA**

Radiant maps that display meteor direction and speed at a given time in the year also map the orbital elements of the meteoroid. Here, we present a number of all-sky radiant maps from six full years of CAMS meteor video observations that are color coded by meteoroid orbital element. The plots show that some orbital elements have a very organized distribution of values across the sky resulting in well-defined color zones, as these are mostly determined by the radiant position, while the elements that are determined mostly by speed tend to show a mixed distribution of values and colors. Because both Apex and Anthelion sources have mostly a limited range in speed, the use of D criteria does not always easily define a shower among the nearby sporadic background.

1   Introduction

When viewing meteor radiant maps like those in Jenniskens (2023), or those shown on the CAMS website[1], it is rarely appreciated how the location of a radiant on the sky is diagnostic of the orbit of the meteoroid. That is because the maps are for a limited period of time in the year and the range of speed is fairly limited for meteors arriving from a given direction.

The time, direction and speed at which a meteoroid enters Earth's atmosphere are typically expressed as solar longitude (which determines the position of Earth around the Sun), the Right Ascension and Declination of the radiant, and the Speed. From that, the six Keplerian orbital elements of a meteoroid are calculated: the perihelion distance q (AU), semi-major axis a (AU), eccentricity e, inclination i (°), argument of perihelion ω (°), and node Ω (°), where a, e and q are related according to $q = a\,(1 - e)$.

Derivative parameters include the Öpik parameters U, ϕ (°), and cosine θ, the longitude of perihelion Π (°) $= \omega + \Omega$, and the Tisserand parameter with respect to Jupiter T_J.

Others have plotted full annual activity in equal area plots, usually mapped with a v_g color scale. Examples include the back covers of WGN by Molau and Rendtel (2009) and SonotaCo (2009). Also plots by Koukal (2016) and Koukal et al., (2024) which appeared in eMetN.

Here, we will show how to read radiant maps by showing how the orbital elements change for different directions in the sky over the course of the full year. We will show a series of all-sky plots of radiants in Sun-centered ecliptic longitude and ecliptic latitude, with orbital element values color coded.

2   Methods

The maps display the data in the CAMS Meteoroid Orbit Database v3.0[2] (Jenniskens et al., 2018). The database runs until the end of 2016, while much more data was taken in recent years that cover the southern hemisphere better. However, every single triangulation in this earlier data set was manually verified.

The maps were created using a newly developed MATLAB script which makes all-sky, all-year plots with nearly equal x and y axis scales in a cylindrical projection. The plot axes are in Sun-centered ecliptic longitude ("longitude") and ecliptic latitude ("latitude"). Each radiant marker is plotted in a color corresponding to the element value of that radiant, and the element values are mapped to the MATLAB 'turbo' color map.

A second MATLAB script creates an interactive version of each plot that was used to check for obscured data in dense clusters, determine local means and variance, and to identify the elements of radiants that appear "out of zone", i.e., a different color than the background. While the plots show a full year of activity at once, each element was examined with plots of a 20° solar longitude period that were advanced 5° at a time producing a 72 frame "movie" to check for possible zone changes during the year.

3   Keplerian element distributions

Figures 1–11 show these orbital element distributions.

The CAMS low-light video observations show the main source directions: the northern and southern halves of the Apex, the Antapex, the Anthelion, and the Toroidal ring.

---

[1] http://cams.seti.org/FDL

[2] http://cams.seti.org/CAMS-v3-2010to2016.xlsx

The Helion, southeastern quadrant of the Apex, and southern and western Antapex are not as well observed because the dataset is based on observations to the end of 2016 and does not include results from the southern hemisphere expansion in recent years. The corresponding maps of more recent video data, and radar data, are shown in Jenniskens (2023, p.128 and p.130, respectively).

Other interesting features include a void of radiants in the Apex source near the ecliptic plane. The lack of data in this region is not an observational artifact, but due to a real lack of meteoroid orbits in the ecliptic plane from planetary perturbations.

There is also a lack of radiants between the Apex source and Toroidal sources, in a region surrounding the Apex source. Here, this empty region will be referred to as the "transition region", split as the eastern and western transition regions. The western transition region is well observed by CAMS while the eastern transition region suffers from daylight.

Geocentric velocity, v_g:
The map of the distribution of speed (here expressed as the geocentric velocity v_g) over the sky is shown as *Figure 1*. As one would expect, the fastest meteors are hitting the Earth head on in the direction of the Apex, while the slowest meteors are catching up on Earth in the direction of the Antapex. The velocities in between are mostly found towards the Anthelion, Toroidal ring and the poles. Because the geocentric velocity is a combination of the meteoroid velocity vector and the speed and direction of Earth, the map of *Figure 1* shows that shower and sporadic meteor velocity is dependent on what part of the sky the meteor arrives from.

Perihelion distance, q:
This orbital element is mostly determined by the radiant direction. *Figure 2* shows that the q distribution appears to emanate from the east and west transition regions, centered at 320° longitude/0° latitude and 220° longitude/0° latitude respectively. Starting from those locations with the smallest q (0 AU, red), perihelion distance increases in all directions until the largest q (1.05 AU, violet) is reached at the center of the Apex (270° longitude) and Antapex (90° longitude). The changes in q increase along relatively straight lines resulting in strong gradients and well-defined color zones. High q orbits are narrowly concentrated at the Apex and much broader at the Antapex because q increases more rapidly approaching the Apex than approaching the Antapex directions.

Notice that all shower clusters blend into the surrounding color zones, or have a similar shade within that zone. The radiants that do not blend into the background color are scattered over the Apex and extend past the northern Toroidal source, but not all the way to the pole. While less data is shown in the southern hemisphere, it is assumed to have the same distribution of these "Out of Zone Radiant(s)" (OZR) as the north. The western Anthelion and Antapex are devoid of OZR. There also appears to be a hole in the scattered OZR that coincides with the northern Toroidal source. These OZR may not be visible in the plots shown here without enlarging the view.

The interactive script revealed that these scattered OZR share high T_J parameters of ~4.3 to ~9.6 by a sample of 14 radiants from all over the Apex. All OZR appear to be in asteroid-like orbits among the otherwise dominant population of Jupiter-family comet and long-period comet orbits. However, some are in Sun-grazer comet orbits like those around the east and west transition regions.
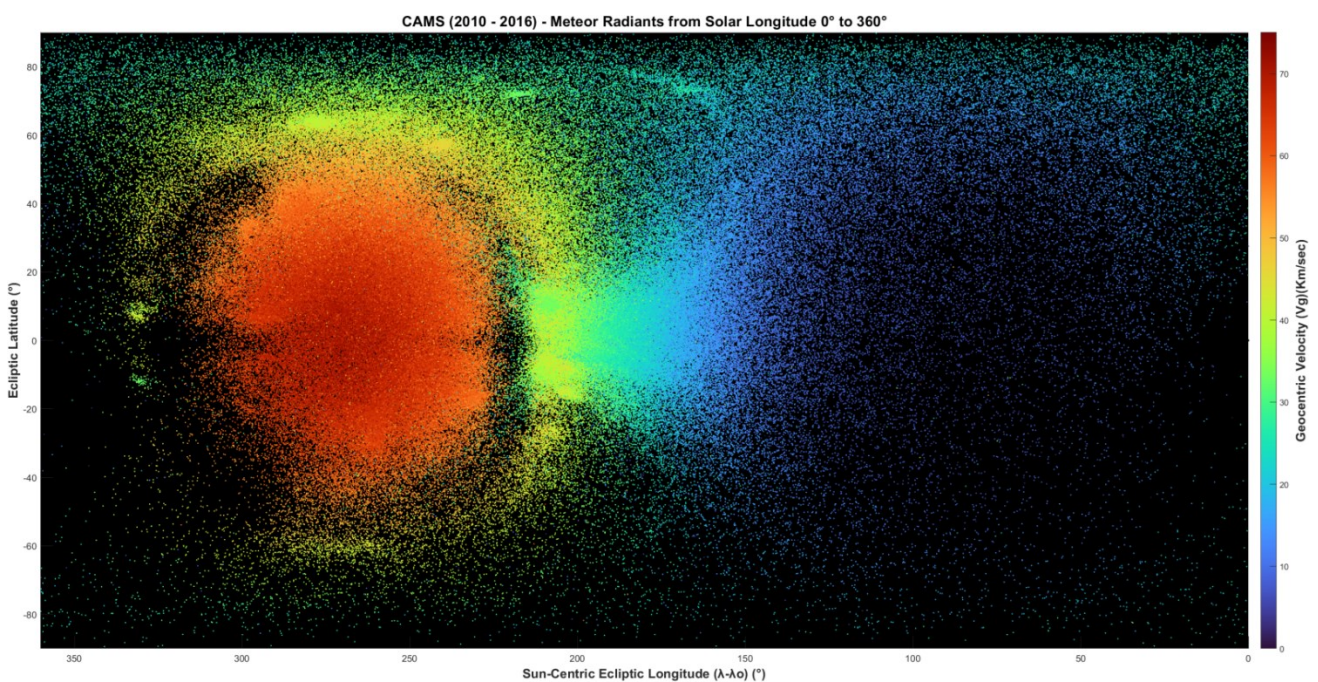

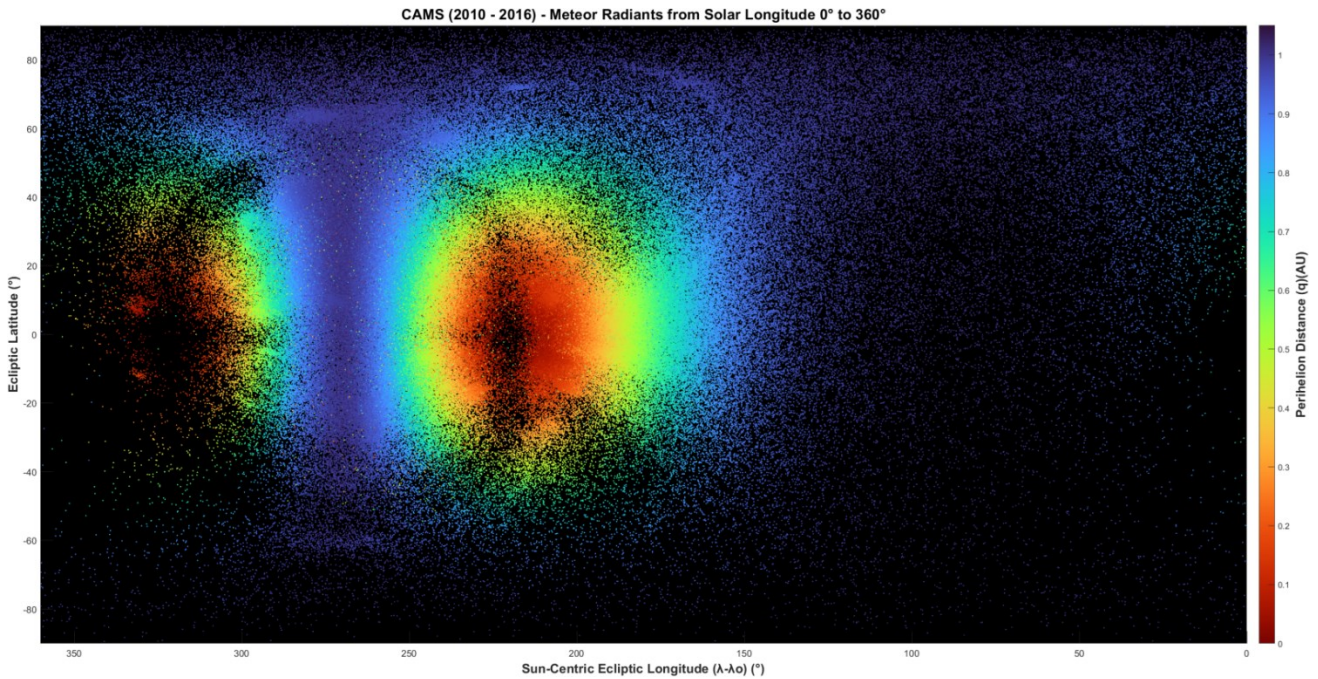*Figure 1* – Geocentric velocity v_g (and Öpik vector magnitude U).
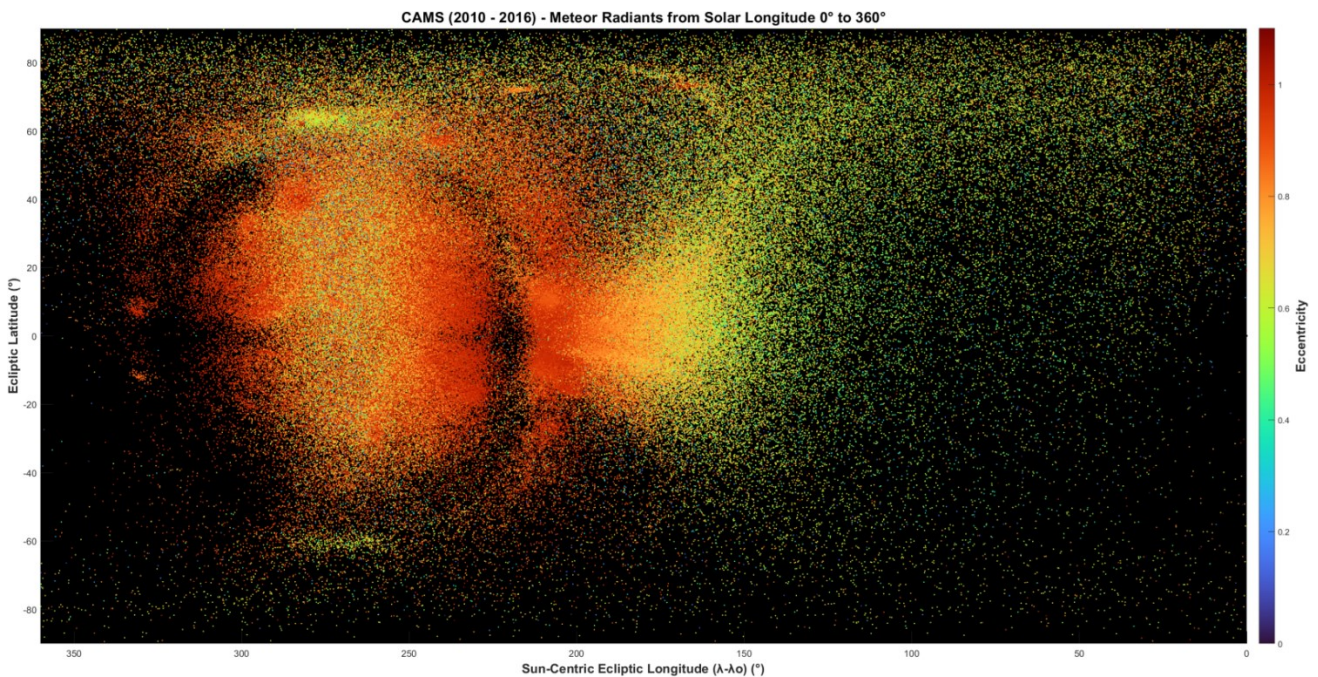
Figure 2 – Perihelion distance *q*.

Figure 3 – Eccentricity *e*.

Eccentricity, *e*:

Figure 3 shows that the *e* distribution is much less organized than *q* and much of the distribution is mixed because this parameter strongly depends on the measured speed. The most obvious structure is the concentration of high eccentricities approaching or exceeding (due to measurement error) the value of *e* = 1.0 around the east and west transition regions, and up and down the Toroidal ring. The strongest gradients lead out of these regions, but break down quickly into a scattered distribution, especially approaching the Apex. The north and south Toroidal sources have distinct high *e* ~0.7 that stand out from the background, as does the western Anthelion source.

The Anthelion source meteoroids change eccentricity from the highest *e* (> 0.8) in the east to lower *e* (0.35 – 0.80) in the west as it becomes more diffuse in latitude approaching the Antapex. The Antapex is likewise dominated by 0.35 < *e* < 0.80, with few *e* < 0.35 and fewer *e* > 0.80.

A distribution of radiants resembling the Narrow Apex source in radar data (Jenniskens, 2023, p. 89) is seen when *e* is restricted to lower values (*Figure 4*) and the lower *e* is restricted, the narrower the Apex. Empirical measurements of the Apex width (W_E) at the ecliptic were made from plots (not shown here) for *e* thresholds in increments of 0.10. The results suggest that from $0.0 \leq e \leq 0.7$ the least squares fit is linear,

$$W_E\ (°) = -3.07 + 64.33 e_{max} \tag{1}$$

and that for $0.7 \leq e \leq 1.1$ the least squares fit is exponential,

$$W_E (°) = 6.24 * \ln(2.69 e_{max}) \qquad (2)$$

where W_E is the width of radiants at the ecliptic in degrees, e_{max} is the threshold for eccentricity, and the system limiting magnitude is ~5.5. Both fit equations have high reliability $R > 0.99$ over their ranges.

Semi-major axis, *a*:

The semi-major axis is defined by speed also, even more so than the eccentricity. *Figure 5* shows the distribution of *a*

scaled from 0 AU to 10 AU. Like *e*, semi-major axis *a* is largely mixed, with a concentration of low-*a* orbits at the Anthelion side of the western transition region. The rest of the Anthelion is also composed of low *a* orbits, but somewhat higher than the low-*a* orbits at the transition region. This low-*a* trend continues moving west through the Antapex and Helion. The Apex and Toroidal ring are noticeably both composed of orbits with longer semi-major axes, but also contain a mix of the low-*a* orbits. The Toroidal sources both stand out from the Toroidal ring with low-*a* orbits. Some shower radiant clusters do stand out from the mixed background.

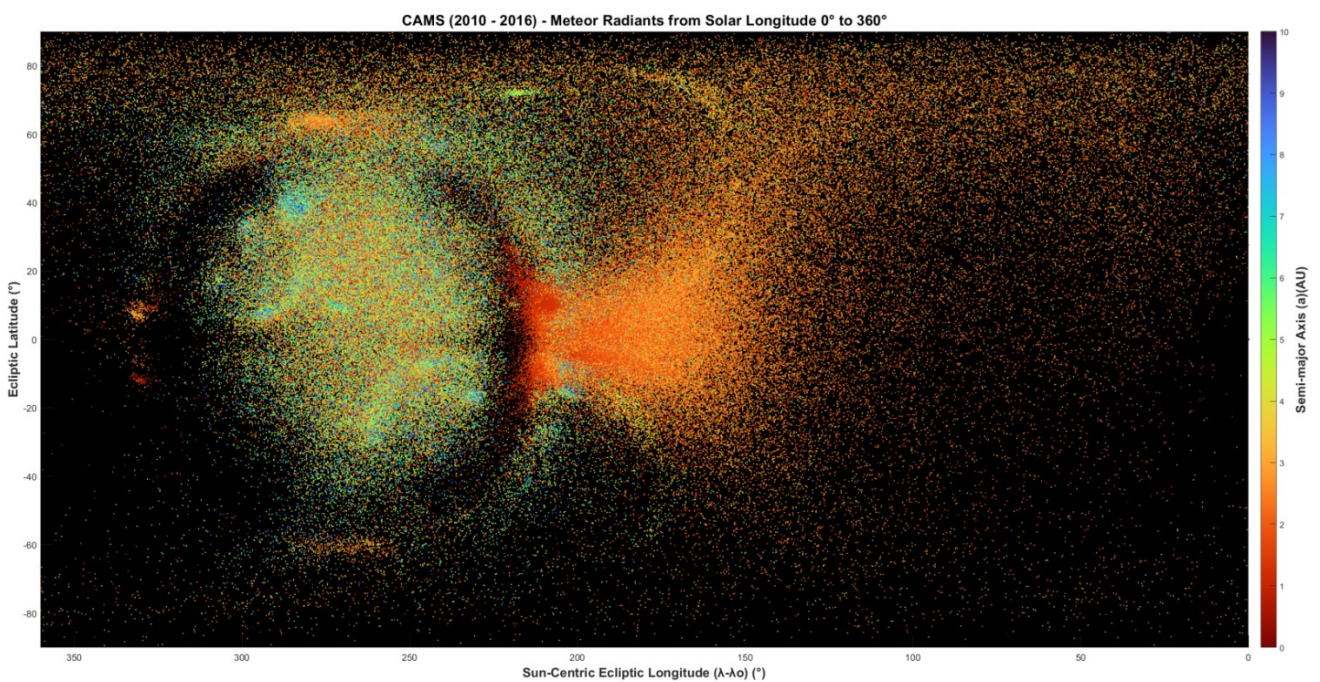*Figure 4* – Narrow Apex Source seen for *e* < 0.50. Colors show T_J parameters.

Figure 5 – Semi-major axis, *a*, from 0–10 AU.
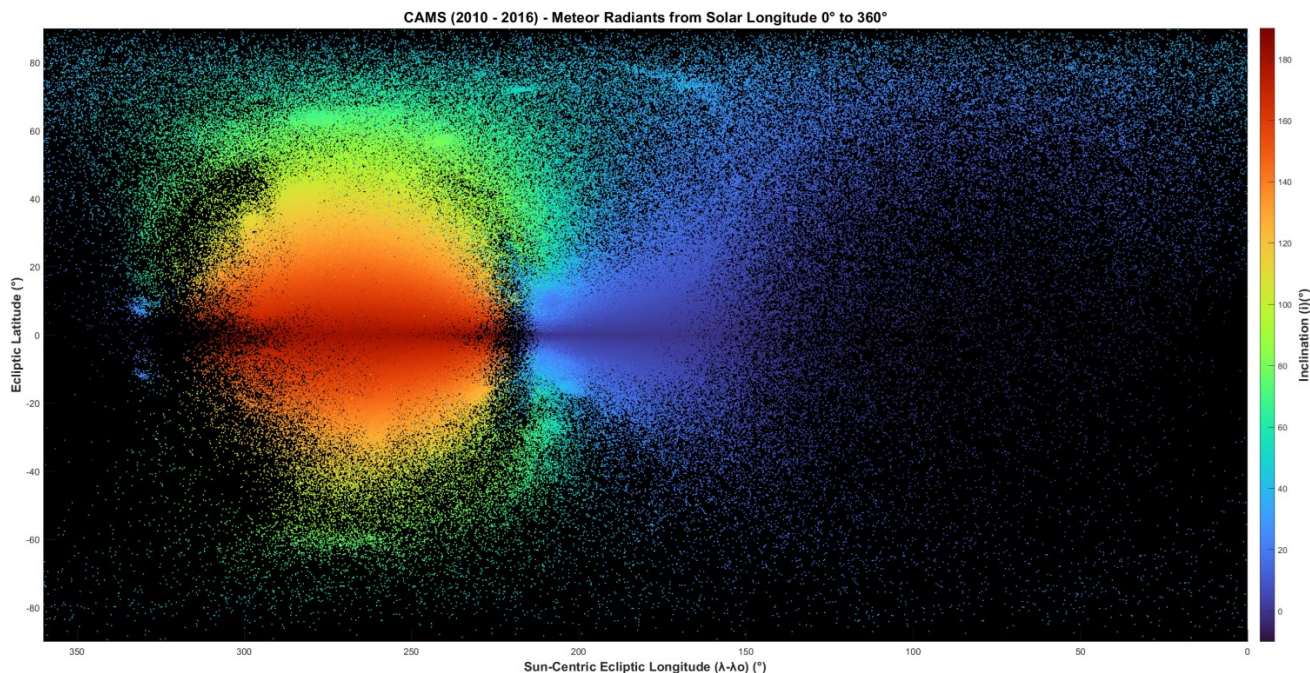
Figure 6 – Inclination *i*. The scale has been extended beyond 0°–180° to make the low *i* radiants easier to see.

Inclination, *i*:

Figure 6 shows that the distribution of *i* is quite organized like that of *q*, but with a different structure symmetrical about the ecliptic plane. Like *q*, the gradients are strong and the color zones are well defined. Shower clusters and the background both blend together in the color zones, with some small deviations like towards the Geminid radiant at around 210° longitude, +10° latitude.

High retrograde ($i > 90°$) orbits are centered on the Apex, and low prograde ($i < 90°$) orbits are centered on the Antapex source. All retrograde orbits are confined to the Apex, arriving in a cone with a base diameter of ~110°, centered at 270° longitude and 0° latitude, the Apex of the Earth's way. This boundary is in the transition region, just inside the Toroidal ring. The rest of the sky and sources are prograde, with a thin scattering of prograde radiants among the retrograde radiants in the Apex.

Where the Anthelion meets the Toroidal ring the mean value of *i* increases rapidly moving up or down the ring, and levels off around $i \approx 72°$ at about ±40° latitude. The OZRs seen in the western transition region are all sungrazers with mixed T_J and *i*, and with *e* close to or slightly over $e = 1$.

Some OZR are seen in the Apex and in the western transition zone. The Apex OZR are the same as those seen in *q* with high T_J, but in the western transition region the T_J parameters are much lower, less than 4.0 in general, and even less than zero in some cases. Notice that, given the way the color zones are structured for *i*, all colors meet at the ecliptic in the eastern and western transition regions. The inclinations of radiants located there can take on a wide array of values.

Argument of perihelion, ω:

The argument of perihelion shown in *Figure 7* also has a distribution that is organized although with an abrupt 180° flip at the ecliptic. The flip at the ecliptic occurs because the ascending node shifts 180° when crossing the ecliptic plane. The argument of perihelion is measured from the ascending nodal point of the nodal line, so when the ascending node shifts by 180°, so does ω. The abrupt vertical changes at 270° and 90° from red to blue and back in the southern hemisphere are actually smooth changes from 360° to 0°.

Orbits approach $\omega = 0°/360°$ in the northern transition regions, decreasing to 0° on the eastern side, and increasing to 360° on the western side. The 180° flip in the southern hemisphere means that in the southern transition regions orbits approach $\omega = 180°$ from above on the eastern side and from below on the western side. Orbits approach $\omega = 180°$ at the North Pole and $\omega = 0°/360°$ at the South Pole.

No showers stand out against these color zones, not even the Geminids. Elongated shower radiant clusters change ω according to the color zone they pass through. Only the OZRs seen against the Apex source in *Figure 2* stand out against the background.

Longitude of perihelion, *Π*:

By itself, a plot of the ascending node *Ω* is not very informative, but when added to ω to make *Π* some things are revealed, because now showers at different times in the year are separated (*Figure 8*). While there are no well-defined color zones, individual shower clusters stand out in various colors against the thoroughly mixed background of the Anthelion and poles. The Antapex is also thoroughly mixed, but has no visible shower clusters.
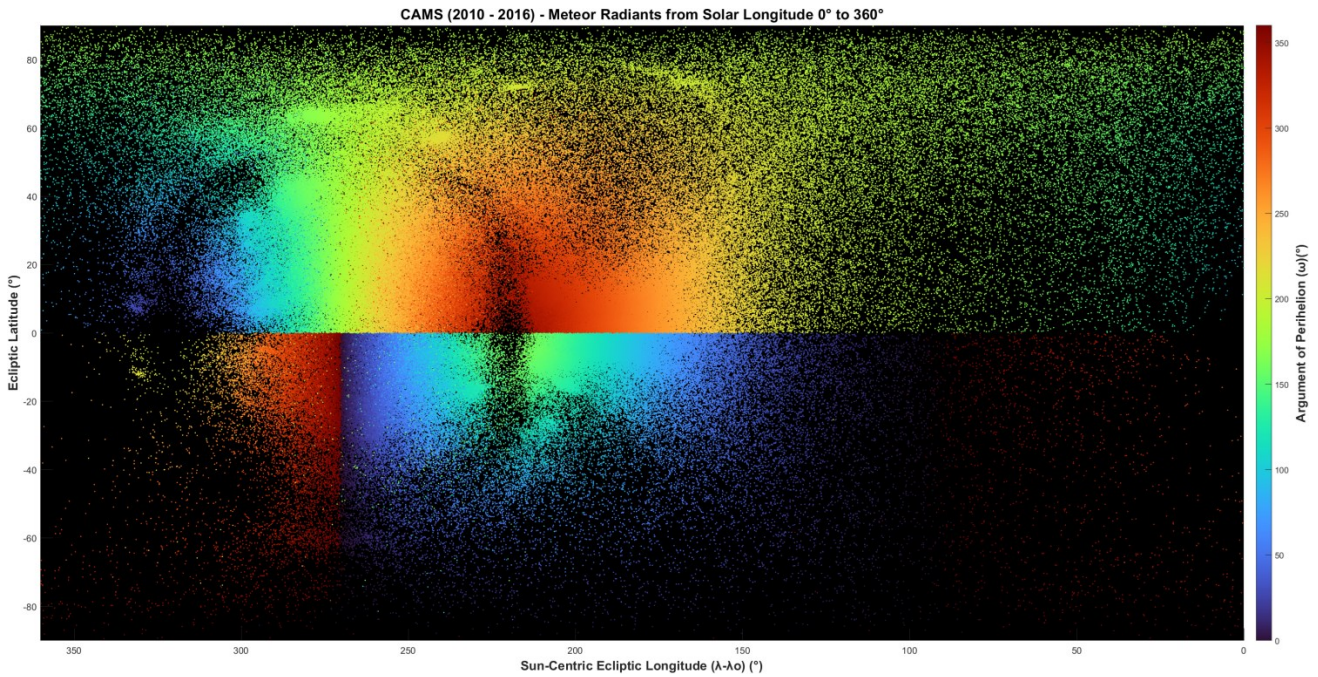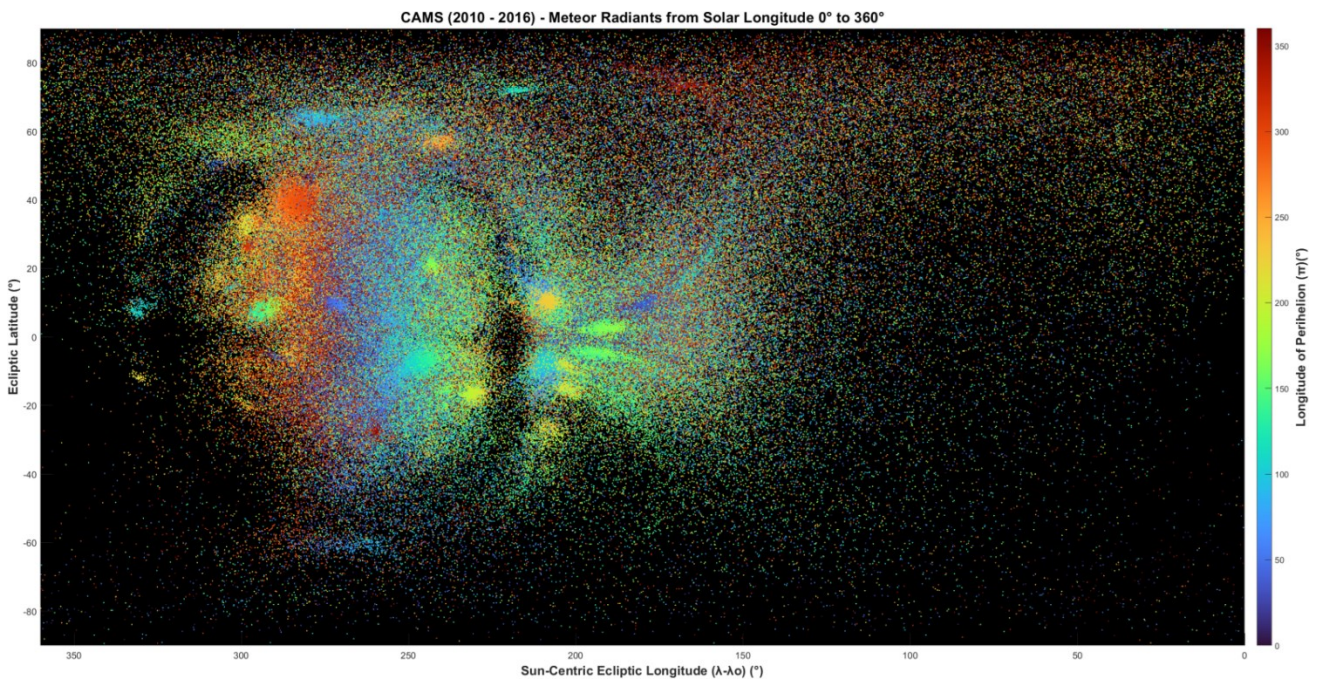
Figure 7 – Argument of perihelion ω.

Figure 8 – Longitude of perihelion Π.

The Apex shows a background distribution of Π that approaches 0° at the center (270° longitude), from high values on the east, and from low values on the west. Shower clusters of various colors stand out against this background variation.

The southern Toroidal source appears to contain two sets of Π values (red on the east and blue on the west). The northern Toroidal source is too obscured by the background to tell if a red component is present, but does have a blue shower cluster on the eastern side, symmetrical about the Apex of the Earth's direction of motion (270°/0°) with the southern blue component. Both components cross over the 270° longitude line in the south, where the value of ω changes abruptly. The northern blue shower cluster is completely on the eastern side of the 270° longitude line.

4   Non-Keplerian element distributions

D criteria D_N and D_R are expressed in terms of the Öpik parameters U, ϕ, and $cos\ \theta$ (Valsecchi, et al., 1999). Here, we examine how well those parameters separate showers and their sporadic background.

Vector *U*:
U is the vector of the meteoroid (Öpik, 1976). The dimensionless magnitude of U is the meteoroid velocity divided by the Earth's velocity, with a maximum ratio of 2.53. When U is scaled from 0 to 2.53 the plot is identical to the plot for v_g scaled from 0 to 75 kilometers per second shown in *Figure 1*. The direction of U is defined by ϕ and θ, discussed below.
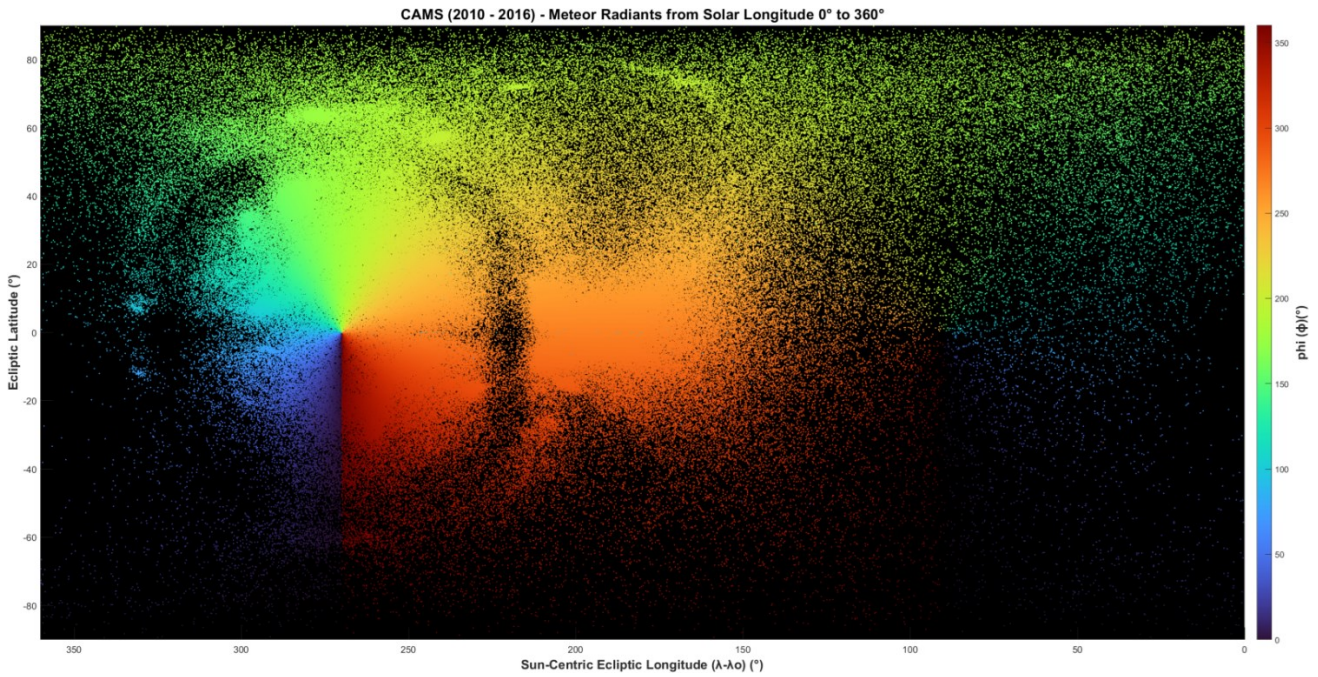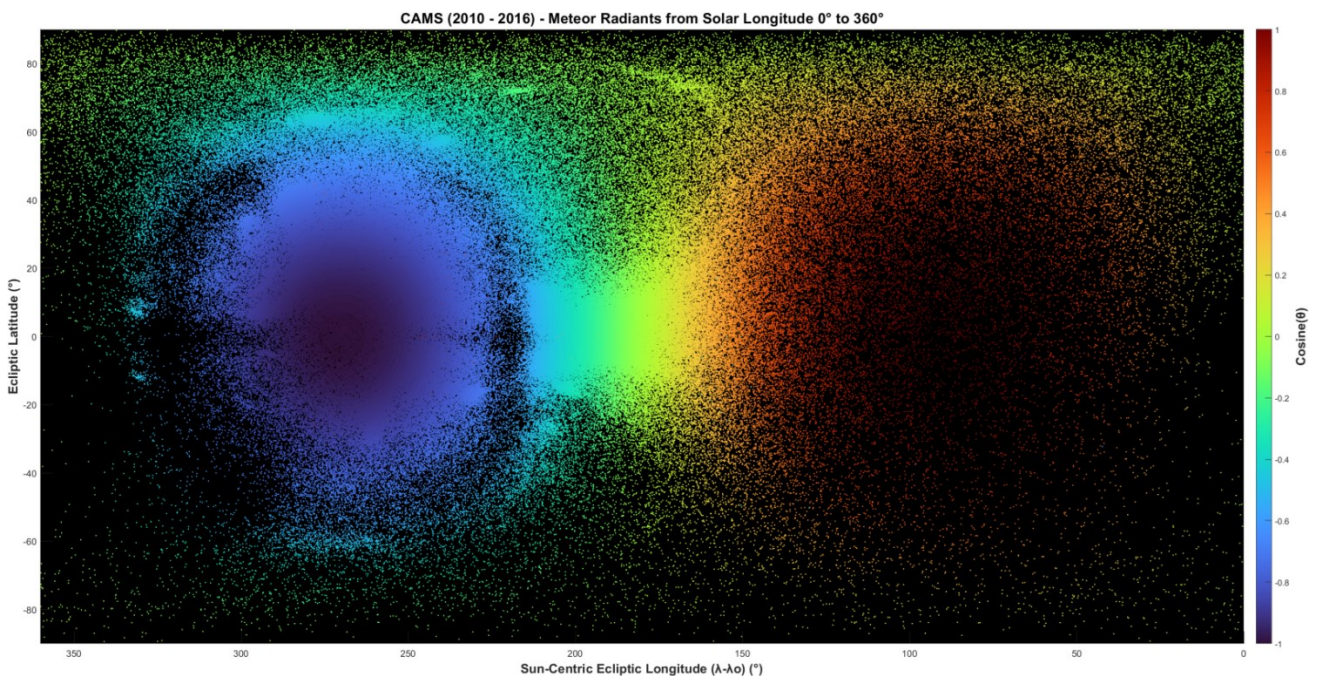
Figure 9 – Öpik variable ϕ.

Figure 10 – Öpik variable cosine (θ).

Angle phi, ϕ:

Figure 9 shows phi ϕ, the angle between the plane containing the vector U and the y–z plane, where the positive y-axis is the direction of the Earth's way, and the z-axis is normal to the ecliptic plane. The y-axis intersects the plot at the Apex (270°/0°) and the Antapex (90°/0°).

Figure 9 shows that the color zones revolve around the y-axis as the plane of vector U is rotated around the y-axis and that as an angular value ϕ changes smoothly. The difference between shower radiants and background radiants is undetectable.

Ratio cosine θ:

Theta θ is the angle between the vector U and the direction of the Earth's way, the positive y-axis. In *Figure 10* cosine θ is used instead of θ because cosine θ is said to be proportional to $-1/a$, which is the orbital energy of the meteoroid.

As an angle ratio, the color zones in the cosine θ plot are smooth, like for ϕ. Again, the difference between shower and background sporadic meteors is undetectable.

Tisserand parameter with respect to Jupiter, T_J:

Figure 11 shows the distribution of T_J. In this plot radiants with $T_J \geq 6.0$ are plotted with larger markers. Radiants with $T_J \geq 7.0$ are plotted with even larger markers.
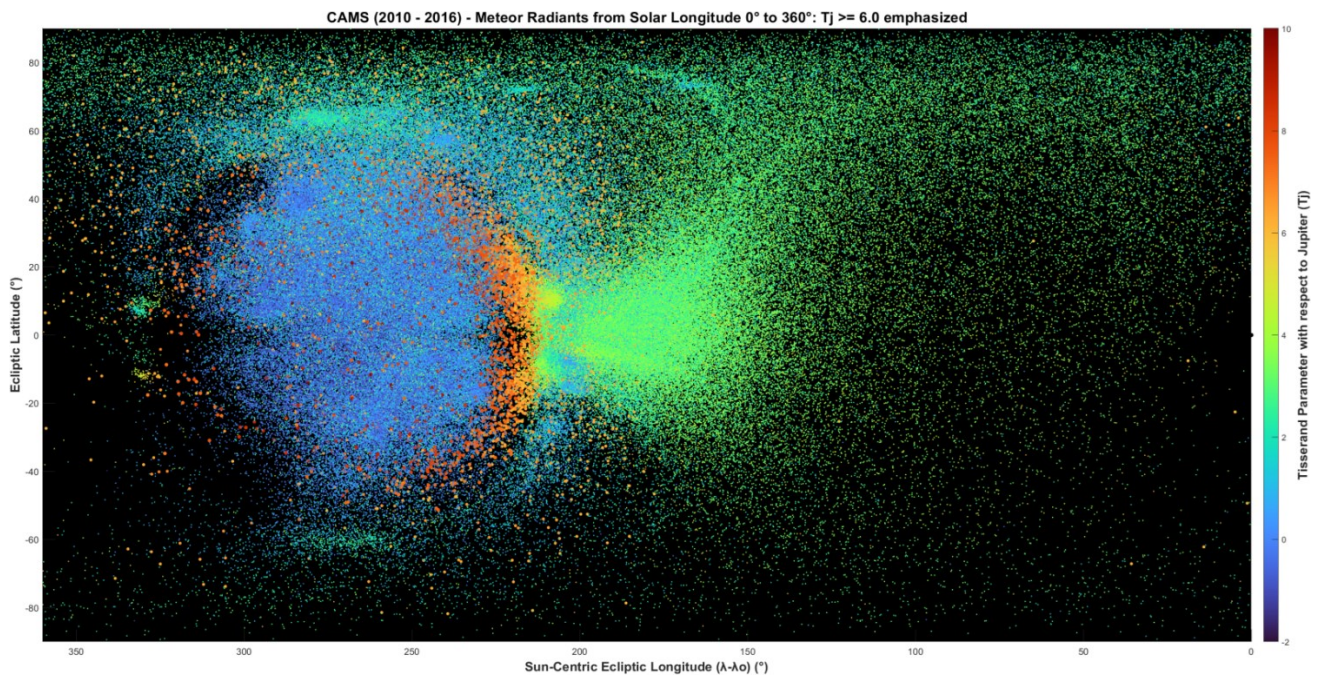
Figure 11 – Tisserand parameter with respect to Jupiter, T_J. Radiants with $T_J \geq 6.0$ are plotted with larger markers. Radiants with $T_J \geq 7.0$ are plotted with even larger markers.

The T_J distribution is mainly divided into two regions, one of blue radiants with low T_J parameters at the Apex and Toroidal ring, and one of green radiants with middle T_J parameters at the Anthelion, Antapex, and poles. A concentration of yellow, orange, and red high T_J parameters appears in the western transition region, and presumably exist in the same way at the eastern transition region, but for lack of data due to daylight.

The Apex is dominated by low T_J parameters near zero, indicating Long Period Comet-type orbits, with occasional orbits having T_J around 1.5–2.0, in between Mellish-type and Jupiter Family Comet (JFC)-type orbits. The Toroidal ring is composed of radiants with Mellish-type orbits with $T_J \sim 1.0$–1.5 while the Toroidal sources have higher T_J parameters of 2.0–2.5 indicating JFC-type orbits.

It was found that radiants with $T_J \geq 7.5$ are confined to the Apex, inside the transition region, but only a small fraction are in retrograde orbits. The larger the T_J threshold, the more restricted the radiants are to the center of the Apex at 270° longitude, 0° latitude. Radiants with $T_J \geq 7.0$ spread wider to the just outside of the transition region. Radiants with $T_J \geq 6.0$ spread even wider to the Anthelion, Helion, and the poles, but not in the Antapex.

Some of the OZR with high T_J parameters seen in *Figures 2 and 11* are in the transition regions where, with low to middle eccentricities, they stand out against the red high e radiants there. They can also be seen in the voids outside the Narrow Apex Source in *Figure 4*.

5   Discussion

The radiant plots show that orbital elements that are mostly determined by the radiant position are distributed across the sky in organized, predictable ways that are the same for shower and sporadic meteors. The perihelion distance, inclination, argument of perihelion, and geocentric velocity are distributed in such a way that the vast majority are surrounded by similar orbital element values, and those values change in gradual and predictable ways moving across the sky.

The gradients of these orbital element values across the sky are not perfectly smooth. In the immediate neighborhood of a radiant, its adjacent neighbors can be slightly larger or smaller in any direction, but as the radiant moves further away from the original location the trends are revealed by the separate and well-defined color zones. These color zones are larger than most shower clusters. The geocentric velocity gradients are the most diverse of the above elements, but still highly constrained in a given radiant direction. It is unclear why the argument of perihelion is relatively smoothly changing towards the Anthelion source direction, compared to other sources and elements.

The distribution of eccentricity and semi-major axis are much less organized because they are mostly determined by the measured speed. The changes from one place to another are far less predictable, yet are still organized in a few ways. The highest eccentricities that approach or exceed 1.0 are concentrated around the east and west transition regions (*Figure 3*), similar to the lowest perihelion distances in *Figure 2*. In the Apex the lowest eccentricities are confined to the center, distributed in the same way as the Narrow Apex source (*Figure 4*), which signifies an excess of low-e orbits in radar observations.

The Öpik parameters U, ϕ, and cosine θ also exhibit a strong organization with strong gradients. U plots identical to v_g and shares the same characteristics. Phi (ϕ) and $\cos \theta$ vary smoothly, expressing an angle and an angle ratio, respectively. Cosine θ is thought to be a near invariant

(Valsecchi, et al, 1999), but a plot of its values does not resemble that of T_J (*Figure 11*). The most noticeable difference is in the Antapex where cosine θ is of the highest values in *Figure 10*, but the highest values of T_J are located in the western transition region, and the Antapex is composed of $T_J \geq 3.0$–3.5 which are still asteroid-like orbits, but not at the extremes of T_J in *Figure 11*.

The transition region:

The "transition region", the void just inside the Toroidal ring, is where various transitions take place. First, it is the boundary that contains all retrograde orbits ($i > 90°$) within the Apex, which also contains a scattering of prograde orbits ($i < 90°$). Outside of this boundary all orbits are prograde. Second, the eastern and western sides at the ecliptic, where the void is at its widest, contain the Sun-grazer orbits, with the exception of the scattered radiants in the Apex that are in asteroid-type orbits with high T_J and small q. The closer a radiant is to the center of this void (~220° longitude, 0° latitude, for the western side) the closer the meteoroid orbits to the Sun. One can think of the Sun as being gravitationally located at these points as q approaches zero. At these same locations, inclinations become chaotic and take on a wide range of values.

These two parts of the transition region are also the epicenters of the highest eccentricities, approaching and exceeding 1.0. Outside of these regions eccentricity is largely mixed, with the lowest eccentricities in the Apex concentrating toward the center (270° longitude).

There are concentrations of high T_J parameters ($T_J > 6.0$) around these regions that tend toward the inside (Apex side) of the transition regions. T_J parameters ≥ 7.5 are completely confined to the Apex inside the transition region boundary.

The argument of perihelion ω approaches 0°/360° in the northern hemisphere, and 180° in the southern hemisphere at these regions. These regions are where perihelion occurs at or near Earth, and is ascending there, or where perihelion occurs on the far side of Earth's orbit and is descending there. In this latter case the semi-major axis must be ≤ 1 AU for the meteoroid orbit to intersect the Earth's orbit but have q on the other side of the nodal line. These radiant orbits are gathered at the Anthelion (and presumably Helion as well) side of the transition region (*Figure 11*).

The Out of Zone Radiants (OZR) seen in the perihelion distance plot, *Figure 2*, are also seen in the argument of perihelion plot. The same OZR can be seen in the eastern and western transition regions of the eccentricity plot, the only areas that are not mixed, and less so in the v_g and T_J plots. These OZR are scattered over the Apex, eastern Anthelion, and western Helion sources while the Antapex lacks them completely. All have high T_J parameters putting them in asteroid-like orbits. The higher the T_J parameter is, the more confined to the Apex of the Earth's way do the radiants occur and that for $T_J \geq 7.5$ the radiants are confined to the Apex source. The OZRs do not show up in the Opik

parameter plots, or in the mixed plots like a, or the Apex distribution of e.

Implications for the use of D criteria:

D criteria are mathematical formulae that describe the similarity between two orbits and are intended to separate shower meteoroids from the sporadic meteoroid background. Most are based on orbital elements q, e, i, ω, and Ω.

It can be seen from the plots that q, i, and ω have distributions that change gradually and more or less smoothly over large areas, forming color zones that are larger than the typical shower radiant cluster, and that shower radiant clusters do not differentiate from these color zones. However, separated over a narrow time span typical of shower durations (a few degrees up to tens of degrees) shows that these elements do stand out from the sporadic background, especially $\Pi = \omega + \Omega$, because it doesn't have the 180° flip of ω and Ω separately when crossing from northern to southern hemisphere.

The plots of a and e (*Figure 5 and 3*) shows a mix of values over most of the sky, but a concentration approaching (and exceeding due to measurement error) $e = 1.0$ is seen at the eastern and western transition regions.

The similarity of orbital elements in different directions at the sky on a given date demonstrates that using sufficiently small thresholds is essential for orbit shape D criteria to be able to differentiate shower radiants from background radiants. Even then, the likelihood of some sporadic pollution is relatively high. The same is true for D criteria that use the near-invariant Öpik parameters, namely D_N and D_R (Valsecchi, et al, 1999). The velocity parameter U is identical in distribution to v_g, and the changes in plots for ϕ and cosine θ being angular and angular ratios, respectively, are smoother than the changes in q, i, and ω, with absolutely no differentiation between shower and background.

6 Conclusion

Meteor orbital elements (q, i, ω) that are mostly determined by the radiant direction are distributed in Sun-centered ecliptic coordinates in a manner that is independent of the time of year. Orbital elements determined by the entry speed (a, e) show a less organized pattern across the sky. Time (solar longitude) correlates strongly with the node Ω.

Several orbital elements and non-Keplerian parameters have all-sky distributions that do not differentiate between shower radiants and background sporadic radiants. Small thresholds are needed for D criteria to identify orbits that are similar.

When viewed over the whole year, meteor showers stand out best in maps of $\Pi = \omega + \Omega$, because adding the element of time to the argument of perihelion parameter separates showers that occur at different times in the year.

References

Jenniskens P., Baggaley J., Crumpton I., Aldous P., Pokorny P., Janches D., Gural P. S., Samuels D., Albers J., Howell A., Johannink C., Breukers M., Odeh M., Moskovitz N., Collison J. and Ganju S. (2018). "A survey of southern hemisphere meteor showers". *Planetary Space Science*, **154**, 21–29.

Jenniskens P. (2023). Atlas of Earth's Meteor Showers. Elsevier, Amsterdam, p. 130.

Koukal J. (2016). "Results of the EDMOND and SonotaCo united databases". *eMetN Meteor Journal*, **1**, 20–23.

Koukal J., Srba J., and Lenža L. (2024). "EDMOND v5.05". *eMetN Meteor Journal*, **9**, 15–23.

Molau S., Rendtel J. (2009). "A Comprehensive List of Meteor Showers Obtained from 10 Years of Observations with the IMO Video Meteor Network". *WGN, the Journal of the IMO*, **37**, 98–121 and back cover of WGN 37:5.

Opik E. J. (1976). Interplanetary Encounters. Elsevier, Amsterdam.

SonotaCo (2009). "A meteor shower catalog based on video observations in 2007-2008". *WGN, the Journal of the IMO*, **37**, 55–62.

Valsecchi G. B., Jopek T. J., and Froeschle C. (1999). "Meteoroid stream identification: a new approach- I. Theory". *Monthly Notices of the Royal Astronomical Society*, **304**, 743–750.

Meteor shower data from video observation Part II
Meteor showers that need careful attention

Masahiro Koseki

The Nippon Meteor Society, 4-3-5 Annaka Annaka-shi, Gunma-ken, 379-0116 Japan
`geh04301@nifty.ne.jp`

The problem with the IAU MDCSD[3] meteor shower table is that users may assume that the meteor showers listed in the table exist exactly as they appear in the list. 0027KSE is rated as an "established shower" but KSE03, which was used as a standard in the previous paper, has been deleted. However, 0839PSR00, located next to KSE03, is in "working status" but is active too. The relationship between KSE and PSR will be explained in detail below. Although there are many similar cases, we will limit the scope related to this paper and explain those in which "Part I, Research methods and summary of survey results" alone may lead to misunderstandings. When a simple explanation is sufficient, it has been supplemented in "Part III, Radiant point distribution map and activity profile." The following 14 cases will be discussed in this Part II.

1. 0027KSE and 0839PSR.
2. 0040ZCY and 0348ARC.
3. 0061TAH: How to name a meteor shower related to Jupiter family comet?
4. 0372PPS and neighbor activities
5. 0165SZC and 0370MIC
6. 0012KCG and neighbor activities: 0012KCG, AXD, 0073ZDR and 0197AUD
7. 0033NIA and 0215NPI
8. The tail of Orionids
9. 0081SLY00 and 0081SLY01
10. 0480TCA and 0481OML
11. The subdivisions of 0002STA and 0017NTA
12. 0338OER and 0490DGE
13. 0340TPY00 and 0340TPY01
14. 0096NCC and 0097SCC

1   0027KSE and 0839PSR

The first observations of KSE were just four photographic meteors captured by Super Schmidt cameras (McCrosky and Posen, 1959). However, no corresponding meteor shower has been found in current video observations. The position of the PSR matches the position of the photographed meteors, but its activity period is about 10 degrees later in solar longitude. *Figure 1* shows meteor activity in the range of λ_{Θ} = 10~30° centered on PSR (λ–λ_{Θ}, β) = (211.69°, 34.29°). *Figure 1 (left)* shows GMN observations, and *Figure 1 (right)* shows IAU MDCSD's KSE with boxes (target), other meteor showers with crosses, and photographed meteors with circles (among them, those marked as KSE are circled in red). The radiant points of IAU MDCSD that appear in *Figure 1 (right)* are shown in *Table 1*.

Although PSR seems to be able to be identified with KSE, the activity profile of PSR is narrow (see 0839PSR in Part III), and therefore the activity at the average KSE of photographic observation λ_{Θ} = 14.7° is inconceivable. IAU MDSD currently has three KSE registrations, but both KSE00 and KSE01 are based on these four photographic meteors. KSE02 is observed by CAMS at the upper left of the 3-degree circle, and it can be assumed that this is a combination of PSR and the activity at the upper left of the 6-degree circle in *Figure 1 (left)*. This 6-degree circle activity corresponds to KSE03 observed by CAMS (deleted in the current IAU MDCSD). For reference, *Figure 2* shows the activity profile estimated by performing the same processing as for other meteor showers based on KSE03. Many radiant points can be obtained in this region through both video and photographic observations (*Figure 1 (right)*). What was identified as a KSE by photographic observations may be a chance association of sporadic meteors, or it may have been active half a century ago and is no longer visible.

SonotaCo Net[4] and GMN[5] both have PSR. Interestingly, GMN uses KSE03, which has now been deleted from the IAU MDCSD, as the KSE entry.

---

[3] https://www.ta3.sk/IAUC22DB/MDC2022/
[4] https://sonotaco.jp/doc/PDA/J14/
[5] https://globalmeteornetwork.org/projects/2023_gmn_shower_table

Table 1 – The radiant points of IAUMDCSD and four photographic KSE meteors (circles in red in *Figure 1 (right)*). Code for photographic meteors, see Koseki (2009).

Code	λ_Θ	$\lambda - \lambda_\Theta$	β	v_g	Distance	Angle	x	y
0027KSE00	14.7	207.7	35.1	45	3.36	285	3.26	0.84
0517ALO00	15.5	226.9	22.1	55.7	18.06	128	-14.18	-11.19
0027KSE01	15.7	209.9	33.3	45.01	1.84	236	1.53	-1.03
0841DHE00	19.5	232.1	46.3	49.5	19.53	46	-14.07	13.54
0027KSE02	20	213.7	36.6	46.7	2.79	35	-1.6	2.29
0836ABH00	20.3	223.1	44.6	47.5	13.5	37	-8.12	10.79
0839PSR00	25.1	211.7	34.3	46.3	0	0	0	0
H1-10366	11.7	212.2	37.5	42	3.21	7	-0.41	3.18
H1-10389	12.7	212	35.6	44.4	1.29	10	-0.22	1.28
H1-10099	16.7	206.5	33.1	46.5	4.49	256	4.36	-1.1
H1-7092	17.7	201.2	31.9	46.7	9.14	258	8.93	-1.97
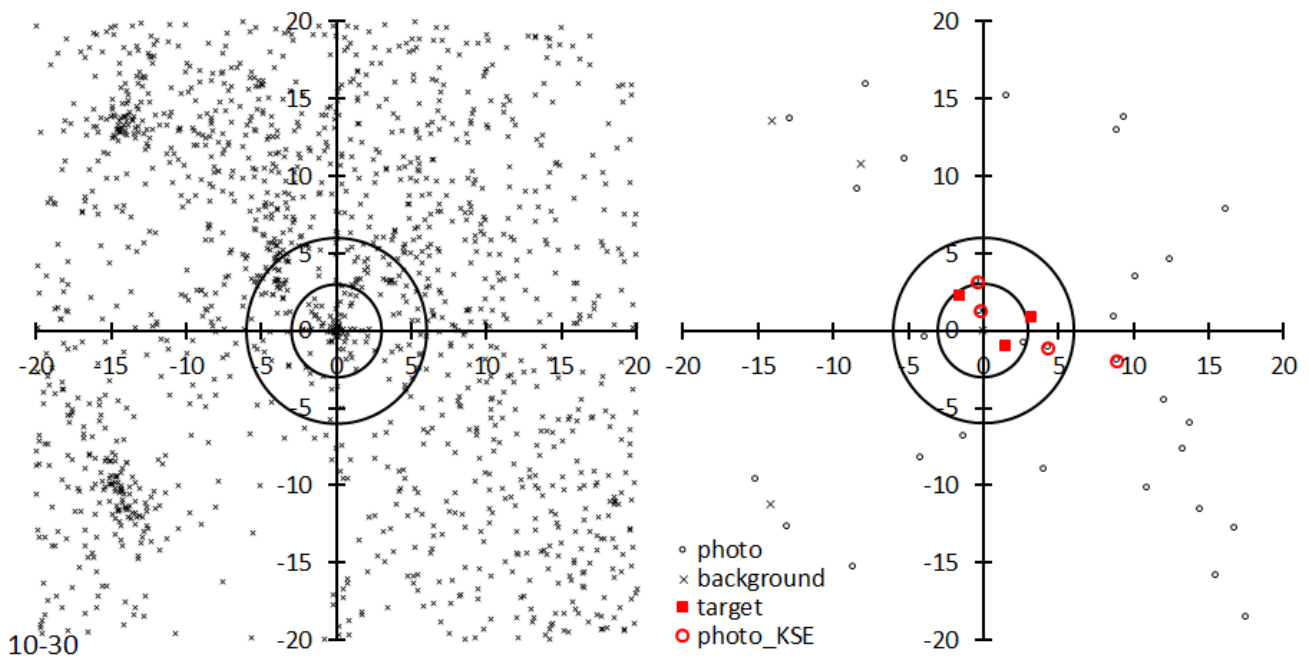
Figure 1 – Radiant point distribution around KSE. GMN (left), IAU MDCSD and photographic meteors (right).
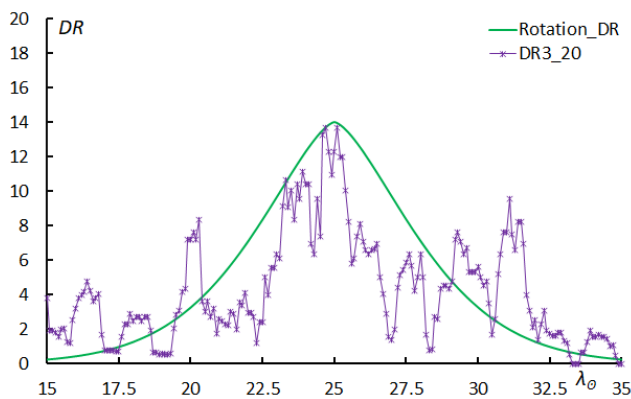
Figure 2 – Activity profile estimate based on KSE03.

2 0040ZCY and 0348ARC

ZCY (zeta-Cygnids) was originally numbered #40 for two similar meteors out of 413 photographed meteors measured by Jacchia and Whipple in their "precision orbit" (Jacchia and Whipple, 1961). Jenniskens combined this with radar observations of Sekanina (1976), which was more than 10 degrees away (Jenniskens, 2006). Currently, an activity different from the photographic observation #40 is called 0040ZCY.

Figure 3 (left) shows the radiant point distribution by GMN for the period $\lambda_\Theta = 0°$ to $50°$, centered on $(\lambda - \lambda_\Theta, \beta) = (307°, 59°)$. 0040ZCY, 0348ARC (April rho-Cygnids), and 0409NCY (nu-Cygnids) all exist in a messy radiant point distribution. If we divide the radiant point distribution into 5-degree increments based on the solar longitude, the ARC can be relatively clearly distinguished from surrounding activities. On the other hand, the activity of ZCY appears to be divided into two groups, one around $\lambda_\Theta = 15°$ (ZCY01) and one around $\lambda_\Theta = 30°$ (ZCY02), based on the activity profile.
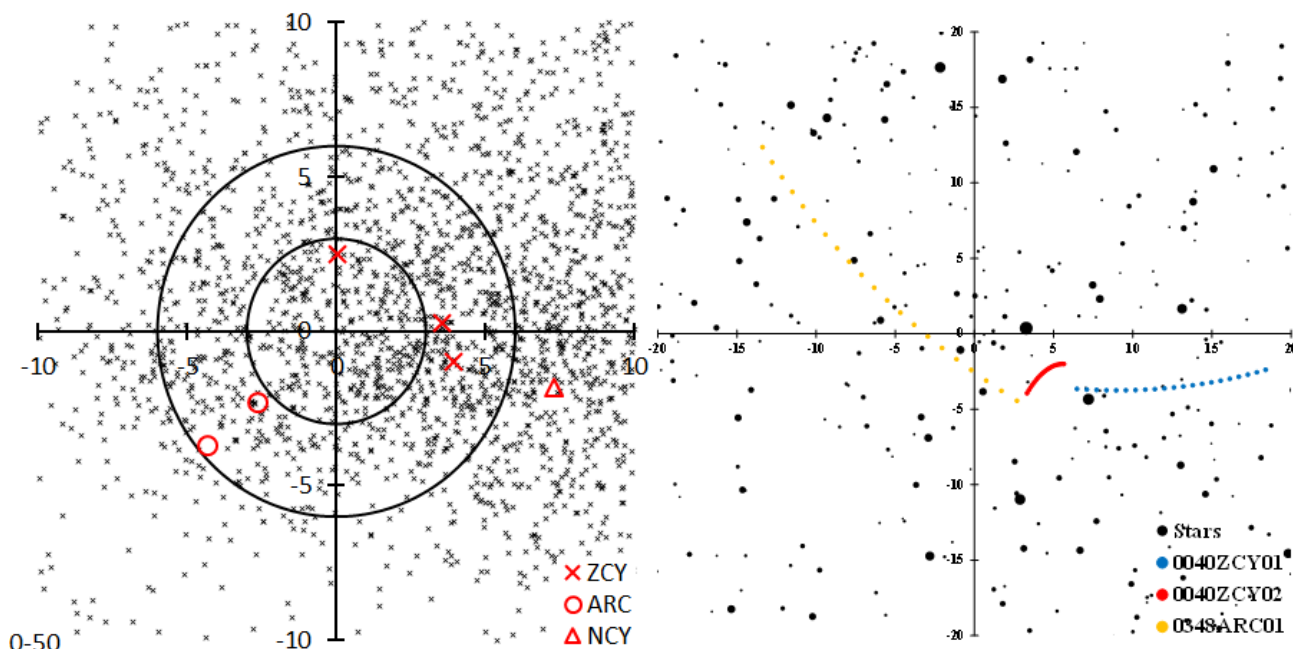
Figure 3 – Radiant point distribution around ZCY and ARC. GMN (left), radiant point movement path estimated in this paper (right).

For this reason, this paper divides the activities into three: ZCY01 (λ_Θ = 5°~25°), ZCY02 (λ_Θ = 20°~40°), and ARC00 (λ_Θ = 30°~50°). *Figure 3 (right)* represents the movement of the radiant point during each period. ZCY01 and ARC00 are moving from right to left (west to east) on the diagram, but ZCY02 is moving strangely, almost stationary, and moving from bottom to top (slightly left to right). However, it is ZCY02 whose activity profile shows a clear increase and decrease.

Considering the radiant shift, the activities of ARC and ZCY02 are close in the range of λ_Θ = 30° to 35°, and the possibility that ZCY01 is connected to ARC via ZCY02 cannot be denied. The strange movement of the radiant point of ZCY02 may be due to interference between ZCY01 and ARC. The activity profiles of ZCY01 and ARC are influenced by the activity of ZCY02.

As seen in *Figure 3 (left)*, the surrounding sporadic meteors are highly active, and further observations are required to draw firm conclusions. 0409NCY might be part of the sporadic meteor activity or ZCY.

Neither ZCY nor ARC appears in the J14 list of SonotaCo net. GMN lists two, but ZCY is grouped as one.

3   0061TAH: How to name a meteor shower related to a Jupiter family comet

In 2022, meteoroid particles ejected from 73P/Schwassmann-Wachmann 3 encountered Earth, resulting in an active meteor shower (Koseki, 2022). However, it is not appropriate to call these TAH (tau-Herculids).

One is that TAH is a meteor shower that was detected and named by Southworth and Hawkins (1963) from photographic observation using D_{SH} and has a very large spread of radiant points. *Figure 4 (left)* shows the distribution of radiant points obtained by photographic observations with IAU MDCSD radiants during the period from λ_Θ = 57.6° to 87.6°, centered at ($\lambda-\lambda_\Theta$, β) = (135.51°, 54.79°) of TAH00. Tau Herculids was named after the two photographic meteors marked with diamonds in *Figure 4 (left)*. Later, Lindblad (1971) thought that the meteor shower consisting of 14 photographed meteors marked with plusses was the same, and this also came to be called tau Herculids (TAH00). However, the meteors photographed with diamonds were observed at λ_Θ = 89.40° and λ_Θ = 93.80°, respectively, and appeared much later than TAH00. This identification itself is problematic, but the photographic meteors spread over a radius of nearly 20 degrees. *Figure 4 (right)* shows meteors observed by GMN during the same period, and the activity area observed in 2022 is visible in the lower right. On the other hand, there is no noticeable concentration of video meteor radiants around TAH00. This is a good example of how it makes a big difference whether a meteor stream is defined by orbit (D_{SH}, Southworth and Hawkins, 1963) or by radiant distribution and geocentric velocity.

Second, the orbits of comets and meteor showers that approach Jupiter often change greatly, and the position of the radiant point also changes significantly. *Table 2* shows the positional relationship of the radiant points with τ Herculis, which is the origin of the name, as the center. H2-7920 and H2-12711 are the meteors that gave rise to the name tau Herculids, and TAH00 and TAH02 are meteor showers registered in the IAU MDC. GMN is the result of observation by GMN in 2022 (Koseki, 2022), and 2022–2049 is the predicted value mentioned in Jenniskens's book (Jenniskens, 2006). The general principle that radiant points are named after the names of nearby stars breaks down significantly. It is not uncommon for the radiant to move so far from its original location that it no longer lives

up to its name when its orbit approaches Jupiter. Currently, the IAU MDCSD does not use the name of the parent object, but this needs to be reconsidered.

Finally, it should be emphasized that this data is from 2022 and does not appear every year. This means that the position of the radiant point and the activity curve will be different the next time when it appears.

Table 2 – The positional relationship of the radiant points with τ Herculis.

Source	α	δ	Distance	Angle
22 tau Her	244.9	46.3		
H2-7920	258.9	50.3	10.1	61.4
H2-12711	238.2	46.3	4.7	271.7
0061TAH00	228.5	39.9	13.6	247.8
0061TAH02	230.4	44.8	10.3	266.8
GMN	208.9	28	33.6	249.8
2022	210	27.4	33.3	247.7
2027	200.4	10.2	52.2	240.8
2049	200	9.3	53.2	240.5
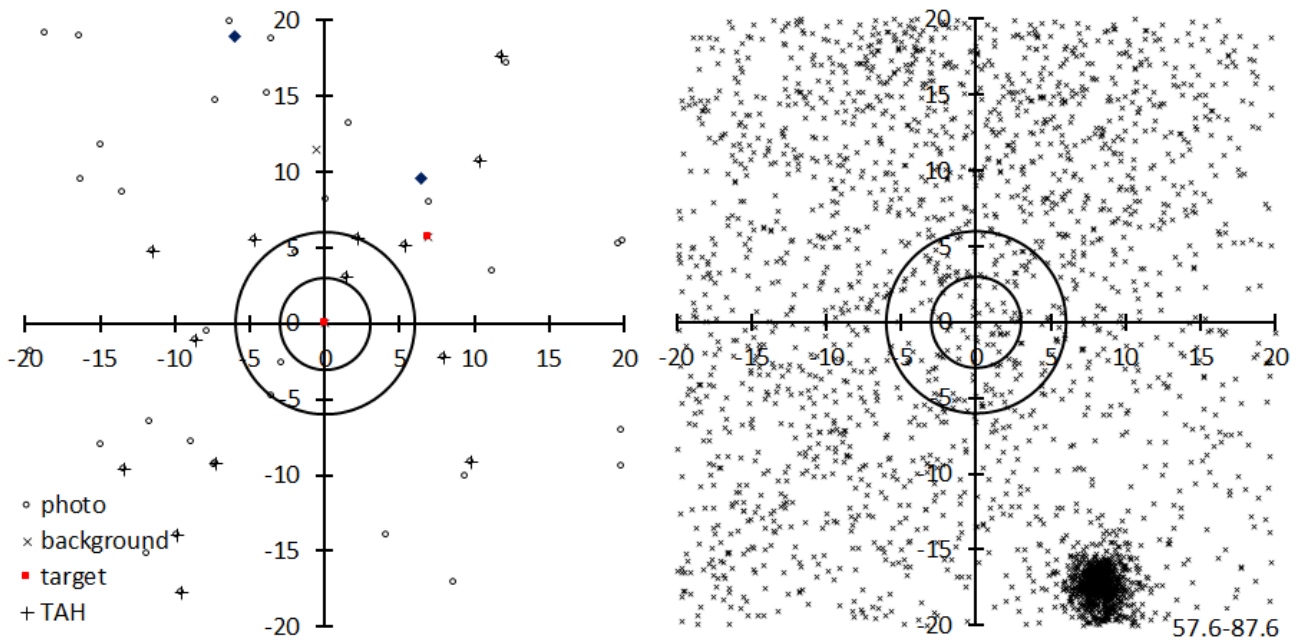
Figure 4 – Radiant point distribution around TAH. IAU MDCSD and photo observation (left), GMN (right).
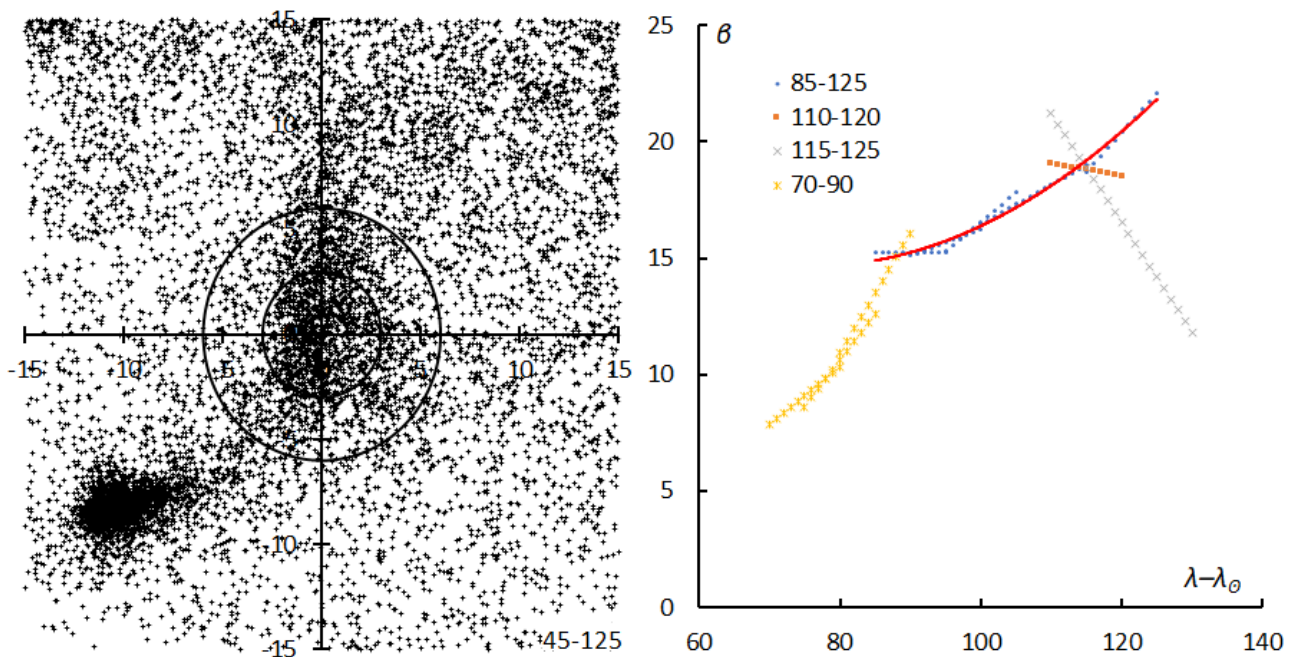
Figure 5 – Water flowing from the water bottle to the fishes: radiant point movement of "PPS" by GMN (left). Estimated ecliptic latitude of the radiant point for every 10 degrees of solar longitude (right).

4   0372PPS and neighbor activities

The radiant point distribution for the period $\lambda_\odot = 45°$ to $125°$ centered at $(\lambda–\lambda_\odot, \beta) = (282.4°, 16.4°)$ is shown in *Figure 5 (left)*. The center is PPS (phi-Piscids) and the bottom left is ETA (eta-Aquariids). It is as if there is activity extending upward from ETA through PPS. There is an existence called "the tail of Orionids" (Jenniskens et al., 2016a) and it can also be compared to water flowing from an aquarium to fishes (as a constellation, water flowing out of Aquarius flows into the mouth of Piscis Austrinus). The question of how much of this flow should be considered as PPS activity is complicated, similar to the question of how to demarcate the activities within the "the tail of Orionids".

If the radiant point at $\lambda_\odot = 85°$ is $(\lambda–\lambda_\odot, \beta) = (285°, 13°)$, find the movement of the radiant point so that the regression line converges as in the case of other meteor showers. This operation was repeated with the next radiant point located 5 degrees before and after the solar longitude.

The results for the ecliptic latitude of the radiant point are shown in *Figure 5 (right)*. The activity with $\lambda_\odot < 85°$ appears to be different from the activity that precedes it. How this activity with $\lambda_\odot < 85°$ is related to ETA remains a future issue. Even when $\lambda_\odot > 85°$, the movement of the radiant point (the line from $\lambda_\odot = 110°$ to $120°$) calculated around $\lambda_\odot = 115°$ is heterogeneous. If we investigate the movement of the radiant point for $\lambda_\odot = 115°\sim125°$ with $(\lambda–\lambda_\odot, \beta) = (279.0°, 16.0°)$ as the center, we can find the movement indicated by plusses in the figure for $\lambda_\odot = 115°\sim125°$ (in the figure, this result is extrapolated 5 degrees forward and backward). The radiant point

distribution spreading from the center to the lower right in *Figure 5 (left)* corresponds to this movement. In this paper, this is called PPS_1, and the period excluding this period, shown by the red curve in *Figure 5 (right)*, is called PPS_0.

5   0165SZC and 0370MIC

In the current IAU MDCSD, what should be classified as 0370MIC (Microscopiids) is placed in 0165SZC (Southern June Aquilids). As shown in *Table 3*, 0165SZC00, 01 is completely different from the reports below. It is clear that 165SZC02 and below are the same activities as 0370MIC00. This is thought to be because the degree of attention differs depending on whether the shower status flag (*s*) is 1 (established shower) or 0 (working list). 0370MIC00 was reported in 2010, and subsequent reports below 0165SZC02 should be included in 0370MIC.
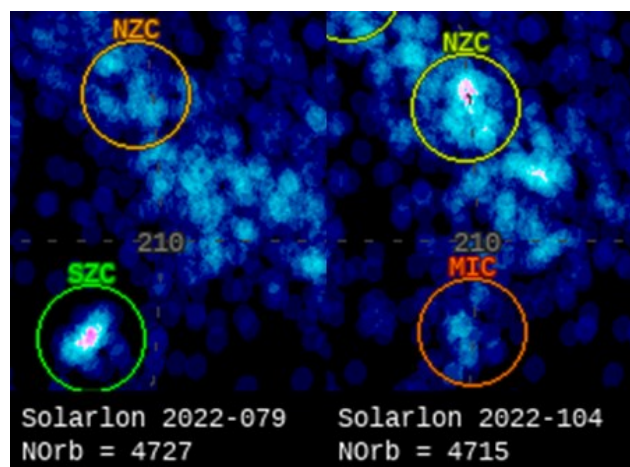

Figure 6 – SZC (left) and MIC (right) in CMOR observation.

Table 3 – Confusion between SZC and MIC in IAUMDCSD.

Code	s	α	δ	v_g	$\lambda_\odot$	$\lambda–\lambda_\odot$	β	References
0165SZC00	1	304.8	-33.92	33.17	79.7	219.5	-13.94	1] Gartrell & Elford, 1975
0165SZC01	1	304.7	-32.8	38.6	80.5	218.89	-12.83	2] Brown et al., 2008
0165SZC02	1	319.3	-27.6	39.2	104	209.24	-11.26	3] Jenniskens et al., 2016
0165SZC04	1	320.4	-26.5	39.9	106.5	208.03	-10.51	5) Shiba, 2022
0370MIC00	0	320.3	-28.3	38	104	209.87	-12.2	1] Brown et al., 2010

Both 0165SZC01 and 0370MIC00 were observed by CMOR, and even now, the CMOR image[6] clearly shows that SZC is a completely different meteor shower from MIC (*Figure 6 (left)*). Note that the activity near the original SZC, $\lambda_\odot = 80°$, was short-lived, and only a few meteors were captured by video observations. Probably SZC has many faint meteors. Conversely, MIC is clearly captured in video observations, but not so clearly in CMOR observations (*Figure 6 (right)*).

In GMN, MIC's activities are referred to as SZC, and does neither appear in SonotaCo net's J14 list.

6   0012KCG and neighbor activities: 0012KCG, AXD, 0073ZDR and 0197AUD

There is considerable confusion about the meteor showers in and around KCG (kappa-Cygnids). First of all, it is important to note that KCG is active on an approximately 7-year cycle, and its activity is rarely seen in normal years. The AXD (August xi Draconids: this is the author's tentative name because nothing corresponding to IAU MDCSD has been observed) is located several degrees west of KCG and shows weak activity every year. In GMN observations, there are more AXD than KCG, except in

---

[6] https://fireballs.ndc.nasa.gov/cmor-radiants/earth.html

2021, when KCG was active. *Figure 7* will be explained in detail later, but of the two radiant point groups seen in both figures, the left one is KCG and the right one is AXD. In the current IAU MDCSD, KCG reports are inconsistent due to confusion with AXD.

The second thing that has caused confusion is that the IAU MDC has been misclassifying ZDR (zeta-Draconids) and

AUD (August Draconids). ZDR and AUD are listed as shown in *Table 4* now. However, the Jenniskens meteor shower table (Jenniskens, 2006), which is the prototype of IAU MDC, covers slightly different material. In this earliest meteor shower table, L1-167 and S3-142 in *Table 5* were listed as ZDR observations, and both S3-147 and S3-149 were listed as AUD.
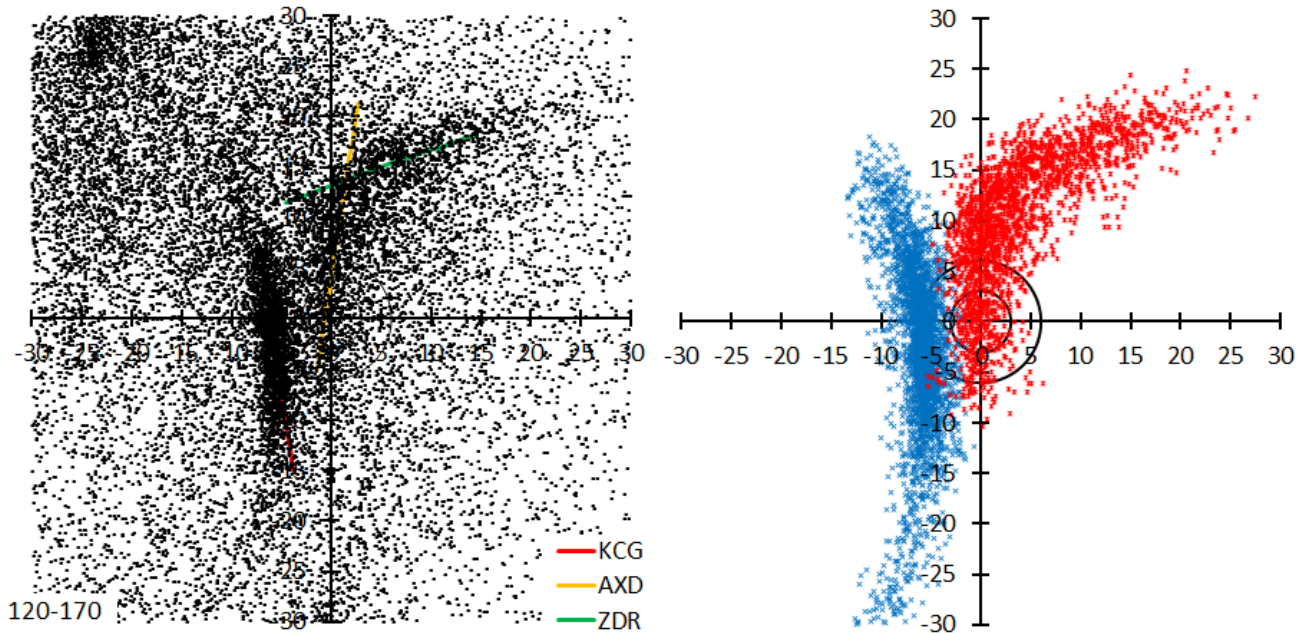
Figure 7 – KCG and AXD. Among the radiant points at left, only the radiant points are picked out which were classified by GMN as KCG (in blue) or AUD (in red) at right.

Table 4 – Meteor showers listed as ZDR or AUD in IAU MDCSD.

Code	s	α	δ	v_g	λ_Θ	$\lambda–\lambda_\Theta$	β	References
0073ZDR00	0	261.7	67.8	22.36	122	33.15	86.55	1] Molau & Rendtel, 2009
0197AUD00	1	272.45	64.91	17.3	141.9	160.51	88.06	1] Sekanina, 1976
0197AUD01	1	271.7	58.9	21.1	143	133.57	82.3	2] Jenniskens et al., 2016
0197AUD03	1			21	149			4) Shiba, 2022

Table 5 – Confusion in ZDR and AUD. For the source, see Koseki (2009).

Source	α	δ	v_g	λ_Θ	$\lambda–\lambda_\Theta$	β	Shower
L1-167	260	30	18	135	120.6	52.9	θ-Herculids
S3-142	303.2	42.7	17	139.7	184.1	60.1	Gamma-Cygnids
T1-110	270.7	54.1	21.9	148.4	123.4	77.5	ζ-Drads
L1-207	269	59	24	149.5	116.6	82.4	ζ-Draconids
S3-147	271.3	65	23.6	140.8	148.7	88.4	August Draconids
S3-149	272.4	64.9	17.3	141.2	160.6	88.1	φ-Draconids
Denning	260.5	63.3					ζ-Draconids

Table 6 – Definition of KCG and AUD by GMN.

Code	$\lambda_{\Theta min}$	$\lambda_{\Theta ref}$	$\lambda_{\Theta max}$	$\lambda–\lambda_\Theta$	$\Delta(\lambda–\lambda_\Theta)$	β	$\Delta\beta$	v_g	Δv_g
KCG_1	93.1	113.6	125	157.943	-0.21	46.628	0.846	18.511	0.039
KCG_2	125	140.1	150	162.943	0.733	70.573	0.634	22.312	0.202
KCG_3	150	154.7	167.1	187.379	3.3	78.47	0.219	25.638	0.264
AUD_1	130.7	142.7	148	144.446	-0.468	79.238	0.881	21.114	0.184
AUD_2	148	153.5	164.9	57.173	-2.675	81.706	-0.885	21.142	-0.199

The scope of ZDR in the earliest table is ambiguous (L1-167 and S3-142 in *Table 5*), and the current IAU MDCSD ZDR is far from them. The existence of the latter cannot be confirmed at all in past photographic observations or modern video observations. However, there are photographic observations (T1-110 and L1-207 in *Table 5*) that can be identified as ζ-Draconids that appear in the classic Denning meteor shower table (Denning, 1899). Had the IAU MDCSD adopted either of these studies, the situation would have been different.

S3-147 and S3-149 in *Table 5*, which are listed as AUD in the earliest tables, are both from Harvard radio observations, and the radiant points are almost the same, with only a slight difference in geocentric velocity. It is unclear why IAU MDSD did not adopt S3-147 (August Draconids), which is the origin of the name AUD. In addition, the radiant points of the current IAU MDC AUD00 (S3-149) and AUD01 listed above are several degrees apart, and there is also a difference in geocentric velocity, so there are some doubts about their identification.

In addition to the confusion of IAU MDC, there is also the problem of the shape of the radiant point distribution, as seen in *Figure 7*. *Figure 7* plots all the radiant points observed by GMN during the period $\lambda_\Theta = 120°$ to $170°$, centered on $(\lambda–\lambda_\Theta, \beta) = (145°, 75°)$. The two radiant point distributions are each curved. *Figure 7 (right)* shows only the meteors classified to be KCG or AUD by GMN. *Table 6* quotes how GMN represents KCG and AUD, and GMN divides KCG into three parts and AUD into two parts. $\lambda_{\Theta min}$ and $\lambda_{\Theta max}$ indicate the lower and upper limits of the respective periods. $\lambda_{\Theta ref}$ is the representative value for each period, and the values of $\lambda–\lambda_\Theta$, β, and v_g correspond to it. $\Delta(\lambda–\lambda_\Theta)$, $\Delta\beta$ and Δv_g indicates the amount of change depending on the solar longitude.
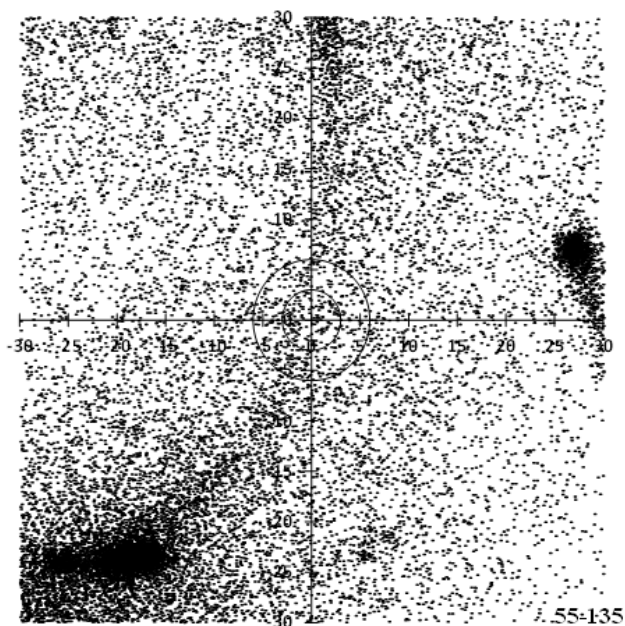
Figure 8 – Radiant arcs extending south of KCG.

As for the curve of this radiant point distribution, interestingly, a series of radiant points can be traced even

before $\lambda_\Theta = 93.1°$, which GMN considers to be the start of KCG activity, as shown in *Figure 8*. *Figure 8* shows the radiant distribution for the period from $\lambda_\Theta = 55°$ to $135°$, centering on $(\lambda–\lambda_\Theta, \beta) = (160°, 35°)$. The radiant points at the top center of the figure represent the early activity of KCG. The radiant density distribution decreases towards the center of the figure, but it appears to extend further down to the ecliptic showers (0456MPS, 0150SOP).

One idea is to set multiple definitions for a single meteor shower like GMN, but on the other hand, it is also possible to break them down into independent activities. In this paper, we will not discuss KCG_1 and KCG_3 proposed by GMN as future issues. In addition, AUD_1 and AUD_2 are divided into two meteor showers, AXD and ZDR, respectively. This classification into AXD and ZDR follows the previous meteor shower table based on SonotaCo net data and the analysis using EDMOND data (Koseki, 2020).

Neither AUD nor ZDR is featured in SonotaCo net's J14 list. It should also be noted that the definition of KCG is different between the J5 list which was applied to the orbit catalogue until 2020 and the J14 list (KCG_ja) in the SonotaCo net shower table, as shown in *Figure 9*.
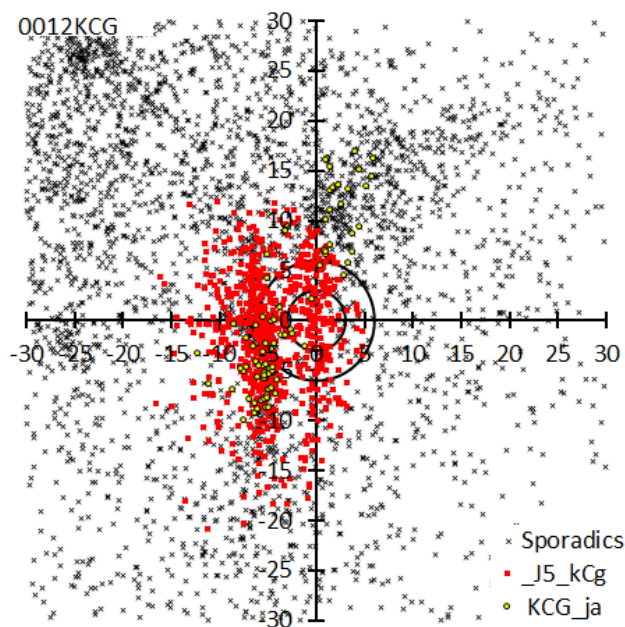
Figure 9 – Changes in the definition of KCG in SonotaCo net.

7   0033NIA and 0215NPI

NIA stands for "Northern iota-Aquariids", while NPI stands for Northern delta-Piscids. Although this paper assumes that NIA and NPI should be unified, the two are often separated, including in the IAU MDCSD. It is necessary to explain the cause of this confusion.

The "Northern ι-Aquariids" came to attract attention due to research by Wright et al. (1957) using Harvard photographic observations. They linked the detected meteor activity to the ι-Aquariids reported by McIntosh (McIntosh, 1935) in New Zealand. It has been thought that the northern branch of the ι-Aquariids (also the southern

branch) is active from late July to early August, almost the same period as the group of the δ-Aquariids. The early radio observations by Ellyett & Roth (1955) cited by Wright et al. (1957) were also from late July to early August. It is true that Wright et al.'s observations also include meteors in the range of $\lambda_O > 145°$, but they should be distinguished from "original ι-Aquariids". *Table 7* shows the entries reported to be part of the ""Northern ι-Aquariids" based on observations in the 20th century, and the top three correspond to "original ι-Aquariids". The bottom three seem to have been named after the "original ι-Aquariids" even though NPI has been observed.

The NIA section of the IAU MDCSD contains a mixture of reports that were influenced by the "original ι-Aquariids"

and reports that actually refer to NPI activities. *Table 8* shows all NIA and NPI reports listed in the IAU MDCSD.

It is thought that NIA00, 01, and 04 were attempts to observe this "original ι-Aquariids". The remaining NIA02, 03, 05, and 07 are reports after NPI00-02, and should be included in NPI.

Both GMN and SonotaCo Net have confusion in their treatment of NIA and NPI, and both treat them as separate groups. However, as shown in *Table 9*, the estimated value from the radiant shift that combines NIA and NPI in this paper (shown as NIA + NPI) sufficiently represents the radiant points of both, and NIA and NPI should be treated as one activity.

Table 7 – Various "Northern ι-Aquariids". For No., see Koseki (2009).

No.	α	δ	v_g	$\lambda-\lambda_O$	β	e	q	i	ω	Ω	λ_O	Stream
LE-313	326.1	-3.4	39	208.8	9.7	0.94	0.1	28.9	328.8	118.3	118.3	Northern i-Aquariids?
K1-91	321.7	-7.8	35	200.8	6.9	0.89	0.2	12	313	120.7	120.7	N i-Aquariids
NI-61.7.11	326.9	-12.1	30	199	1.2	0.85	0.234	6.9	312.5	126	126	N.i-Aquariids?
S2-50	352.5	-0.8	28.2	200.6	2.2	0.823	0.242	3.2	313.5	152.2	152.2	Northern i-Aquariids
S3-159	350.1	0.6	26.1	198.1	4.4	0.777	0.302	5.2	307.4	153.1	153.1	Northern i-Aquariids
LI-78	354.6	1.3	31	193.5	3.3	0.83	0.326	4	299.7	162.1	162.1	Northern i Aquariids

Table 8 – All entries of NIA and NPI in the IAU MDCSD; "ot" means observation technique.

Code	s	α	δ	v_g	λ_O	$\lambda-\lambda_O$	β	Notes	ot	References
0033NIA00	1	327.66	-5.88	31.2	147.7	180.11	6.76	*1		1] Cook, 1973
0033NIA01	-2	328	-4.7	27.6	145.1	183.44	7.75	*1		2] DMS 2001
0033NIA02	1	356	3	28.6	159.5	198.02	4.34	*1	R	3] Brown et al., 2008
0033NIA03	1	355.4	3.4	28.7	159	198.13	4.95	*1	R	4] Brown et al., 2010
0033NIA04	1	334	-8.3	27.19	142	190.89	2.3	*1	T	5] Molau et al., 2012
0033NIA05	1	346.7	-1.2	31.3	148	199.3	4.14	*1	T	6] Jenniskens et al., 2016
0033NIA07	1	2.3	4.9	29.7	166.9	197.16	3.58		T	8) Shiba, 2022
0215NPI00	2	0.84	3.74	27.4	168.3	193.96	3.1	*2	R	1] Sekanina, 1973
0215NPI01	2	9.15	7.04	25.6	173.5	197.67	2.85	*3	R	2] Sekanina, 1976
0215NPI02	2	7.64	7.14	30.4	173.3	196.54	3.53	*4	P	3] Porubcan & Gavajdova, 1994
0215NPI03	-7	9.2	7.7	31.2	174.4	197.08	3.43	*5		4] Jenniskens, 2006
0215NPI04	2	10.2	8.6	28	176	196.75	3.87	*6	T	5] Jenniskens et al., 2010
0298IAQ00	-2							*7		1] Jenniskens, 2006

Notes:

*1: Member of 298/IAQ complex

*2; In Sekanina 1973, the shower name is Piscids (p. 257 & 260), member of 030/PSC

*3: In Sekanina 1976, the shower name is Piscids (Tab. VI, p. 285) , Member of 030/PSC

*4: In Porubcan & Gavajdova 1994, the shower name is delta-Piscids , Member of 030/PSC

*5: No original reference, member of 30/PSC

*6: ? Encke complex, member of 30/PSC

*7: Group members: 33/NUA, 3/SIA; removed, empty record; NUA is a misprint of NIA.

Table 9 – Comparison of SonotaCo Net's J14 list, GMN's list, and this article's estimated value obtained by unifying NIA and NPI.

Code	Source	λ_Θ	$\lambda-\lambda_\Theta$	β	α	δ
NIA	GMN	162.6	197.19	3.893		
	NIA+NPI	163	197.5	3.8	359	3.7
	SonotaCo	151.8634			350.535	-2.48922
	NIA+NPI	152	199.6	3.9	350.8	0.2
NPI	GMN	183.6	191.771	3.655		
	SonotaCo	182.1232			12.66271	9.177
	NIA+NPI	183	193.7	3.8	14	10.1

8   The tail of Orionids

Figure 10 shows the radiant point distribution observed during the period from $\lambda_\Theta = 130°$ to $240°$, with ($\lambda-\lambda_\Theta$, β) = (254°, –17°) as the center and reveals unique meteor activity series: the tail of Orionids (Jenniskens et al. 2016a). On the left is GMN's video observation, and on the right is the distribution of meteor showers registered with the IAU MDCSD.   *Table 10* gives the radiant points of the distribution map in *Figure 10 (right)*.

The underlined showers are referred to as "The Halley Complex" in the IAU MDCSD. Although not shown in this table, 0719LGM00 ($\lambda_\Theta = 232°$, $\lambda-\lambda_\Theta = 234.06°$, $\beta = –5.01°$) is also included in this group.   RER and PSO look like forked tails.

There is no general standard as to what is considered an independent activity. In addition to ORI, this article covers ERI, PSO, and NUE, which are rated 8 or higher on a 10-point scale in our previous research (Koseki, 2023c).

A band of weak radiant points can be seen to the right of "the tail of Orionids". 0194UCE00, 0583TTA00, and 1142SNT00 correspond to this. *Figure 11* represents the radiant point distribution and activity curve based on TTA taking the radiant shift into account. Although the radiant distribution looks like a single meteor shower, the activity profile suggests multiple activities. Even if this band of radiant points has some common origin, it would take some discussion to recognize it as a single meteor shower. It is interesting that there are other bands of radiant points besides the "tail of Orionids". There are several other examples where "tails" or "bands" are similarly observed, so please refer to those as well, see: *Section 4* "0372PPS and neighbor activities", *Section 6* "0012KCG and neighbor activities: 0012KCG, AXD, 0073ZDR and 0197AUD", *Section 12*, "0338OER and 0490DGE".
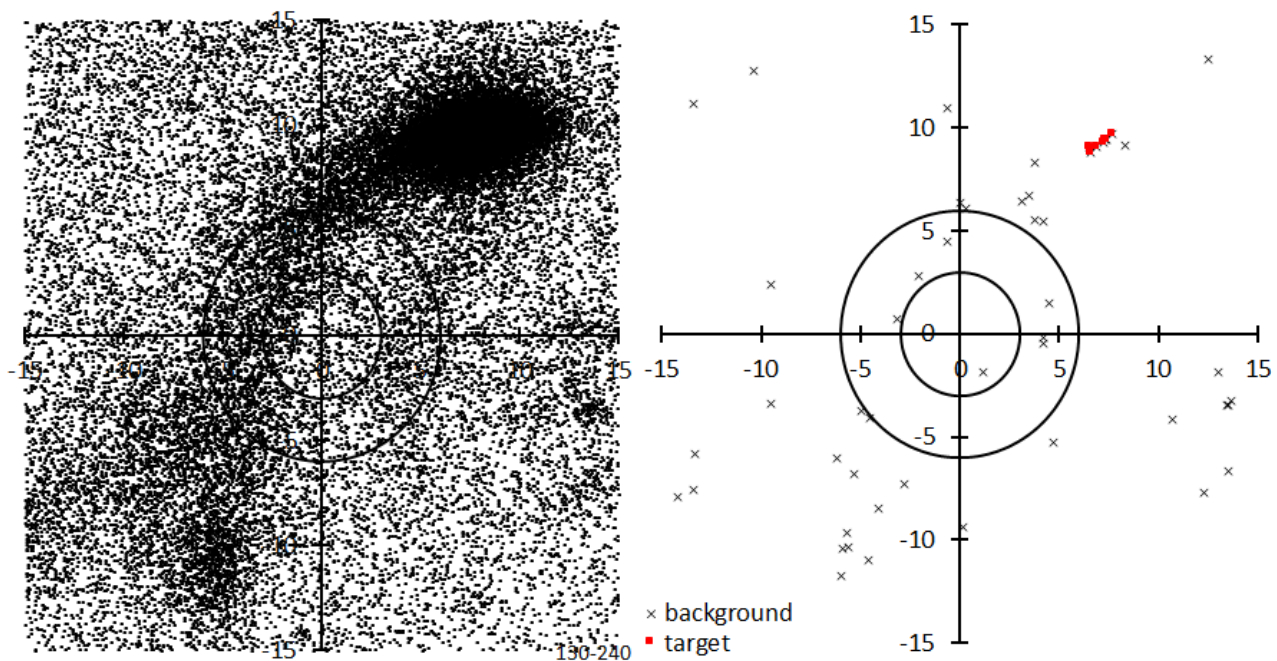
Figure 10 – The tail of the Orionids during the period $\lambda_\Theta = 130°\sim240°$, centered at ($\lambda-\lambda_\Theta$, β) = (254°, –17°). GMN video observations (left), the IAU MDCSD (right).

Table 10 – Radiants around the tail of Orionids in the IAU MDCSD plotted in *Figure 10 (right)*.

Code	λ_Θ	x	y	Code	λ_Θ	x	y	Code	λ_Θ	x	y
0466AOC01	136.8	3.47	6.69	1087OOE00	167.3	4.69	-5.25	0718XGM00	206	3.1	6.4
0191ERI02	137	-5.59	-10.37	0337NUE00	167.9	-4.92	-3.74	1198XRO00	207.1	8.3	9.11
0535THC00	137	12.98	-1.86	0337NUE02	168.6	-4.51	-4.07	0008ORI03	207.5	6.89	9.04
0738RER00	137	-9.48	-3.36	1142SNT00	171.2	4.47	1.47	0008ORI04	207.9	6.52	9.07
0191ERI00	137.5	-5.97	-11.75	0595TTT00	175	12.5	13.33	0008ORI05	208	6.6	8.77
0191ERI01	137.6	-5.87	-10.45	0430POR00	178.4	-2.09	2.8	0008ORI01	208.6	7.33	9.45
0466AOC02	138	4.24	5.46	0896OTA00	179.3	-13.37	11.14	0008ORI00	208.7	7.41	9.43
0466AOC00	138.5	3.74	5.53	0211AOR00	182.8	-9.51	2.38	0008ORI06	209	7.24	9.27
0194UCE00	145.7	4.22	-0.17	0876ROR00	185.3	1.15	-1.87	0008ORI02	209.8	7.68	9.67
0193ZAR00	146.7	-10.39	12.73	0479SOO00	185.6	0.34	6.06	0232BCN00	214	-4.63	-10.97
0873OMI00	152.8	10.71	-4.18	0479SOO01	185.7	-0.62	4.49	0558TSM00	221	-5.7	-9.66
0552PSO01	159	-14.17	-7.94	0225SOR01	187	-6.2	-6.04	0243ZCN00	225	-0.64	10.94
0337NUE03	163	-3.16	0.72	0479SOO02	187	0.04	6.35	0558TSM01	227	-4.06	-8.46
0583TTA00	164	4.19	-0.44	0225SOR00	191.7	0.14	-9.38	0245NHD00	234.8	-5.32	-6.81
0337NUE01	165	-13.36	-5.8	0226ZTA01	196	3.79	8.28	0246AMO00	239	13.48	-3.43
0552PSO00	166.3	-13.42	-7.6	1090EOR00	196.5	12.29	-7.69	0246AMO01	239.3	13.44	-3.47
1088SEE00	166.5	13.51	-6.67	0227OMO00	206	-2.81	-7.33	1196ZCM00	239.8	13.64	-3.28
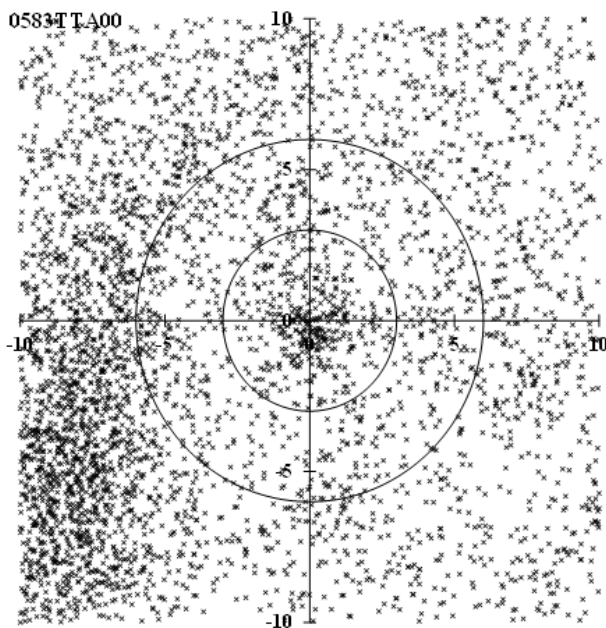
Figure 11 – Third tail of Orionids? The radiant point distribution using 0583TTA00 data taking the radiant drift into account.
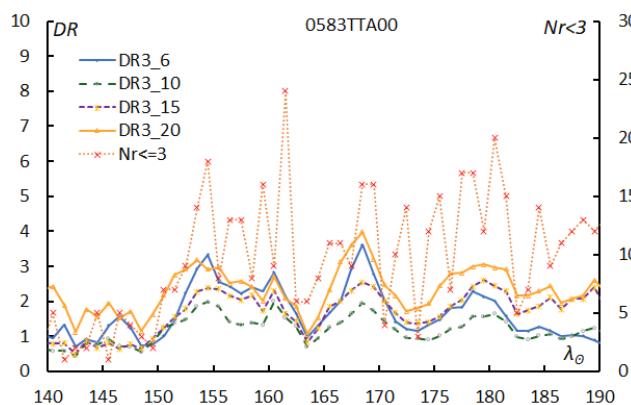
Figure 12 – The activity profile of the "third tail of the Orionids" plotted in *Figure 11*.

9   0081SLY00 and 0081SLY01

The confusion began when 0081SLY was considered a single activity by the same observer (Molau and Rendtel, 2009). In *Figure 13 (left)*, the upper left of the 6-degree circle is SLY00, and symmetrically, the group of spread radiants at the lower right of the circle is SLY01. Not only are they more than 10 degrees apart in position, but there is also a 20-degree difference in solar longitude. For this reason, SLY is on the working status, and as a result, the IAU MDCSD has given each of the two SLYs different numbers and names: 0705UYL00 = SLY00 and 0424SOL00 = SLY01. 0425PSA01 and 0613TLY00 may also be included in the SLY01 activity.

Lindblad's "Lyncids" (Lindblad, 1971), which corresponds to SLY01, is used as 0081SLY in the Jenniskens meteor shower table (Jenniskens, 2006) , which is the prototype of IAUMDC. Molau and Rendtel (2009). probably detected SLY01 as a counterpart to this observation and found SLY00 as another candidate. In *Figure 13 (right)*, triangles are meteor showers that are not listed in the IAU MDCSD, and the filled triangle are the "Lyncids". Among the circles in the photographic observations, two meteors that Lindblad identified as belonging to the "Lyncids" are indicated by filled circles.

SonotaCo net's J14 list takes UYL, but not SLY01. GMN treats SLY01 as SOL. In this paper, SLY00 will be referred to as SLY_0 and SLY01 will be referred to as SLY_1.
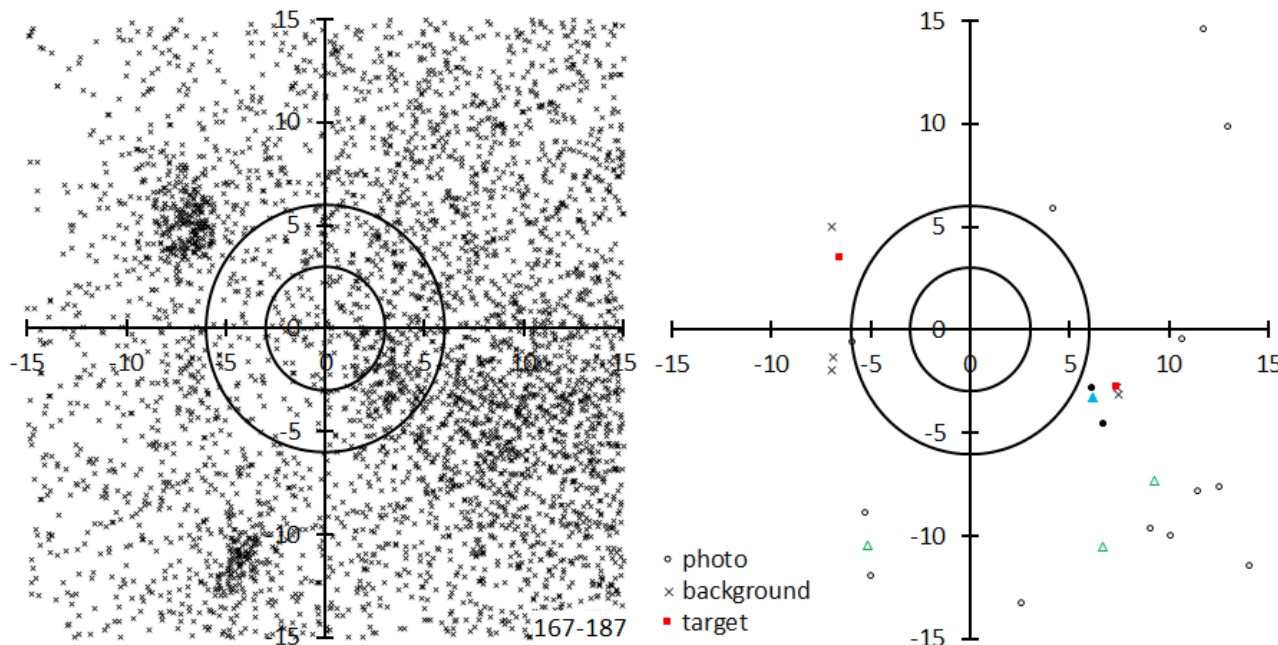
Figure 13 – Two SLYs during the period $\lambda_\Theta = 167°\sim187°$ centered at $(\lambda–\lambda_\Theta, \beta) = (287°, 29°)$. Video observations of GMN (left), Photographic observations and the IAU MDCSD (right).

10 0480TCA and 0481OML

Contrary to SLY, confusion arose because the same observer (Rudawska and Jenniskens, 2014) separated 0480TCA and 0481OML into two separate activities, in this case. Both TCA and OML are meteor showers detected by combining SonotaCo net and CAMS data. *Figure 14* shows the radiant distribution for the period $\lambda_\Theta = 192°\sim232°$ centered on $(\lambda–\lambda_\Theta, \beta) = (283°, 14°)$, and as can be seen, the two activities are continuous. The radiant point on the lower right is due to early Leonid activity.
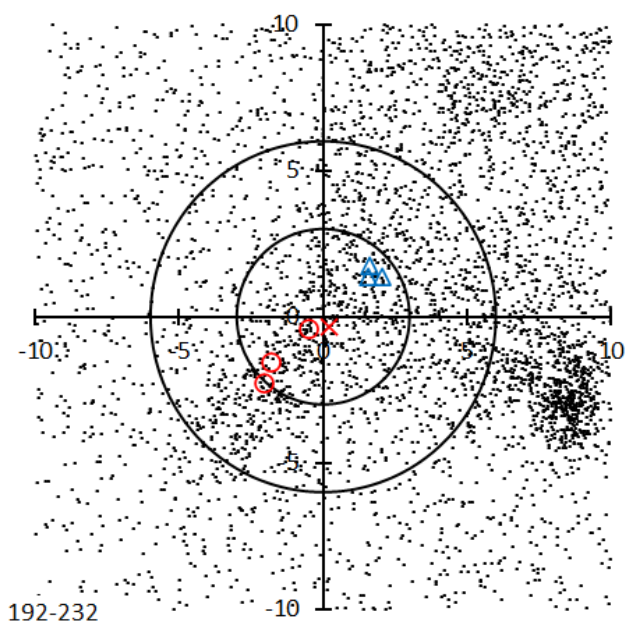
Figure 14 – TCA and OML; small dash: GMN video observations, circle: TCA, triangle: OML, cross: SGC.

Both TCA and OML are on the working status in the IAU MDCSD, and a new meteor shower called 1114SGC

(sigma1-Cancrids) has been added to the IAU MDCSD, which corresponds to TCA.

In GMN, the name OML is not used, and the activities at $\lambda_\Theta = 178.5°\sim221.9°$ are referred to as TCA. SonotaCo net's J14 list features both TCA ($\lambda_\Theta = 200.6°\sim208.1°$) and OML ($\lambda_\Theta = 216.8°\sim221.5°$).

11 The subdivisions of 0002STA and 0017NTA

STA

IAUMDCSD annotates the following seven reports as "#2/STA component": 0286FTA00、0625LTA00、0626LCT00、0627NPS00、0628STS00、0636MTA00、0637FTR00. In addition to this, 0624XAR00 is also considered part of STA. The SonotaCo net J14 list does not treat it as an independent activity and sets a long activity period of $\lambda_\Theta = 181.57°\sim267.40°$. On the other hand, while GMN considers the above eight activities as activities independent of STA, it also treats STA activities during a period of $\lambda_\Theta = 190°$ to 230° (see *Figure 16 (left)*).

As the author has argued many times, it is appropriate to think of STA in two parts (Koseki, 2012, 2020). Just as Whipple divided the activity into October Arietids and Taurids in November (Whipple, 1940), it was also known from visual observations that the main maximum occurs in November after the less active maximum in October. *Figure 15* represents the radiant points in the range of $\lambda–\lambda_\Theta = 180°\sim205°$ and $\beta = -8\sim2$ during the period of $\lambda_\Theta = 185°\sim245°$. As in the previous paper (Koseki, 2021), the group shown by the straight line is called STA_SE, and the group shown by the broken line is called STA_SF. STA_SE corresponds to October Arietids, and STA_SF corresponds to Taurids in November. STA_SF shows
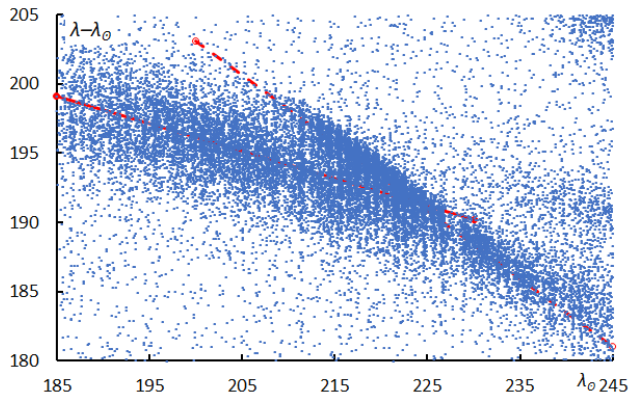
Figure 15 – The distribution of radiants in the range of $\lambda-\lambda_{\odot} = 180° \sim 205°$ and $\beta = -8 \sim -2$, during $\lambda_{\odot} = 185°\sim245°$.

significant activity in the years for which David Asher noted that the Taurids activity intensifies (Asher and Clube, 1993), but STA_SE shows no change. These two activities must be considered separately because they show clear differences in the magnitude ratio and the beginning height of the meteor path (Koseki, 2023a).

NTA

Similar to STA, there are eight reports in NTA with the annotation "#17/NTA component": 0629ATS00, 0630TAR00, 0631DAT00, 0632NET00, 0633PTS00, 0634TAT00, 0635ATU00, 0726DEG00. Even in this case, the SonotaCo net J14 list lumps together the activities with $\lambda_{\odot} = 199.69°\sim276.42°$, but while GMN treats the eight activities independently, it also monitors the activities of NTA during $\lambda_{\odot} = 217°\sim 241°$ (see *Figure 16 (right)*).
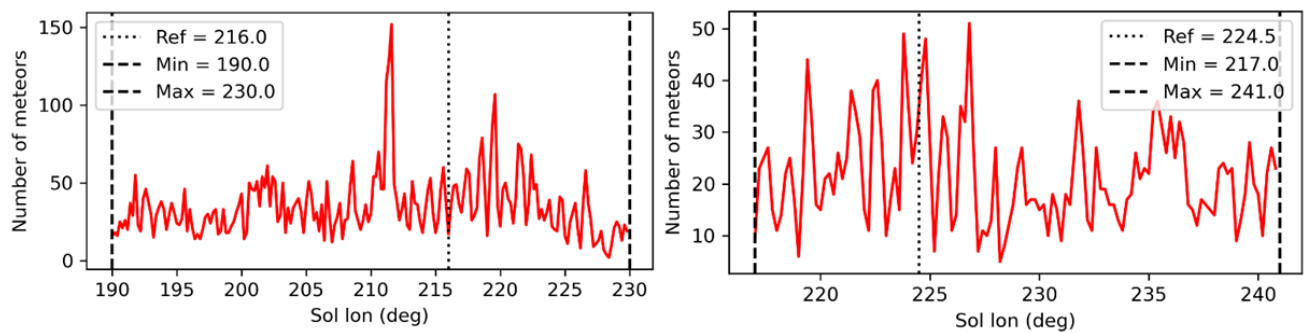
Figure 16 – Observed numbers classified as STA (left) and NTA (right). The true activities of STA and NTA cannot be represented because of the segmenting of their respective activities.
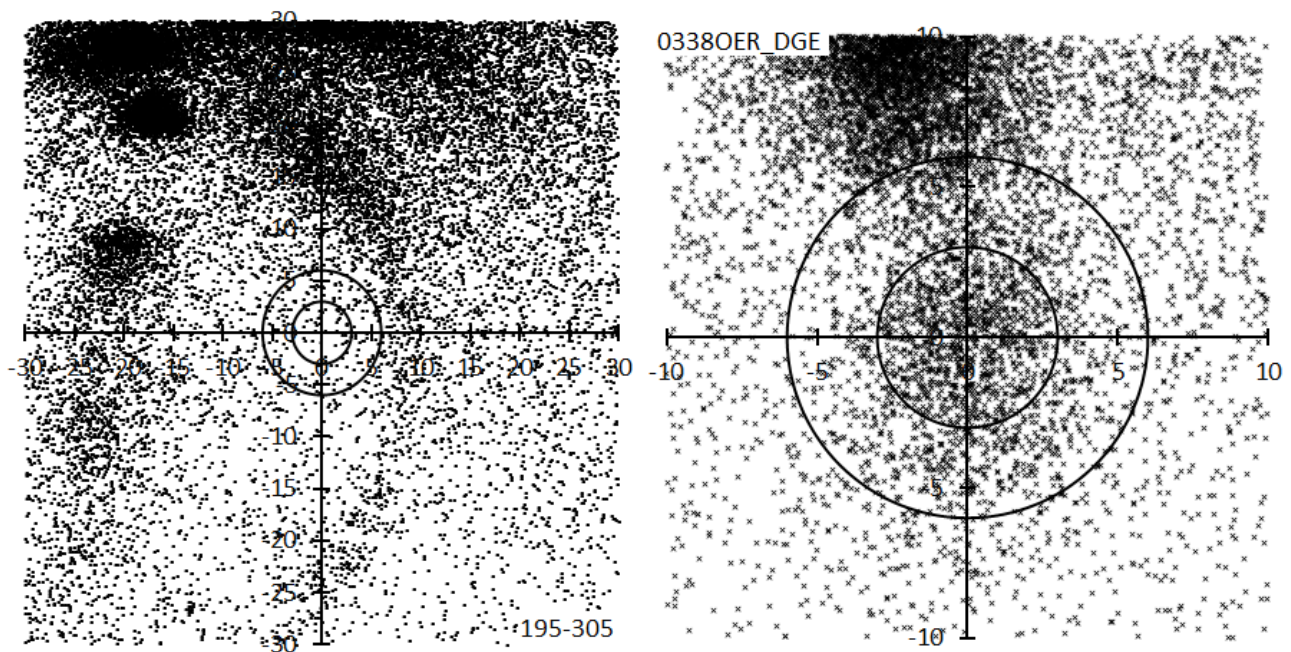
Figure 17 – Radiant arc extending from OER. The radiant distribution for the period from $\lambda_{\odot} = 195°$ to $305°$, centered at $(\lambda-\lambda_{\odot}, \beta) = (185°, -37°)$ (left). Distribution of radiant points with $\lambda_{\odot} = 195°\sim305°$ accumulated along the radiant arc (right).

Table 11 – The IAU MDCSD meteor showers existing within the range of *Figure 17 (left)*.

Code	λ_{Θ}	$\lambda - \lambda_{\Theta}$	β	v_g	Distance	Angle	x	y
0002STA05	196	195.6	-4.2	28.2	5.89	7	-0.69	5.85
0028SOA01	196	196.8	-4.2	29	6.14	18	-1.86	5.85
0002STA03	196.5	195.2	-4.3	27.92	6.07	3	-0.37	6.06
0028SOA00	198.5	195.8	-2.8	25.6	8.94	9	-1.46	8.82
0902DCT00	202.1	194.4	-13.2	32.7	0.96	79	-0.94	0.19
0002STA09	202.4	195.2	-4.6	28.6	9.1	12	-1.86	8.91
0624XAR00	205	195.1	-4.6	28.5	10.18	13	-2.32	9.92
0086OGC00	206.7	199.2	-24.5	3.3	11.5	147	-6.34	-9.6
0338OER03	230.5	184.6	-20.8	28	1.5	190	0.25	-1.48
0338OER01	232	185.7	-20	28.5	1.33	105	-1.28	-0.33
0338OER00	234.7	183.5	-21.8	26.9	1.33	175	-0.11	-1.32
1115NXE00	241.88	180.7	-24.5	26.06	1.42	183	0.08	-1.42
0490DGE00	249.3	176.1	-35.3	23.8	8.67	192	1.79	-8.48
0490DGE01	254	176.8	-29.9	24.7	0.1	178	0	-0.1
0709LCM01	273.3	175.1	-45.9	25.1	0.47	105	-0.46	-0.12
0709LCM00	286	176.4	-54.6	25.4	2.46	329	1.27	2.11
0308PIP00	290.7	198.8	-63.3	33	8.68	120	-7.51	-4.35

12 0338OER and 0490DGE

OER has already been set as an established shower, but OER03 has been marked with "Continue to (#490 DGE) December delta Eridanids." It certainly looks like that, but in fact, meteor activity that is expected to continue ahead of it has also been captured. *Figure 17 (left)* shows the radiant distribution for the period from $\lambda_{\Theta} = 195°$ to $305°$, with $(\lambda - \lambda_{\Theta}, \beta) = (185°, -37°)$ as the center. Although it is for such a long period, the radiant points are connected in an arc shape. The radiant cluster at the top of the figure is the STA, and the OER starts its activity hanging from here.

Figure 17 (right) shows the integrated radiant distribution if the radiants move along this arc. Many IAU MDCSD meteor showers exist within the range of this figure, as shown in *Table 11*. Among these, the codes for those within 3 degrees from the center are shown in red. Instead of DGE00 being removed, the activity 0709LCM is included.
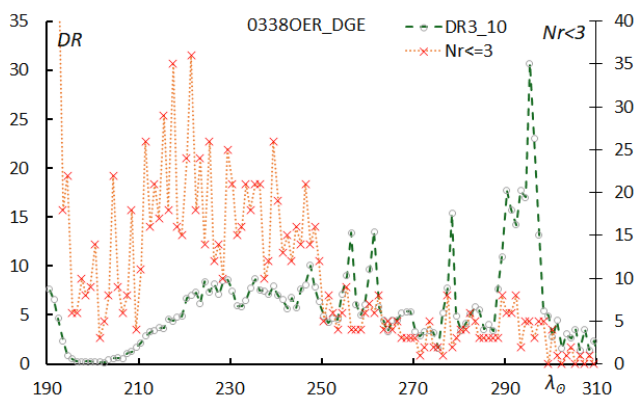
Figure 18 – The number of meteors within 3 degrees.

Furthermore, GMN describes the activities after DGE as

0308PIP, but the descriptions from 0300ZPU00 to 0318MVE00 are fragmentary visual observation reports compiled by Jenniskens from his perspective (Jenniskens, 2006). It would be unreasonable to think of 0308PIP as an extension of all activities after DGE.

Similarly, if we count the number of meteors and draw an activity profile along the arc, we get *Figure 18*. If we look at the graph of the number of meteors $Nr <= 3$ within 3 degrees from the center, it seems that the activity is at its maximum around $\lambda_{\Theta} = 230°$, but when looking at $DR3\_10$, the maximum is around $\lambda_{\Theta} = 295°$. Considering that the position of the radiant has moved considerably south and the number of meteors detected from the Northern Hemisphere will decrease, it is impossible to judge changes in activity simply by the number of meteors. On the other hand, during the first half of these meteor shower activities, there were strong activities such as not only STA but also MON and GEM, so caution is required when considering changes in DR. The reason that $DR3\_10$ decreases when $\lambda_{\Theta} < 220°$ is due to the influence of STA, and when $DR3\_20$ is used, the influence of GEM becomes strong around $\lambda_{\Theta} = 260°$. Considering these constraints, this arc-like continuous activity can be thought of as a single activity or as a combination of multiple activities. If we calculate the changes in the orbit by linking the arc-shaped activity, it appears that the perihelion direction and semi-major axis of the orbit remain fairly constant. Problems remain unsolved as into how many parts it will be divided, and whether it can be considered as a whole. As mentioned above it is currently unclear what the later stage of the activity was when the radiant point moved deep to the south, so future GMN activity in the southern hemisphere is expected.

GMN treats OER and DGE as one, but the SonotaCo Net J14 list only covers OER and does not mention DGE. GMN

considers the activity to extend up to $\lambda_\Omega = 260.5°$, but around this time the radiant distribution has entered the part where it moves southward in an arc shape.

13 0340TPY00 and 0340TPY01
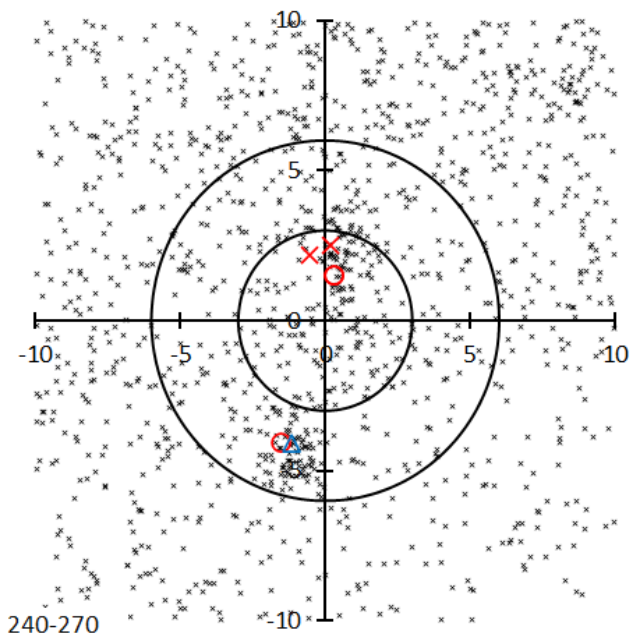
Figure 19 – Two TPYs. GMN video observations with the IAU MDCSD showers.

The IAU MDCSD has three reports for 0340TPY. The first one is from SonotaCo net in 2009, and the latter two are both from CAMS's first report (Jenniskens et al, 2016b). *Figure 19* shows the radiant distribution for the period from $\lambda_\Omega = 240°$ to $270°$, centering on $(\lambda–\lambda_\Omega, \beta) = (260°, –35°)$. Of the two TPYs, the upper one is TPY01 and 02, and the lower one is TPY00. Although the difference in position is not so large, the confusion started because the IAU MDC accepted the CAMS report as TPY01 even though they are about 15 degrees apart in solar longitude. Because of the difference between TPY00 and TPY01, they were set as working status each, so a duplicate report of "a new meteor shower" was registered.

In the J14 list of SonotaCo net, TPY00 is just TPY and TPY01 and 02 are DMH. However, in GMN, TPY00 is treated as DTP, and the pair of TPY01 and 02 is treated as TPY. Since TPY00 is reported earlier than TPY01 and 02 and before DTP, it is appropriate to use TPY00 as TPY like SonotaCo net.

In addition, in the previous paper (Koseki, 2021), these two activities were distinguished as TPY_0 and TPY_3, but since TPY03 was deleted from the IAU MDCSD, TPY_0 will remain as it is, and what used to be called TPY_3 will be referred to as TPY_1 in this paper. A new report of TPY is registered in IAUMDCSD as TPY04 that is TPY_0.

14 0096NCC and 0097SCC

Figure 20 shows the radiant point distribution for every 10 degrees in solar longitude between $\lambda_\Omega = 235°$ and $315°$, centering on $(\lambda–\lambda_\Omega, \beta) = (190°, 0°)$. The radiant distribution shows that while the radiant points of STA and NTA are moving to the right on the diagram, what appears to be a collection of radiant points remains near the center. Discussion is still ongoing as to whether these activities should be collectively called NCC or SCC, divided into several parts, or whether they should be called sporadics or ANT. It cannot be called an "established shower" like given in the IAU MDCSD.
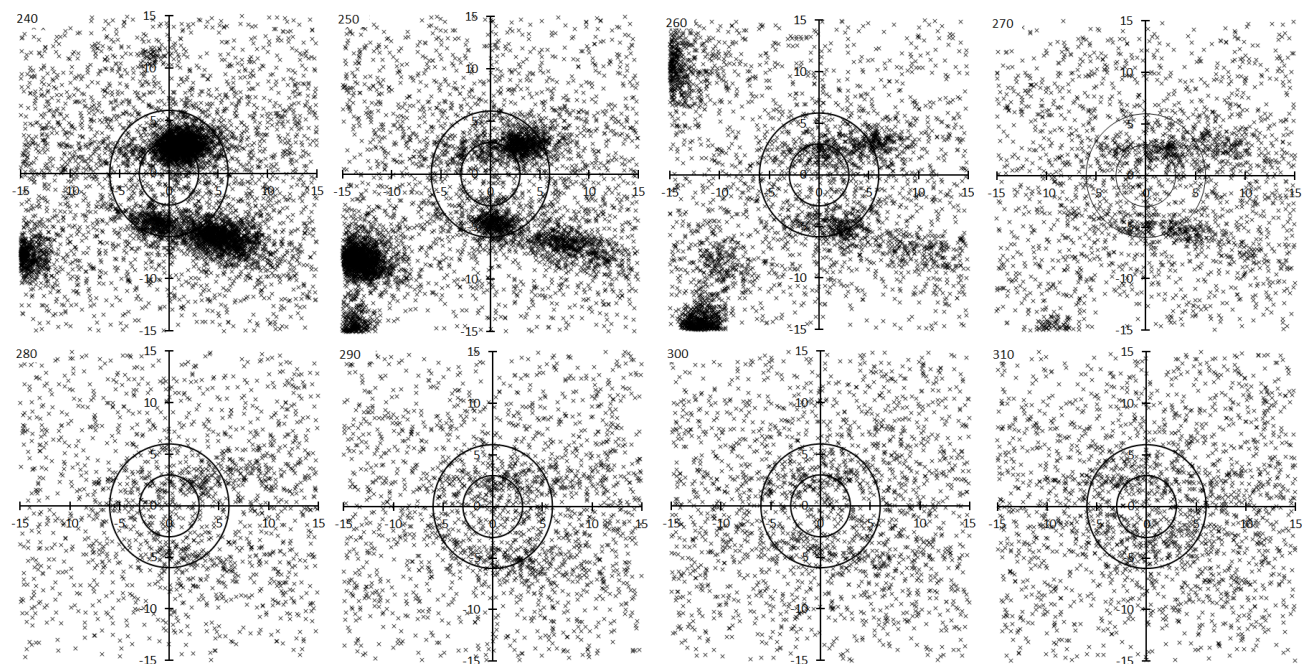
Figure 20 – From Taurids to Cancrids. Radiant distribution 10 solar longitude bin centering on $(\lambda–\lambda_\Omega, \beta) = (190°, 0°)$. The middle value for each period is shown in the upper left corner of each figure.

Table 12 – NCC and SCC in the IAU MDCSD; "ot" means observation technique.

Code	α	δ	v_g	$\lambda_\odot$	$\lambda-\lambda_\odot$	β	Notes	ot	References
0096NCC00	130	20	25.67	297	190.17	1.57	*1	V	1] Arlt R.,1995
0096NCC01	134.19	14.2	26.7	300.2	192.38	-2.94	*2	R	2] Nilsson, 1964
0096NCC02	126.72	19.92	28	297.1	187.11	0.73	*3	P	3] Lindblad, 1971
0096NCC03	124.83	20.92	25.8	292.9	189.35	1.3	*4	R	4] Sekanina, 1973
0096NCC04	130.52	19.71	26.4	297.1	190.62	1.42	*5	R	5] Sekanina, 1976
0096NCC05	131.4	17.6	27.73	299	190.08	-0.4	*6	V	6] Molau et al., 2013
0096NCC06	127.6	21.5	27.2	296	188.63	2.47	*7	T	7] Jenniskensetal., 2016
0096NCC08	128.6	20.4	28.2	296.9	188.9	1.63		T	9) Shiba, 2022.
0097SCC00	131.68	11.91	24.36	305.7	185.15	-5.82	*8	P	1] Terentjeva, 1989
0097SCC01	118.87	7.63	24	297	182.41	-12.91	*9	R	2] Nilsson, 1964
0097SCC02	131.5	10.6	26.43	298	193.02	-7.13	*10	T	3]Molau & Rendtel, 2009
0097SCC03	125	14.4	27	296	187.9	-5.02	*11	T	4] Jenniskens et al., 2016
0097SCC05	117.5	16.1	27.9	287.1	189.34	-4.85		T	6) Shiba, 2022.

Notes:
*1: In Arlt 1995 the shower name is delta-Cancrids, member of delta-Cancsrids group (#95 in 2006 PJ)
*2: In Nilsson 1964, Tab 4 radiant 61.1.1, member of delta-Cancrids group (#95 in 2006 PJ)
*3: member of 96
*4: In Sekanina 1973, the shower name is delta-Cancrids (p. 255 & 258) member of delta-Cancrids group (#95 in PJ 2006)
*5: In Sekanina 1976, the shower name is delta-Cancrids (Tab. VI, p. 274), member of delta-Cancrids group (#95 in PJ 2006)
*6: member of 95/DCA group
*7: ecliptic antihelion source, member of delta-Cancrids group (#95 in PJ2006)
*8: In Terentjeva 1989 in Tab.1 alpha-Cnc(a), member of delta-Cancrids group (#95 in PJ2006)
*9: In Nilsson 1964, Tab 4 radiant 61.1.2,, member of delta-Cancrids group (#95 in PJ2006)
*10: ecliptic antihelion source, twin of 204/DXL, member of delta-Cancrids group (#95 in PJ2006)
*11: ecliptic antihelion source, twin of 204/DXL, member of delta-Cancrids group (#95 in PJ2006)

Table 12 lists what is considered NCC and SCC in the IAU MDCSD. The notes section is lively, showing that this activity can be interpreted in any number of ways. It can be seen that various interpretations have been made by researchers since the 1960s (Koseki, 2023b). The fact that Terentjeva's most important work is not cited in the IAU MDCSD is an indication of the bias of the material; Терентьева, А.К., 1966, 'Исследование Метеоров', No.1, 62-132.

In any case, $(\lambda-\lambda_\odot, \beta) = (190°, 0°)$ is at the center of ANT, and it is unclear what NCC or SCC refers to. Although NCC and SCC were listed in the previous meteor shower table (Koseki, 2021), they are excluded in this article. NCC and SCC are not featured in SonotaCo net J14 list either. On the other hand, GMN lists both.

Acknowledgment

References

Asher D. J. and Clube S. V. M. (1993). "An extraterrestrial influence during the current glacial-interglacial". *Quarterly Journal of the Royal Astronomical Society*., **34**, 481–511. See also "Taurid swarm years", http://www.cantab.net/users/davidasher/taurid/swarmyears.html.

Denning W.F. (1899). "General Catalogue of the Radiant Points of Meteoric Showers and of Fireballs and Shooting Stars observed at more than one station". *Memoirs of the Royal Astronomical Society*, **53**, 201–293.

Ellyett C. D. and Roth K. W. (1955). "The Radar Determination of Meteor Showers in the Southern Hemispheres". *Australian Journal of Physics*, **8**, 390–401.

Jacchia L. G., and Whipple F. L., (1961). "Precision orbits of 413 photographic meteors". *Smithsonian Contributions to Astrophysics*, **4**, 97–129.

Jenniskens P. (2006). Meteor Showers and their parent comets, Cambridge.

Jenniskens P., Nénon Q., Albers J., Gural P. S., Haberman B., Holman D., Morales R., Grigsby B. J., Samuels D. and Johannink C. (2016a). "The established meteor showers as observed by CAMS". *Icarus*, **266**, 331–354.

Jenniskens P., Nénon Q., Gural P.S., Albers J., Haberman B., Johnson B., Holman D., Morales R., Grigsby B.J., Samuels D., Johannink C. (2016b). "CAMS confirmation of previously reported meteor showers". *Icarus*, **266**, 355–370.

Koseki M. (2009). "Meteor Shower Records: A Reference Table of Observations from Previous centuries". *WGN, the Journal of the IMO*, **37**, 139–160.

Koseki M. (2012). "Three components of 'Taurids'". *WGN, the Journal of the IMO*, **40**, 129–138.

Koseki M. (2020). "Three components of 'Taurids' II". *WGN, the Journal of the IMO*, **48**, 36–46.

Koseki M. (2021). "The activity of meteor showers recorded by SonotaCo Net video observations 2007–2018". *eMetN Meteor Journal*, **6**, 91–246.

Koseki M. (2022). "Global Meteor Network: Outburst produced by dust from 73P/Schwassmann-Wachmann3". *eMetN Meteor Journal*, **7**, 369–378.

Koseki M. (2023a). "Major meteor showers based on Global Meteor Network data". *eMetN Meteor Journal*, **8**, 231–245.

Koseki M. (2023b). "Remaining problems in IAUMDC Shower Database (SD)". *eMetN Meteor Journal*, **8**, 288–309.

Koseki M. (2024). "Meteor shower data from video observation, Part I, Research methods and summary of survey results". *eMetN Meteor Journal*, **9**, 166–183.

Southworth R. B. and Hawkins G. S. (1963). "Statistics of meteor streams". *Smithsonian Contributions to Astrophysics*, **7**, 261–285.

Vida D., Gural P., Brown P., Campbell–Brown M., Wiegert P. (2019). "Estimating trajectories of meteors: an observational Monte Carlo approach – I. Theory". *Monthly Notices of the Royal Astronomical Society*, **491**, 2688–2705.

Vida D., Gural P., Brown P., Campbell–Brown M., Wiegert P. (2020). "Estimating trajectories of meteors: an observational Monte Carlo approach – II. Results". *Monthly Notices of the Royal Astronomical Society*, **491**, 3996–4011.

Vida D., Šegon D., Gural P. S., Brown P. G., McIntyre M. J. M., Dijkema T. J., Pavletić L., Kukić P., Mazur M. J., Eschman P., Roggemans P., Merlak A., Zubrović D. (2021). "The Global Meteor Network – Methodology and first results". *Monthly Notices of the Royal Astronomical Society*, **506**, 5046–5074.

Whipple F.L. (1940). "Photographic Meteor Studies. III. The Taurid Shower". *Proceeding of the American Philosophical Society*, **83**, No.5, 711–745.

Wright F. W., Jacchia L. G., and Whipple F. L. (1957). "Photographic ι-Aquariid meteors and evidence for the northern ι Aquariids". *Astronomical Journal*, **62**, 225–233.

51-Sagittids meteor shower confirmed by CAMS

**P. Jenniskens, M. Odeh, C. Johannink, M. Breukers, J. Baggaley, J. Scott,
N. Moskovitz, T. Cooper, H. Devillepoix, D. Rollinson, and D. Samuels**

SETI Institute, 339 Bernardo Ave, Mountain View, CA 94043, USA
`pjenniskens@seti.org`

The newly detected 51-Sagittids shower reported last year from Global Meteor Network observations was visible in single night CAMS data for May 14–15, 2024. The shower appears to be a weak annual shower from a yet-to-be-discovered long-period comet. The shower was also detected by CAMS in prior years.

1   Introduction

Last year, Vida et al. (2023) reported the detection by the Global Meteor Network of a possible new shower with a radiant in Sagitta on a single night in May. The shower was designated M2023-K1. Subsequently, the shower was given the provisional name 51-Sagittids and Lunsford (2024) called attention to the shower in the weekly shower call for new observations. When the shower was clearly detected in single-night CAMS data this year at the website[7], Lunsford alerted us to this confirmation. Here, we report on that detection, confirming it as a sighting of a yet-to-be-discovered long-period comet.

2   Observations

Figure 1 shows the radiants of meteors detected in the CAMS network during the 5-day solar longitude interval 52 – 57 degrees (Equinox J2000), roughly corresponding to the dates of May 14–18. The radiants are given in Sun-centered ecliptic coordinates and plotted similar to such maps in Jenniskens (2023). The shower is clearly detected as a concentration of radiants in the northern apex source. The radiant distribution shows a daily drift in Sun-centered coordinates and sharpens up slightly after correction (Jenniskens, 2023), the result shown here. Vida et al. (2023)
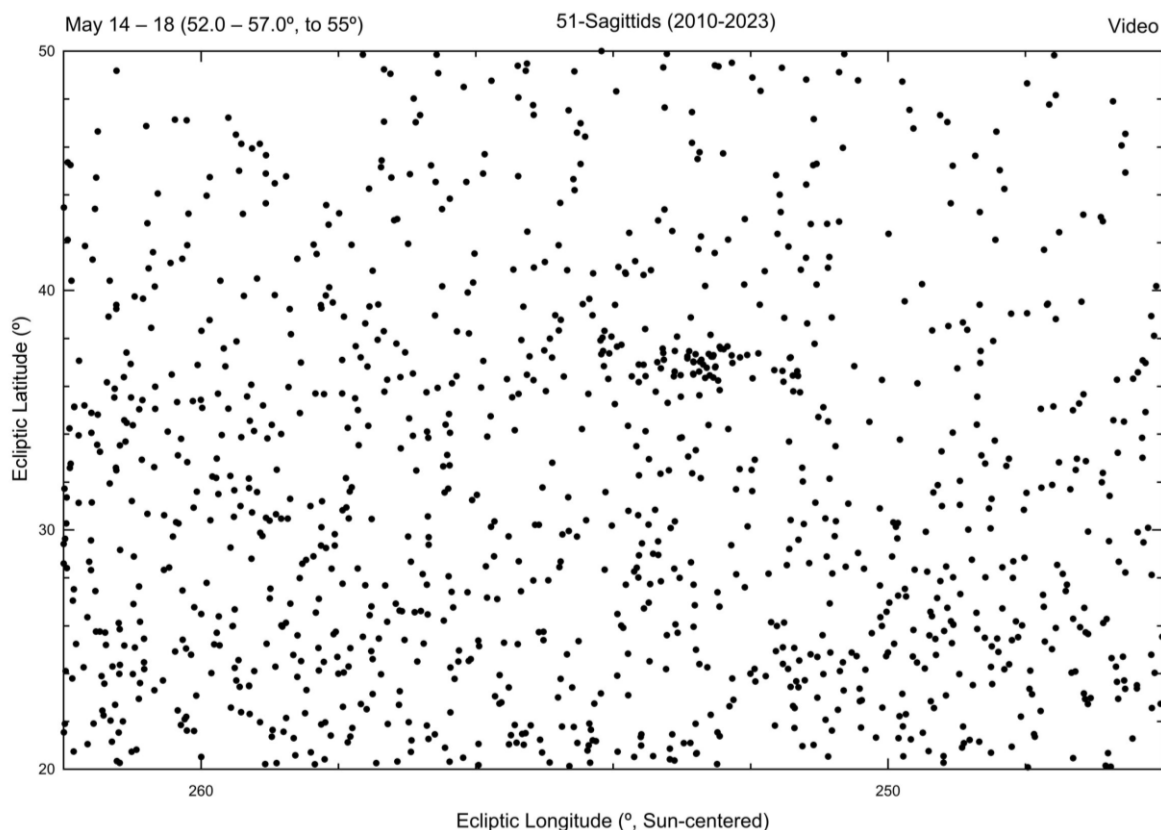
Figure 1 – Radiant map in the region around the 51-Sagittids radiant during the shower's activity period from past 2010–2023 CAMS observations (Jenniskens, 2023).

---

[7] http://cams.seti.org/FDL/

May 14 – 18 (52.0 – 57.0º, to 55º)   51-Sagittids (2024)   Video
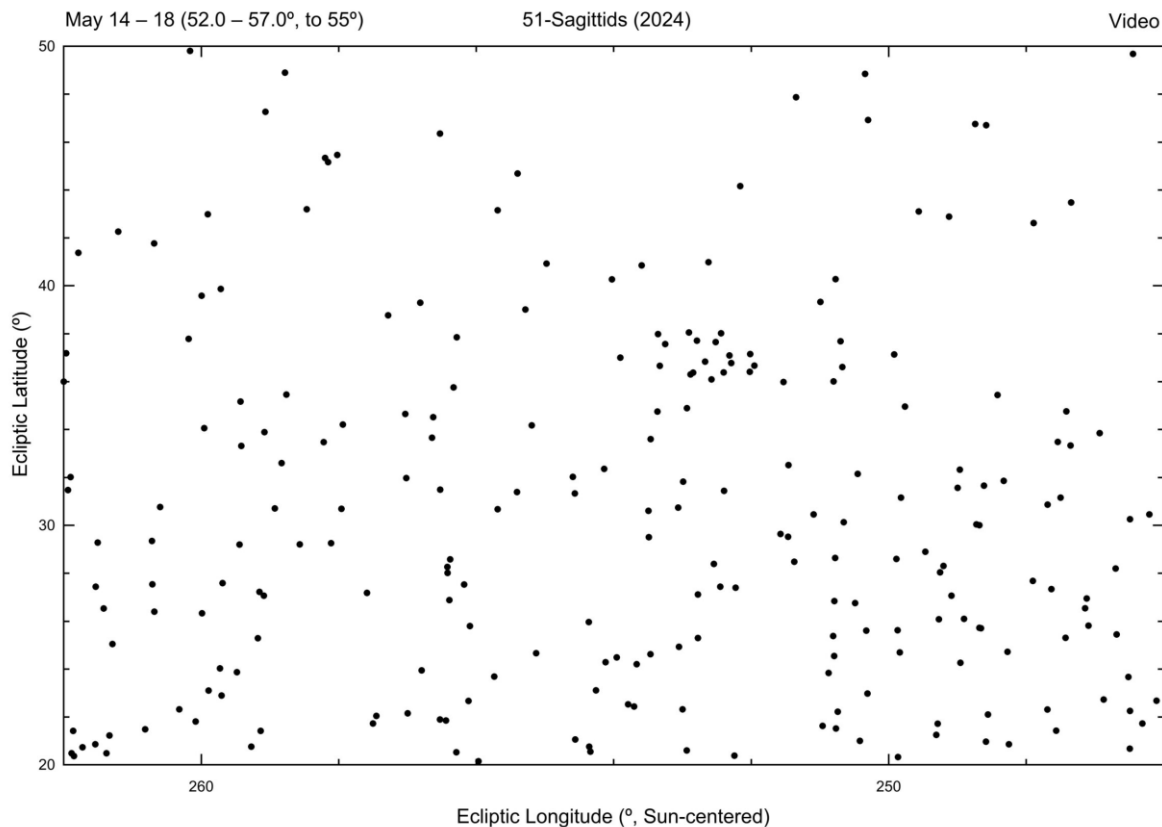
Figure 2 – Same as Figure 1, but for the CAMS observations in 2024.

already reported that the shower was detected in prior years of the Global Meteor Network as well as in the results from the SonotaCo and EDMOND low-light video camera networks.

Figure 2 shows the data from the CAMS networks in 2024 in a similar plot. The shower is clearly detected. Table 1 gives the median orbital elements and their 1-sigma dispersion. The first meteor was detected on May 14 at 18^{h}38^m UTC, and the shower was last seen on May 17 at 01^{h}11^m UTC.

The shower is very weak and observations are from a number of CAMS networks, mostly reflecting the local weather conditions. 6 meteors were detected by the United Arab Emirates Astronomical Camera Network, coordinated by M. Odeh. 5 meteors were detected by CAMS-BeNeLux, coordinated by C. Johannink and M. Breukers. 3 meteors were detected by CAMS New Zealand, coordinated by J. Baggaley (University of Canterbury) and J. Scott (University of Otago). 3 meteors were detected by LO-CAMS, coordinated by N. Moskovitz (Lowell Observatory). 1 meteor was detected by CAMS South Africa, coordinated by T. Cooper, and 1 meteor was detected by CAMS Australia, coordinated by H. Devillepoix (Curtin University) and D. Rollinson.

3 Discussion

Observations in 2024 do not suggest that there was an outburst. The number of detected meteors was, starting in 2011: 0, 3, 1, 1, 0, 0, 2, 6, 5, 11, 7, 6, 8, and 19. The increase in the number over the years reflects the increasing number of cameras deployed. This appears to be an annual shower. In prior years, the shower was first detected as early as May 14 at 7^{h}28^m UTC and last seen on May 18 at 8^{h}24^m UTC. The median solar longitude of this year's observations was at a similar time to that of prior years (Table 1).

Table 1 – The median orbital elements (Equinox J2000.0) of the 51-Sagittids compared to the 2023 observations reported by Vida et al. (2023).

	51-Sagittids GMN: 2023	51-Sagittids CAMS: 2010–2023	51-Sagittids CAMS: 2024
λ_Θ (°)	54.5	54.8 ± 1.1	54.4 ± 0.6
α_g (°)	300.3	300.7 ± 1.6	300.1 ± 1.1
δ_g (°)	+17.8	+17.4 ± 0.7	+17.2 ± 0.7
v_g (km/s)	59.7	59.2 ± 1.2	58.9 ±. 1.2
$\lambda - \lambda_\Theta$ (°)	252.8	252.8 ± 1.0	252.3 ± 1.1
β (°)	+37.4	+37.0 ± 0.7	+37.0 ± 0.6
a (AU)	300.9	17.7	12.6
q (AU)	0.903	0.897 ± 0.015	0.891 ± 0.018
e	0.997	0.949 ± 0.085	0.929 ± 0.093
ω (°)	218.2	219.4 ± 3.2	220.6 ± 3.8
Ω (°)	54.4	54.7 ± 1.1	54.4 ± 0.6
i (°)	113.5	113.9 ± 1.4	113.4 ± 1.2
Π (°)	272.6	274.6 ± 2.9	275.9 ± 3.8
T_J	–0.45	–0.23	–0.07
N	15	65	19

The relatively high semi-major axis points to a long-period comet being the source of this shower. The orbital period is likely more than 250 years and less than 4000 years (Jenniskens et al., 2021). In the coming years, it deserves to pay attention to this radiant to see if outbursts can be detected. At present, we know that the source is a long-period comet. If the 1-revolution dust trail of this comet wanders in Earth's path on occasion, which is expected to happen only once or twice every 60 years if the comet orbit passes close enough to Earth (Lyytinen & Jenniskens, 2003), then this would make this comet a Potentially Hazardous Comet.

References

Jenniskens P., Lauretta Dante S., Towner M. C., Heathcote S., Jehin E., Hanke T., Cooper T., Baggaley J. W., Howell J. A., Johannink C., Breukers M., Odeh M., Moskovitz N., Juneau L., Beck T., De Cicco M., Samuels D., Rau S., Albers J., Gural P. S. (2021). "Meteor showers from long-period comets". *Icarus*, **365**, article id.114469.

Jenniskens P. (2023). Atlas of Earth's Meteor Showers. Elsevier, USA. 838 pp.

Lunsford B. (2024). "Meteor activity outlook for May 11-17, 2024." American Meteor Society website: https://www.amsmeteors.org/2024/05/meteor-activity-outlook-for-may-11-17-2024/ (last accessed May 22, 2024).

Lyytinen E., Jenniskens P. (2003). "Meteor outbursts from long-period comet dust trails." *Icarus*, **162**, 443–452.

Vida D., Segon D., Roggemans P. (2023). "A possible new meteor shower in Sagitta." *eMetN Meteor Journal*, **8**, 246–251.

April outburst of iota-Herculids has an associated annual shower

Peter Jenniskens and Stu Pilorz

SETI Institute, 339 Bernardo Ave, Mountain View, CA 94043, USA
pjenniskens@seti.org

The new April 27–28 shower in Hercules reported from GMN observations is found to have a weak associated annual shower in past CAMS data.

1 Introduction

Last week, Vida and Šegon (2024) reported the detection by the Global Meteor Network of a brief meteor outburst from a shower in the constellation Hercules in the night of April 27–28, 2024. The shower was given the designation M2024-H1. The shower was not reported in the past and is therefore not included in the recent Atlas of Earth's Meteor Showers (Jenniskens, 2023). The shower radiates from near the 4th magnitude star iota-Herculis, therefore a suitable provisional name is iota-Herculids (IHE). The shower only lasted about 4 hours, with activity between solar longitudes 37.70 and 37.85 degrees narrowly concentrated around 37.80 degrees.

2 Observations

The 2024 outburst was not detected by the global CAMS networks because of overcast conditions in the BeNeLux and in Turkey. We examined the past CAMS observations and found that there is a weak annual shower at this position in ecliptic longitude and latitude that stands out by having slightly higher velocities than the nearby sporadic background. In total, 33 shower members were identified over the solar longitude interval 35.7 to 39.1 degrees. The number of detected shower members for each year since 2011 was: 0, 0, 0, 1, 1, 0, 1, 2, 4, 5, 9, 4, 6, 0. Some of the gradual increase in numbers is on account of more cameras participating in the network, with the more recent years showing activity annually. The median orbital elements (with 1-sigma dispersions uncorrected for observational uncertainty) are listed in *Table 1*.
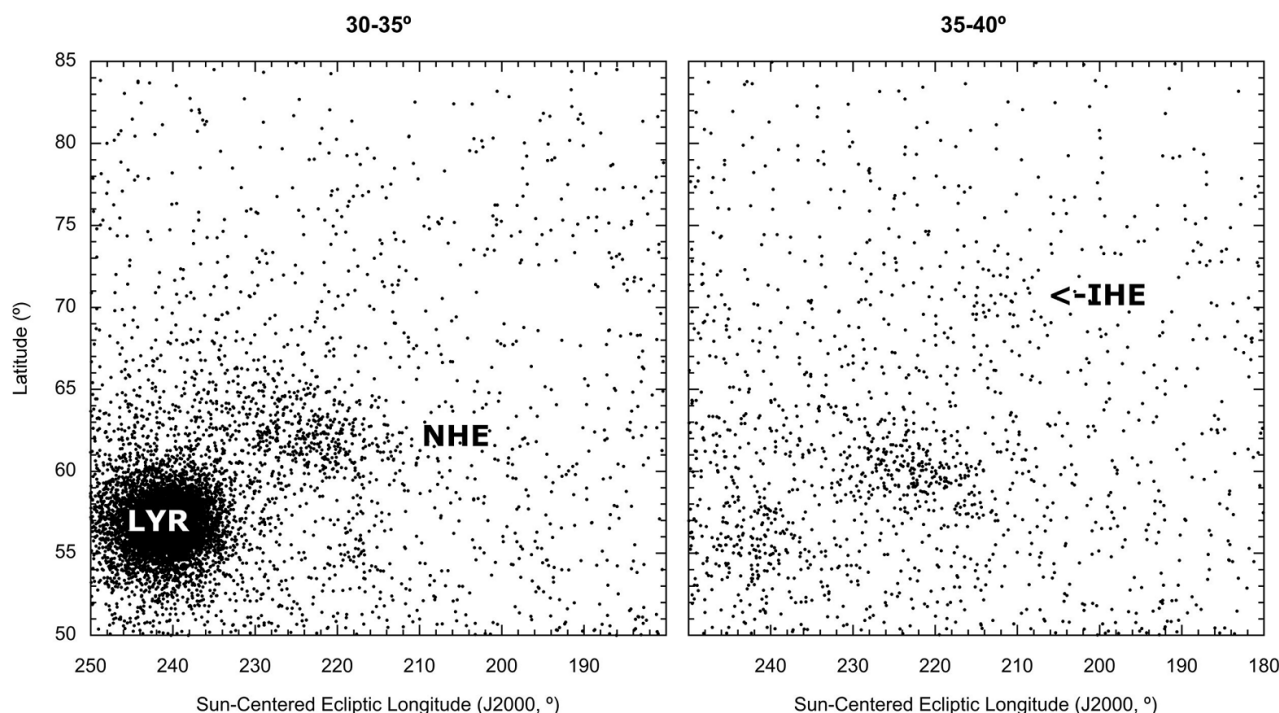
Figure 1 – The plot of the radiants obtained by the CAMS networks during 2010–2024 for the solar longitude interval 30–35º (left) and 35–40º (right). The weak iota-Herculids are marked in the right diagram. Other showers in this region are the April Lyrids (LYR) and nu-Herculids (NHE).

Table 1 – The median orbital elements (Equinox J2000.0) compared to the 2024 outburst orbit from Vida and Šegon (2024).

	IHE outburst GMN: 2024	IHE annual shower CAMS:2014–2023
$\lambda_{\odot}$ (°)	37.8	37.8 ± 0.8
α_g (°)	261.1	260.9 ± 1.7
δ_g (°)	47.3	+48.2 ± 1.3
v_g (km/s)	35.6	35.4 ± 2.1
$\lambda - \lambda_{\odot}$ (°)	214.24	212.9 ± 3.1
β (°)	70.15	+70.8 ± 1.4
a (AU)	29.8	18
q (AU)	0.953 ± 0.005	0.956 ± 0.009
e	0.968 ± 0.068	0.947 ± 0.136
ω (°)	206.97 ± 1.55	206.4 ± 2.4
Ω (°)	37.819 ± 0.025	37.8 ± 0.8
i (°)	55.77 ± 1.02	55.2 ± 2.2
Π (°)	244.79 ± 1.58	244.0 ± 2.5
T_J	0.85	0.97
N	25	33

3 Discussion

The annual shower was also detected by the SonotaCo network, with 6 meteors radiating from this direction and with this speed spread over the years 2007 (2), 2012 (1), 2013 (1), 2017 (1) and 2019 (1), all from the nights April 26–28.

The source of the shower was identified as a Halley-type shower by Vida and Šegon (2024) based on the measured orbital elements. Indeed, the Tisserand parameter is in the range of Mellish-type comet showers (Jenniskens, 2023). However, the fact that the velocity of meteors is slightly higher on average than the sporadic background before and after the shower suggests that the meteors move in a long-period comet orbit. A Halley-type comet might be expected to have a more intense associated annual shower if it is trapped or librates about a mean-motion resonance. If due to a prograde long-period comet, the sighting in 2024 makes it possible to predict when the next outburst is expected (Lyytinen and Jenniskens, 2003).
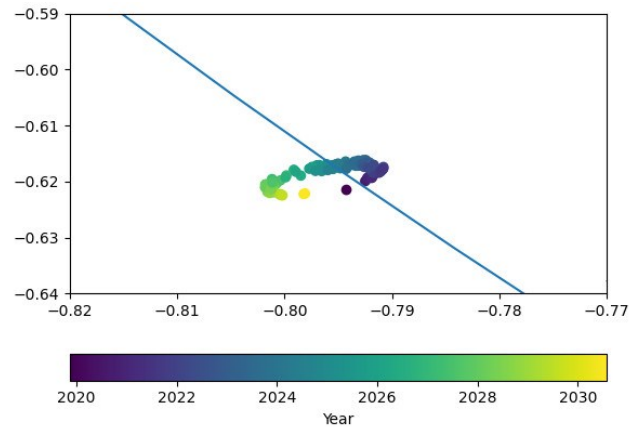
Figure 2 – The motion of the iota-Herculids dust trail relative to Earth's orbit between 2020 and 2030.

Figure 2 shows the calculated motion of the dust trail relative to Earth's orbit, starting from the orbit for the outburst iota-Herculids in Table 1, assuming that this orbit describes the center of the dust trail. Adjusting the orbital period to that of a typical long-period comet, between 250 y ($e = 0.976$) and 4000 y ($e = 0.996$) (Jenniskens et al., 2021), results in a similar pattern. Coordinates are in units of AU and the color scale is in decimal years. From this, it appears that the dust trail was close to Earth's orbit previously in late 2020 (but not in April that year) and will not return until the early 2030's. The first likely return will be on 2033 April 28 at around 00^h21^m UTC (solar longitude 37.584º, J2000).

References

Jenniskens P., Lauretta Dante S., Towner M. C., Heathcote S., Jehin E., Hanke T., Cooper T., Baggaley J. W., Howell J. A., Johannink C., Breukers M., Odeh M., Moskovitz N., Juneau L., Beck T., De Cicco M., Samuels D., Rau S., Albers J., Gural P. S. (2021). "Meteor showers from long-period comets". Icarus, 365, article id.114469.

Jenniskens P. (2023). Atlas of Earth's Meteor Showers. Elsevier, USA. 838 pp.

Lyytinen E., Jenniskens P. (2003). "Meteor outbursts from long-period comet dust trails". Icarus, 162, 443–452.

Vida D., Segon D. (2024). "New Shower in Hercules". eMetN Meteor Journal, 9, 161–164.

April 2024 report CAMS-BeNeLux

Carl Johannink

Am Ollenkamp 4, 48599 Gronau, Germany
c.johannink@t-online.de

A summary of the activity of the CAMS-BeNeLux network during the month of April 2024 is presented. This month was good for 8566 multi-station meteors resulting in 2672 orbits.

1   Introduction

Meteor activity in April is still at a low level for northern latitudes. But with the Lyrids around April 22nd, we welcome the first well-known yearly meteor shower since the Quadrantids in early January.

2   April 2024 statistics

Weather in April remained very unsettled in this month. Although we could collect orbits in all nights, except during April 18–19, there were many nights with only partly clear conditions. Clear weather at all stations in the BeNeLux was, like nearly all months since October 2023 very rare.

Only in four nights we could collect more than 200 orbits: April 1–2, 21–22, 22–23 and 28–29. So at least then we benefited from better conditions. We could collect 629 orbits during the nights April 21–22 and April 22–23, mostly Lyrid meteors, as can be seen in *Figure 1*.
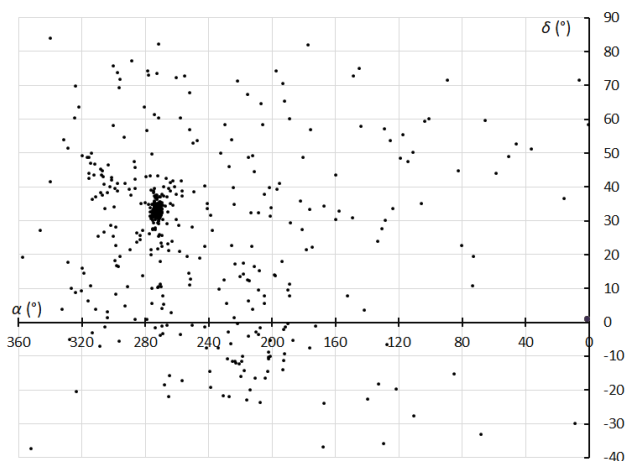
Figure 1 – Radiant plot of all orbits captured by CAMS-BeNeLux during April 21–22 and April 22–23, 2024.

CAMS-BeNeLux captured 8566 meteors multi-station. This resulted in 2672 orbits. 51,5% of the multi-station meteors, were captured by at least 3 cameras.

On average, 116 cameras were active every night in April. A greater number than last year because the number of stations and camera is still growing in our network. This month, at Dourbes four additional RMS cameras were installed by Hervé Lamy.
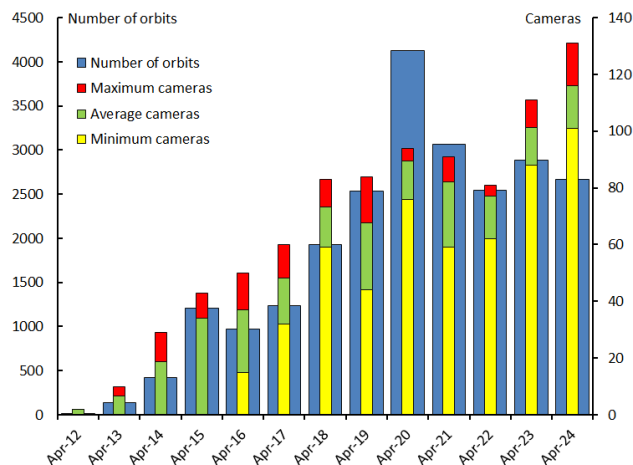
Figure 2 – Comparing April 2024 to previous months of April in the CAMS-BeNeLux history. The blue bars represent the number of orbits, the red bars the maximum number of cameras capturing in a single night, the green bars the average number of cameras capturing per night and the yellow bars the minimum number of cameras.

Table 1 – Number of orbits and active cameras in CAMS-BeNeLux during the month of April in the period 2012–2024.

Year	Nights	Orbits	Stations	Max. Cams	Min. Cams	Mean Cams
2012	6	11	4	2	–	2.0
2013	19	140	9	10	–	6.5
2014	19	421	12	29	–	18.8
2015	27	1212	15	43	–	33.9
2016	26	971	17	50	15	37
2017	28	1235	20	60	32	48.2
2018	27	1929	21	83	59	73.3
2019	29	2538	20	84	44	67.7
2020	29	4128	25	94	76	89.4
2021	28	3061	27	91	59	82.1
2022	27	2543	24	81	62	77.2
2023	29	2888	36	111	88	101.4
2024	29	2672	45	131	101	116.0
Total	323	23749				

At least 101 cameras were active each night. Comparing this number with the number of archived orbits, this confirms the impression that the weather was very changeable.

3   Conclusion

This is the fourth best result compared with all other April months, especially due to a larger number of cameras in our network.

Acknowledgment

May 2024 report CAMS-BeNeLux

Carl Johannink

Am Ollenkamp 4, 48599 Gronau, Germany
c.johannink@t-online.de

A summary of the activity of the CAMS-BeNeLux network during the month of May 2024 is presented. This month was good for 10084 multi-station meteors resulting in 2993 orbits.

1   Introduction

In addition to the ever-present sporadic activity, this month is best known for having one of the most active meteoroid streams in the Southern Hemisphere: the eta Aquariids (May 6). Even from our latitudes we can observe activity from this meteor shower.

2   May 2024 statistics

Fortunately, this month brought generally better conditions than what we got in the previous months. Especially during the second week of May we could collect many orbits, from May 6–7 up to May 13–14 a total of 1523 orbits.

Around May 14, weather resumed the cloudier pattern we faced already so many months since October last year. This trend was confirmed by the fact that only in 2 nights during the second half of May we could collect more than 100 orbits. A poor result compared with 10 nights with more than 100 orbits in the first half of May.
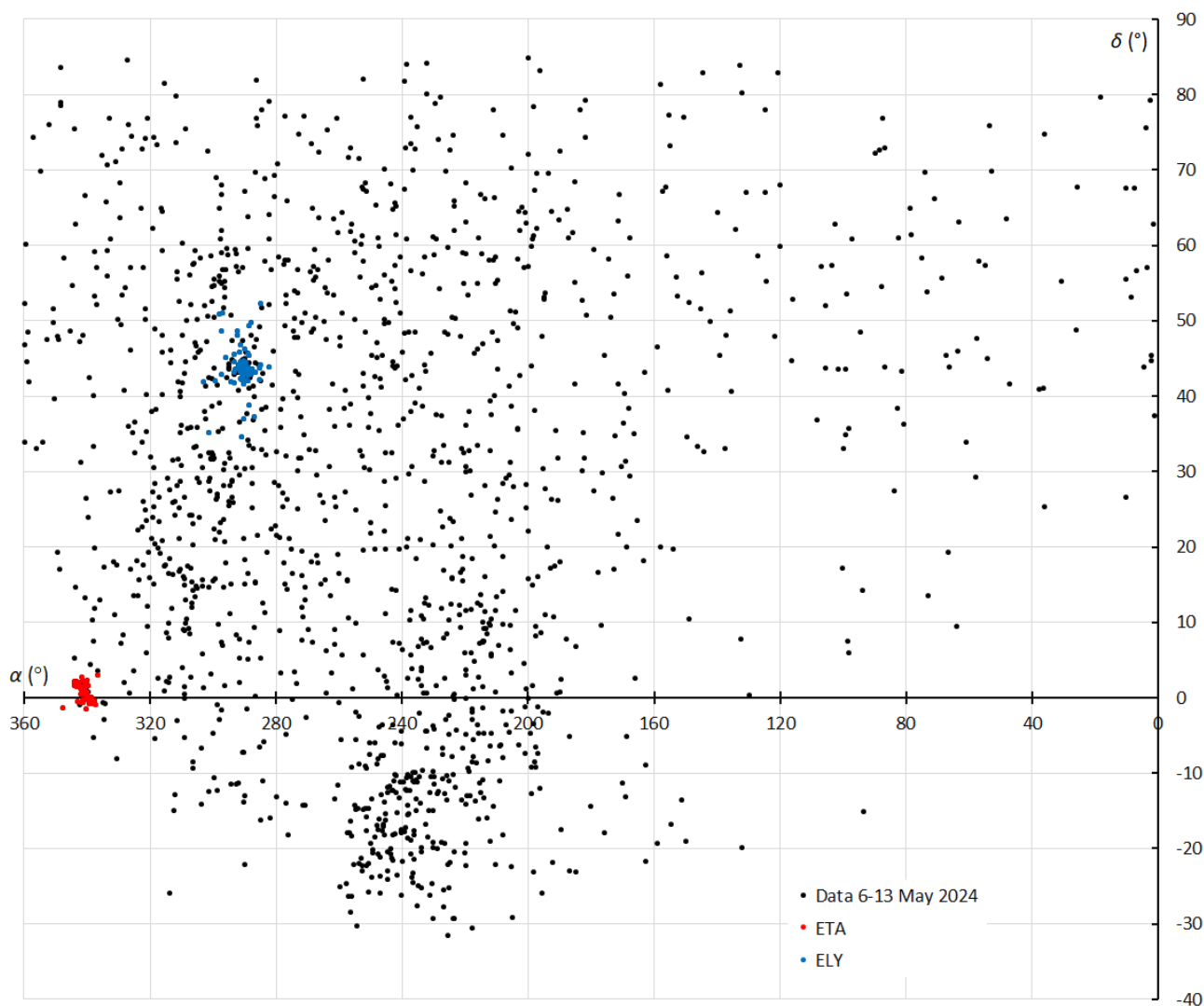
Figure 1 – Radiantpositions of all simultaneous meteors during May 6–14 (data CAMS-BeNeLux).
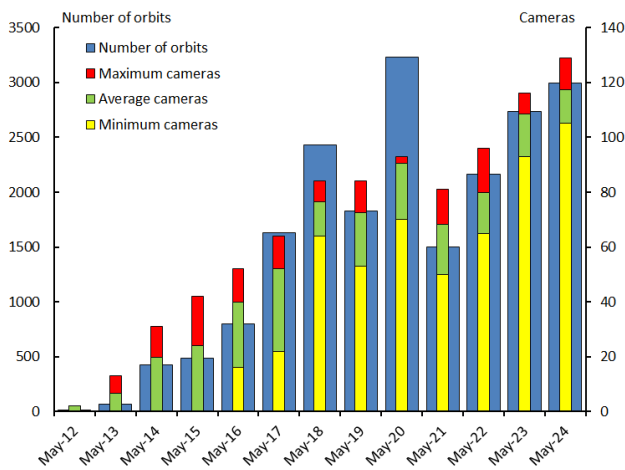
Figure 2 – Comparing May 2024 to previous months of May in the CAMS-BeNeLux history. The blue bars represent the number of orbits, the red bars the maximum number of cameras capturing in a single night, the green bars the average number of cameras capturing per night and the yellow bars the minimum number of cameras.

Table 1 – Number of orbits and active cameras in CAMS-BeNeLux during the month of May in the period 2012–2024.

Year	Nights	Orbits	Stations	Max. Cams	Min. Cams	Mean Cams
2012	5	13	4	2	–	2
2013	13	69	9	13	–	6.8
2014	22	430	13	31	–	19.7
2015	25	484	15	42	–	24.2
2016	26	803	17	52	16	39.9
2017	24	1627	19	64	22	52.0
2018	31	2426	21	84	64	76.6
2019	29	1825	20	84	53	72.4
2020	29	3226	24	93	70	90.5
2021	28	1500	25	81	50	68.2
2022	30	2160	28	96	65	79.8
2023	30	2734	36	116	93	108.6
2024	31	2993	45	129	105	117.4
Total	262	20290				

CAMS-BeNeLux collected a total of 10084 multi-station meteors, resulting in 2993 orbits. More than 50% of this score was achieved in the first half of May.

On average, 117 cameras were active during each night. On May 8–9, 129 cameras picked up data, in other nights at least 105 cameras (*Table 1* and *Figure 2*).

The beautiful weather in the period 6 to 13 May also allowed that we were able to capture quite a few eta Aquariids. In *Figure 1* all radiant positions of the 1523 orbits collected from May 6 up to May 14 are plotted. Red colored radiant positions refer to eta Aquariids meteors (ETA).

But we also see a concentration of radiants near RA = 285° and Decl. = 43°. These meteors belong to the eta Lyrid meteoroid stream (ELY), active from May 5–15 (Jenniskens, 2023), which coincided with exactly the period with clear skies in our regions. Meteor shower identification was done using of the Drummond criterium.

3 Conclusion

This month gave the second-best result of all months of May so far. Only in May 2020 we could collect more orbits (3226). Most clear nights were around the ETA-maximum then.

Acknowledgment

3902, 3903, 3904, 3905, 3906 and 3908), *Holger Pedersen* (Otterup, Denmark, RMS 3501), *Eduardo Fernandez del Peloso* (Ludwigshafen, Germany, RMS 3805), *Tim Polfliet* (Gent, Belgium, Watec 396, RMS 3820, 3840 and 3846), *Steve Rau* (Oostende, Belgium, RMS 3822), *Steve Rau* (Zillebeke, Belgium, Watec 3850 and 3852, RMS 3851 and 3853), *Paul and Adriana Roggemans* (Mechelen, Belgium, RMS 3830 and 3831, Watec 3832, 3833, 3834, 3835, 3836 and 3837), *Jim Rowe* (Eastbourne, England, RMS 3703), *Philippe Schaack* (Roodt-sur-Syre, Luxemburg, RMS 3952), *Romke Schievink* (Bruchhausen Vilsen, Germany, RMS 3808 and 3809),*Hans Schremmer* (Niederkruechten, Germany, Watec 803), *Rob Smeenk* (Assen, Netherlands, RMS 3196), *Rob Smeenk* (Kalenberg, Netherlands, RMS 3192, 3193, 3194 and 3195), *Erwin van Ballegoij* (Heesh, Netherlands Watec 3148 and 3149), *Andy Washington* (Clapton, England, RMS 3702).

References

Jenniskens P. (2023). Atlas of Earth's Meteor Showers, pages 55–57.

What CARMELO can observe

Lorenzo Barbieri

Associazione Astrofili Bolognesi (AAB), Italy
barbieriofiuco@gmail.com

The CARMELO (Cheap Amateur Radio Meteor Echoes LOgger) network made of cheap and homemade receivers created so far, although small, shows the potential of this innovative project in the field of meteor observation using the meteor scatter method.

The system measures and represents waveforms and frequency of every single meteor echo received in a way never seen before by any amateur observer.

This article describes some types of waveforms displayed by the system and analyses, if present, the head echo, highlighting its Doppler shift. A possible methodology for calculating the speed of the meteor as a function of the distance travelled by the radio echo is also described.

It also shows the overlap of the measurements carried out on the same event by different observers by recording the temporal sequence and hypothesizes a method for calculating the meteor speed starting from the delay times recorded by each individual observation.

1 What is CARMELO?

The CARMELO project for radio meteor reception is described on the main page of the CARMELO website[8]. Another description appeared in this Journal (Barbieri and Brando, 2022), while the description of its first months of operation were published in the same Journal (Barbieri et al., 2023).

To briefly summarize here what is described in the aforementioned articles, CARMELO (Cheap Amateur Radio Meteor Echoes LOgger) essentially consists of two units: the receiving device and the server that processes the data received.

The device:

The apparatus consists of a receiver which cost is affordable for the majority of interested amateur astronomers or radio amateurs and it is entirely digital. Unlike all other amateur meteor scatter experiences, with the CARMELO radio receivers no personal computers are needed.

Consequently, the observations made from multiple observers are of the same type and recorded with the same standard. A microprocessor (Raspberry) essentially performs three functions:

- Operates an SDR (Software Defined Radio) dongle that tunes to the user's chosen transmitter frequency.
- Samples the radio signal, calculates its FFT, measuring amplitude and frequency and recognizes the presence of a meteor echo. As a result, the interference and satellite signals are not detected.
- Writes data to a log file which is transferred to the server.

The device must be connected to an antenna suitable for receiving the chosen frequency, correctly oriented and positioned in an open place and as far as possible from the ground or buildings. It must also be connected to a modem that allows access to the internet.

The server:

The server receives data in real time. Since the data is generated by identical equipment and identical software, all is based on a single standard and therefore compatible with each other.

The server generates some pages which are available to the user. In these pages you can find:

- The distribution of CARMELO receivers across the territory.
- The statistic of the number of events recorded hour by hour in which it is possible to recognize the trend of the meteor shower activity.
- Each recorded event of the current week is graphically represented in order to identify for each: signal the amplitude, echo duration and the observer.
- By choosing a single meteor in this graphic representation, the user can open a new page which graphically represents the two measured data with the FFT: namely the waveform and the received frequency.
- If the chosen meteor has been observed by more than three observers simultaneously, the user can superimpose the various waveforms, allowing the analysis of the different reception times simply by clicking the appropriate button.

2 The CARMELO receiver network

The main difference between professional and amateur meteor radar lies in whether or not they have a dedicated transmitter. Amateurs use other people's transmitters: with great power, with a frequency in the VHF (Very High Frequency) range and positioned at a large distance. Unfortunately, the analogue standard television broadcasting switch off in favor of the digital one and the

---

transmigration of emissions to UHF has deprived amateur observers of many usable transmitters.

This conversion occurred first in Europe and then in the USA. In fact, now in the European territory the best, if not only usable transmitter, is the Graves military transmitter, while in the USA the few digital terrestrial broadcasts that remained on the VHF have drastically reduced their power. For this reason, the CARMEL0 installed in the USA now has much lower numbers of reception compared to previous years. At the time of writing, the functioning CARMELO network has one receiver in the USA, a dozen receivers in Italy and one in Croatia.

3 The events page

The events page records all the meteors observed by the network in the last week. Each event is plotted with the recording time on the abscissa scale and with the maximum radioelectric power on the ordinate axis.

Each event is also characterized by a symbol and a color corresponding to the observer who recorded that event. The size of the sign is proportional to the duration of the recording. By positioning the mouse over each event, a box appears which summarizes the essential data of that recording; all of this is automatic.

4 The waveforms

By clicking on the event, it is possible to see the waveform and the frequency simultaneously. This is possible because the server plots the result obtained from the FFT calculation carried out on each single sampling carried out on the radio meteor echo.

The waveforms are of various types: from those more similar to pulses which are characteristic for underdense meteors to the longer and flatter one's characteristic of overdense meteors.

The durations vary from about fifty milliseconds to several seconds. The lower limit of the duration of the detection of underdense meteors is given by the length of the sampling: in CARMELO, to identify a meteor, at least two consecutive samplings are needed.

The duration of each single sampling depends on the performance of the microprocessors: and ranges from a minimum of 8 to a maximum of 20 milliseconds. We have noticed that apparently identical Raspberry Pi4s, paired with identical dongles while running the same program, do not have the same speed. Using the new Raspberry Pi5 the speed increases by approximately 25%.

Undersense meteors show the descending curve which is expected considering the diffusion of the ionized plasma cylinder through free ion-electron recombination.

Another possible interpretation concerns the functioning of the transmitter, which, as mentioned, is a military radar. We do not have precise information about it and therefore we cannot know if the transmitted power undergoes variations over time such as to justify this type of variations in the received signal, also because these variations, as mentioned, do not have a pattern that is regularly repeated.

The waveforms illustrated so far concern the echoes reception coming from the reflection point P along the plasma cylinder formed by the ionization and therefore by the creation of free electrons, see *Figure 3*.

At point P the fundamental conditions of reflection occur:

- At this point the incidence angle is equal to the reflection angle.
- P is also the tangent point between the straight line representing the meteor and the ellipse which has the transmitter and receiver as foci.
- Furthermore, the plane on which the *TPR* triangle lies is orthogonal to the meteor trajectory. (Cis Verbeeck, Jean-Louis Rault, 2022)
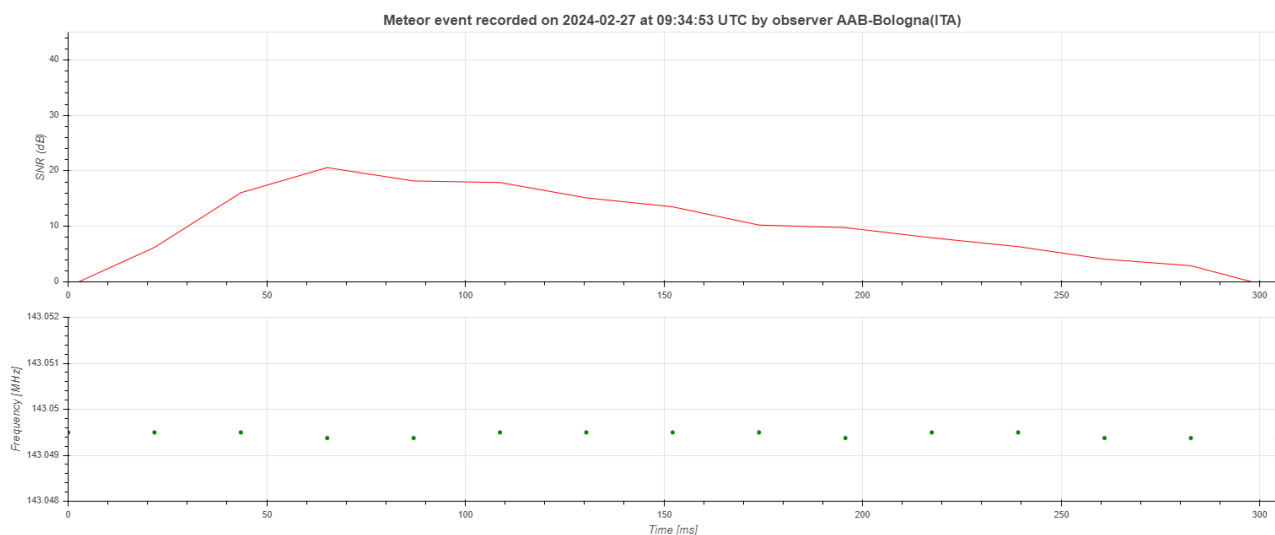
Figure 1 – Graph with waveform (above in red) and frequency (below in green).
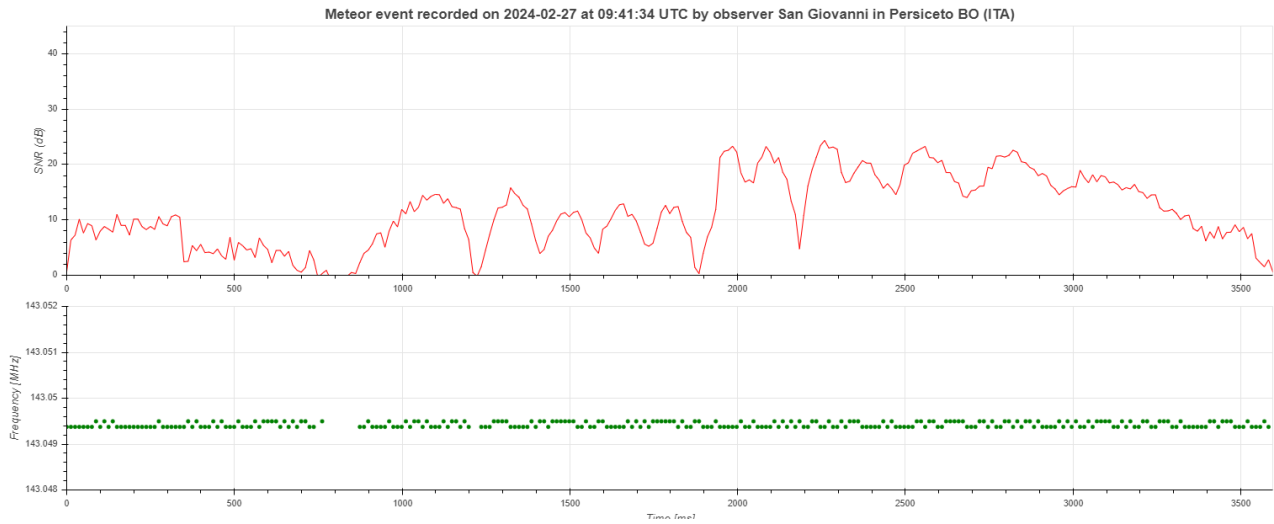
Figure 2 – Oscillations.
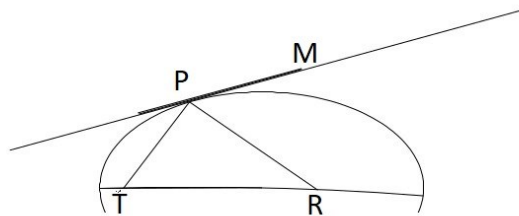
Figure 3 – The reflection condition: *T* is the transmitter, *R* the receiver, *P* the reflection point placed on the cylinder of ionized electrons.
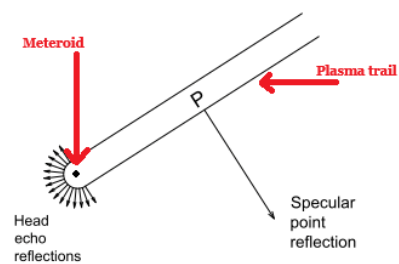
Figure 4 – Artistic representation of the two types of reflection.

5   The head echo

As mentioned, without the realization of the specular reflection condition, reception does not occur; it is possible, however, that before the creation of this cylinder, or even regardless of it, it is possible for a receiver to pick up the head echo.

The head echo is generated in the front part of the meteor radio where the meteoroid ablation generates the plasma first appearance which takes on a spheroidal shape.
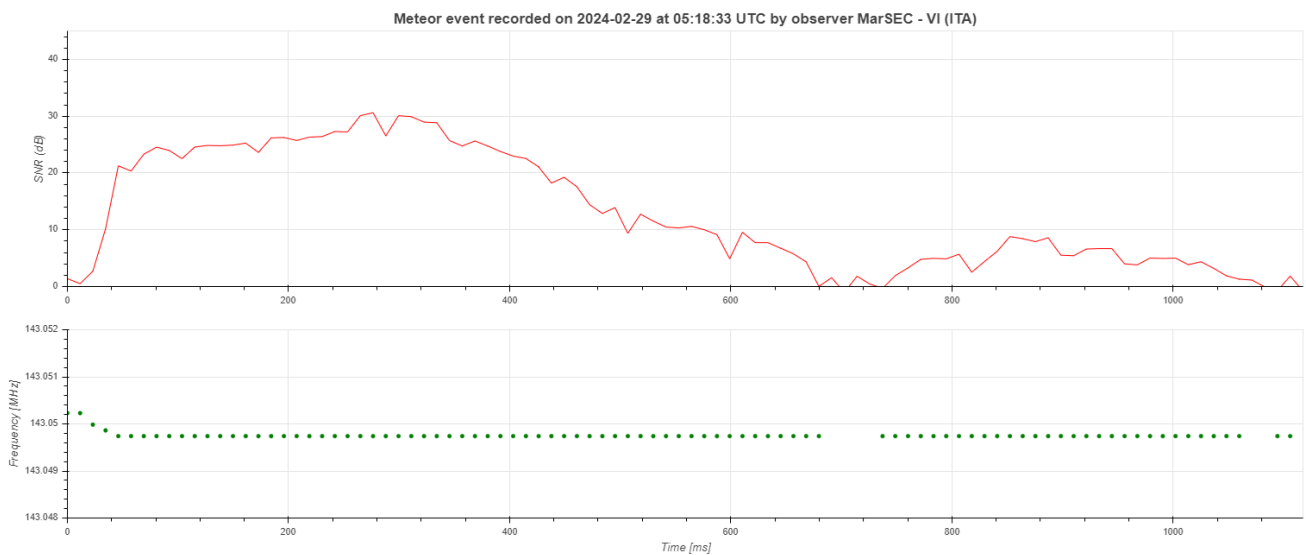
Figure 5 – The head echo. In the first 50 milliseconds the signal comes from the plasma sphere caused by the advancement of the meteor in the ionosphere. The received power (in red) is low and the frequency (in green) shows the Doppler shift. Around 50 milliseconds the meteoroid reached the reflection point *P*, orthogonal to the observer's point of view. The Doppler shift fades out and the reflection of the ionized cylinder overrides that of the receding head echo.
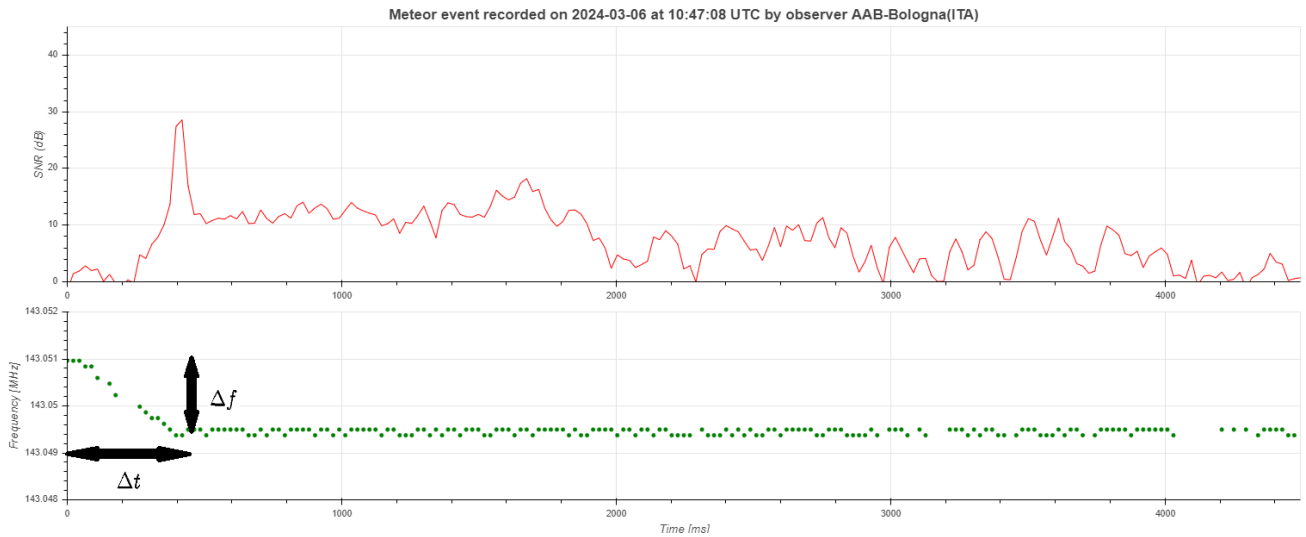
Figure 6 – Δf and Δt in the Doppler shift.
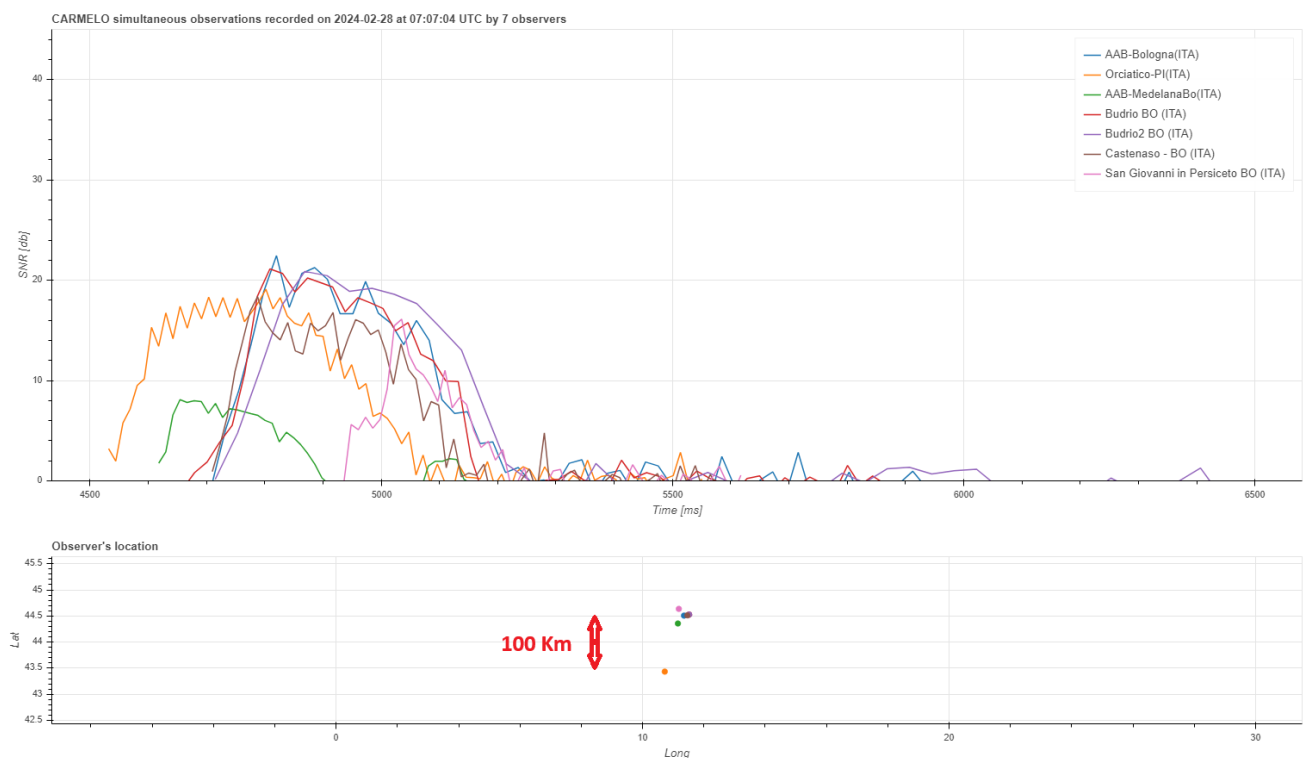
Figure 7 – Overlay of waveforms coming from 7 different receivers. In the upper part of the graph, you can see the different amplitudes of the radioelectric power received and the different reception times. In the lower part the location of the interested observatories on the territory is reproduced.

On this shape the reflection is omnidirectional and the reception is therefore admissible regardless of the reflection conditions typical of the specular reflection, described above.

In the case of the meteor in *Figure 5* we note that the first 50 milliseconds describe the head echo: the signal is very weak compared to that due to the cylinder of free electrons that is created after the first 50 milliseconds. Despite the small amount of power received, the Doppler shift due to the meteor speed is evident.

CARMELO records the frequency of each sampling with a precision of ± 61 Hz. The ratio between Δf and Δt gives us the Doppler shift slope. This slope depends on the meteor frequency and on the geometry determined by the mutual position of the meteor trail, the transmitter and the receiver.

6   Simultaneous receptions

The network of receivers in operation at the time of writing covers a small part of our country (Italy). The distances between the observatories vary between tens of kilometers and up to a few hundred kilometers.

Many meteor echoes are simultaneously observed by multiple observers: in this case the user can view all the superimposed waveforms by clicking on the "see simultaneous receptions" button. As you can see, simultaneous receptions of the same event are more likely with nearby receivers, but above all for higher power echoes, it happens that they can also be seen from relatively distant locations.

The waveforms have different amplitudes: this depends on various factors: first of all the antennas do not all have the same gain, and above all, not all observation conditions are optimal: some observatories have buildings or land close to the antenna, thus moving away from the conditions of best reception, but the essential fact that different observers receive the signal from different points of the trajectory must be taken into consideration, and it is therefore possible that the free electrons density in different trajectory points is, in fact, different. A point with lower ionization therefore involves less reflection and a faster process of recombination of ions and free electrons with consequent shorter duration of the echo.

The differences between the waveforms recorded by observers distant from each other cannot always be explained with the arguments presented above; there are cases in which different waveforms can be interpreted as different behaviors of the radio meteor at different points of its trajectory. The graph in *Figure 8* shows one of the cases we sometimes encounter.
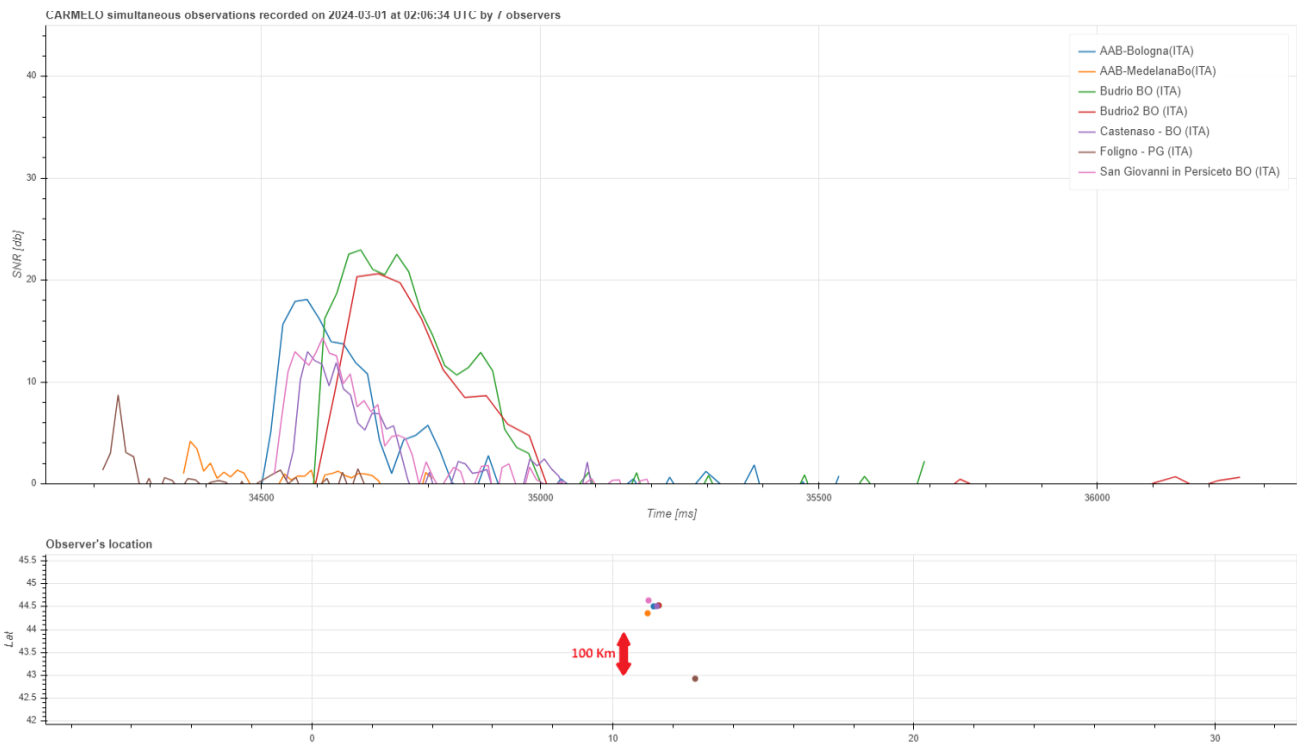
Figure 8 – After about a second and several tens of km travelled, the radio meteor shows a sudden increase in reflection.
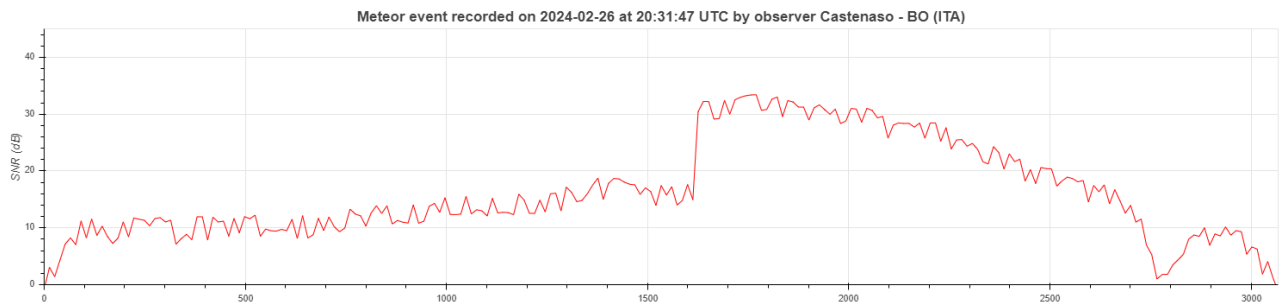
Figure 9 – Another case of sudden increase in power received.

The last observer recorded a sudden increase in received power. The explanation for this fact may have been traced back to a measurement error of the equipment, but this explanation is not supported by the experience we have acquired in three continuous years of CARMELO operation.

It could otherwise be hypothesized that the cause of this increase in power lies in the functioning of the transmitter, and in particular in the variation in power due to the rotation of the radiation beam of its antennas. Indeed, the Graves transmitter, being a military transmitter, has technical parameters that are not easily known and the little information in our possession is scarce and dated.

The impression we have after many years of observation is that something has changed in the time and that the discontinuities in the sky sweep carried out by Graves' antennas have, if not disappeared, drastically decreased. Furthermore, the fact that the increase in reception of this radio meteor is around ten dB, and thus vertical, and above all detected by a single observer, would rule out this hypothesis.

As an alternative to the explanations set out above, one could hypothesize that at the instant of the increase in the received power CARMELO "saw" a fragmentation of the meteoroid and a consequent increase in the production of ionized plasma. Although uncommon, the observation of sudden increases in received power also occurs in other cases.

The most interesting observation concerns the temporal sequence of the rising edges present in the recorded waveforms by each observer.
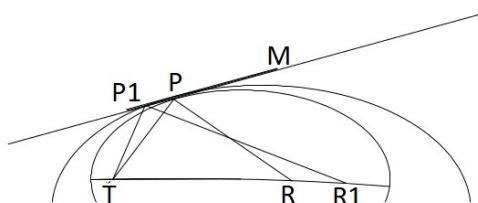
Figure 10 – Different receivers see the same meteor at different points on its trajectory.

If we hypothesize that the instant in which the reception presents its initial rising edge is the one in which the radio meteor appears at the specular reception points $P_1, P_2,… .P_n$ we can associate the different times $t_1, t_2,….t_n$ to these transits.

By comparing the various times of increasing waveforms it is possible to see the progression in space of the different moments in which the cylinder of free electrons appears for each observer.

In simultaneous receptions the delay times follow a sequence which has a clear counterpart in the location on the territory: for example, in *Figure 11* we can see how the temporal progression suggests a trajectory from south west to north east. In some cases, there are simultaneous receptions even between very distant receivers.

7   Velocity calculation

The images displayed here are a small sample of the amount of data that the CARMELO network provides and makes available to observers and enthusiasts, continuously and in real time for each observed meteor.

Are the data provided by the observations of the CARMELO network sufficient to calculate the speed of the meteors? This objective has so far been a forbidden dream for all amateur astronomers, that is, for all those who observe radio meteors using continuous wave transmitters.

The absence of a pulsed signal in fact prevents any sort of triangulation and measurement on the different times of the progressing meteor trajectory of the individual echoes received by multiple receivers. We can consider two different approaches: that of the head echoes Doppler shifts and that of the simultaneous observed time delays.

Figure 11 – Simultaneous reception from three observers: the waveforms are similar.
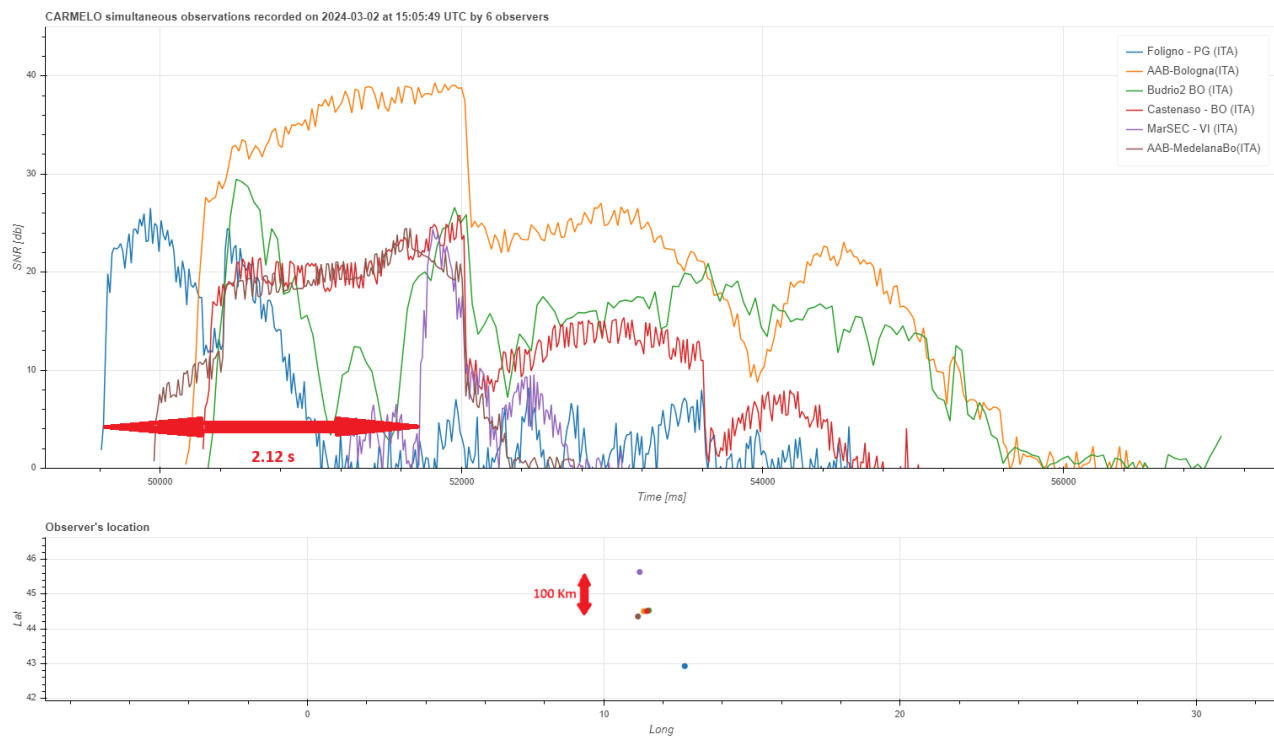
Figure 12 – Simultaneous reception performed by 6 observers. The two most distant are over 300 km away. The delay between the two rising edges is 2.12 seconds.

In the first case the absence of information about the meteor trail position in the forward scatter configuration prevent us from writing an algorithm suitable for solving the problem. As already said in *Section 5* head echoes are not always present in receptions and this is due to at least two factors: first of all, the fact that they are very weak and therefore almost always indistinguishable from noise, secondly because due to the geometric orientation of the track the head echo may not always appear before the meteor transit point P of the specular reflection.

The CARMELO network data provide us with the delay times of the wave fronts appearance at the specular reception points P_1, P_2,…,P_n observed along the meteor's path. The question arises whether it is possible to write a set of equations that is able to place the aforementioned points along the tangent line to the n ellipsoids having as foci T and the points R_1, R_2,…,R_n represented in *Figure 10*. In this way it would be possible to outline both the trajectory and the speed.

To this end it is possible to search for the points P_1, P_2,…,P_n and their coordinates using the method described by M. T. German (2023) by calculating the shortest distance in the path T P_n R_n between the infinite points of the meteor's trajectory. Here too, comparison with the video recordings of the aforementioned networks will be necessary.

8   Conclusions

The observation of the hourly rate of meteoric activity has so far been the only result of the experiences of receiving radio meteors with the meteorscatter method in the amateur field. The CARMELO project allows us to go beyond this objective.

With CARMELO it is possible to see in real time the waveform of each observed radio meteor and qualitatively analyze the physics of each event: from the head echo to the creation of the reflecting plasma cylinder up to its dissolution.

On a quantitative level, the data produced allow us to investigate the Doppler shift created in the head echo and to evaluate the speed of the meteor as a function of the meteor-receiver distance.

The simultaneous reception of the same event by multiple observers located across the territory allows us to obtain the different times in which the radio meteor reaches the specular reflection point for each of the observers. The development of a geometric analysis of the temporal sequence can lead to the velocity measurement and the evaluation of the trajectory.

The next step will be to choose one or more events that have a simultaneous visual observation recorded in one of the various networks based on dedicated video cameras, and from these data compare position, speed and trajectory in search of resemblances both in the field of head echo Doppler shift measurement, and in the temporal sequence of simultaneous receptions.

Acknowledgment

References

Barbieri L. and Brando G. (2022). "A global network for radio meteor observers". *eMetN Meteor Journal*, **7**, 34–45.

Barbieri L., Brando G., Fontana P., and Sarto S. (2023). "First steps of the CARMELO network (Cheap Amateur Radio Meteors Echoes LOgger)". *eMetN Meteor Journal*, **8**, 201–206.

German M.T. (2023). "Utilizing Video Meteor Trails to Understand Radio Meteor Detection". *WGN, Journal of the International Meteor Organization*, **51**, 72–92.

Verbeeck C., Rault J.-L. (2022). Radio meteor observations. Handbook for meteor observers. Jürgen Rendtel, editor, International Meteor Organization.

Radio meteors April 2024

Felix Verbelen

Vereniging voor Sterrenkunde & Volkssterrenwacht MIRA, Grimbergen, Belgium
`felix.verbelen@gmail.com`

An overview of the radio observations during April 2024 is given.

1   Introduction

The graphs show both the daily totals (*Figure 1 and 2*) and the hourly numbers (*Figure 3 and 4*) of "all" reflections counted automatically, and of manually counted "overdense" reflections, overdense reflections longer than 10 seconds and longer than 1 minute, as observed here at Kampenhout (BE) on the frequency of our VVS-beacon (49.99 MHz) during the month of April 2024.

The hourly numbers, for echoes shorter than 1 minute, are weighted averages derived from:

$$N(h) = \frac{n(h-1)}{4} + \frac{n(h)}{2} + \frac{n(h+1)}{4}$$

Local interference and unidentified noise remained low for most of the month, but weak to moderate lightning activity was observed on 4 days, while strong lighting above our beacon on April 8th made meteor observations very difficult for some time (*Figure 5*).

Also, solar activity was particularly strong during this month. Attached (*Figures 6 and 7*) are examples of the registrations of a number of strong type III outbursts on 12 and on 19 April.

Meteor activity gradually increased in the course of the month, but the eye-catcher came as expected on April 22nd with the Lyrids. Counts of "all" reflections hardly shows an increase at that date, but the increased number of overdense meteors is striking.

During the entire month 6 reflections longer than 1 minute were recorded. A selection of these, along with some other interesting reflections is included (*Figures 8 to 14*). More of these are available on request.

In addition to the usual graphs, you will also find the raw counts in cvs-format[9] from which the graphs are derived. The table contains the following columns: day of the month, hour of the day, day + decimals, solar longitude (epoch J2000), counts of "all" reflections, overdense reflections, reflections longer than 10 seconds and reflections longer than 1 minute, the numbers being the observed reflections of the past hour.

---

[9] https://www.emeteornews.net/wp-content/uploads/2024/05/202404_49990_FV_rawcounts.csv

49.99MHz - RadioMeteors April 2024
daily totals of "all" reflections *(automatic count_Mettel5_7Hz)*
Felix Verbelen (Kampenhout)
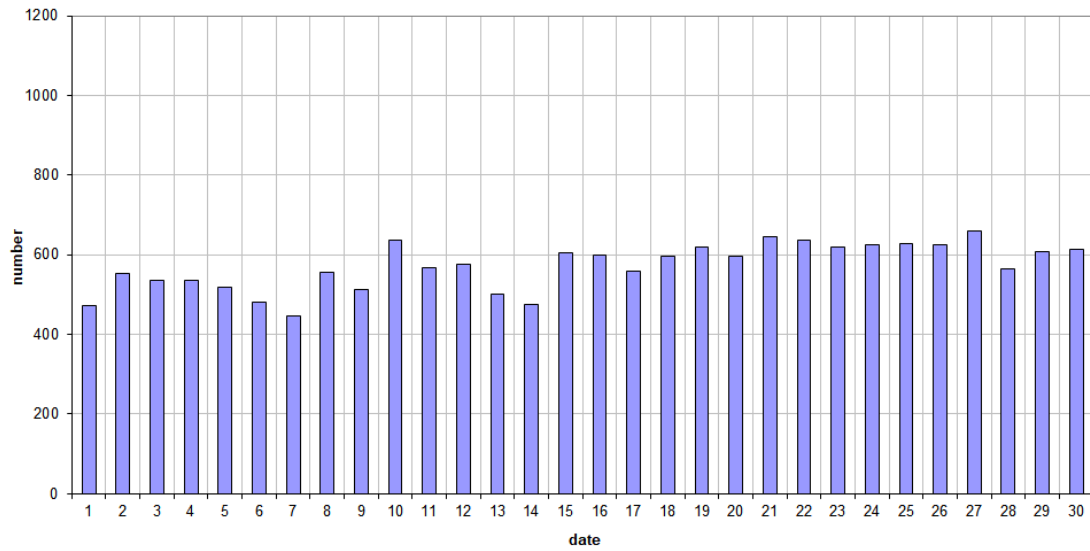
49.99MHz - RadioMeteors April 2024
daily totals of all overdense reflections
Felix Verbelen (Kampenhout)

Figure 1 – The daily totals of "all" reflections counted automatically, and of manually counted "overdense" reflections, as observed here at Kampenhout (BE) on the frequency of our VVS-beacon (49.99 MHz) during April 2024.

49.99MHz - RadioMeteors April 2024
daily totals of reflections longer than 10 seconds
Felix Verbelen (Kampenhout)

49.99MHz - RadioMeteors April 2024
daily totals of reflections longer than 1 minute
Felix Verbelen (Kampenhout)

Figure 2 – The daily totals of overdense reflections longer than 10 seconds and longer than 1 minute, as observed here at Kampenhout (BE) on the frequency of our VVS-beacon (49.99 MHz) during April 2024.

49.99 MHz - RadioMeteors April 2024
number of "all" reflections per hour (weighted average) *(automatic count_Mettel5_7Hz)*
Felix Verbelen (Kampenhout)

49.99MHz - RadioMeteors April 2024
number of overdense reflections per hour (weighted average)
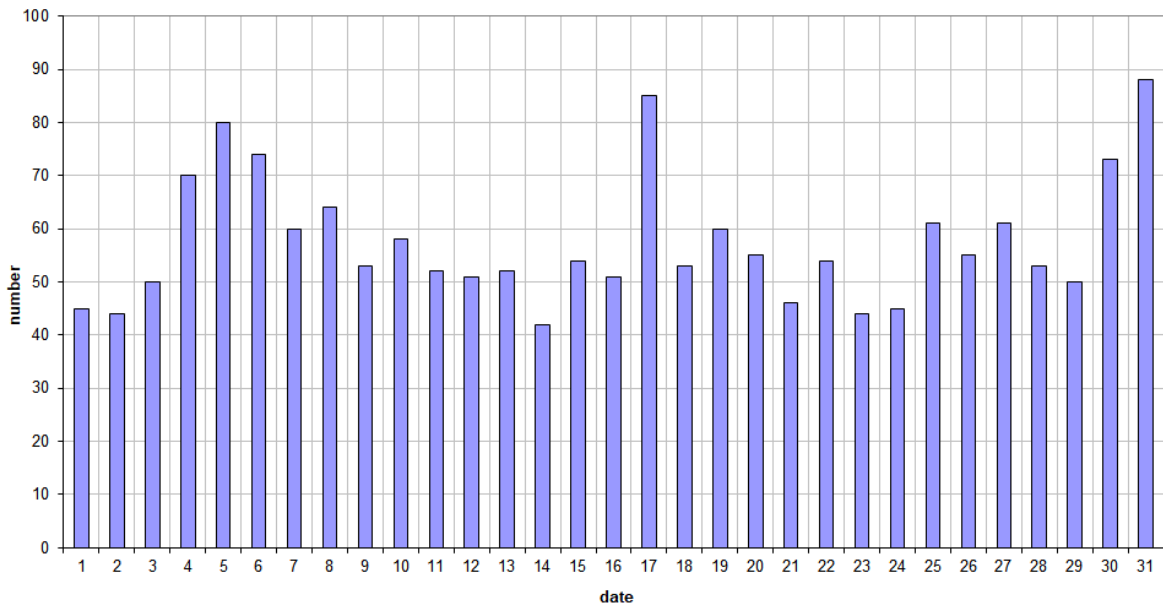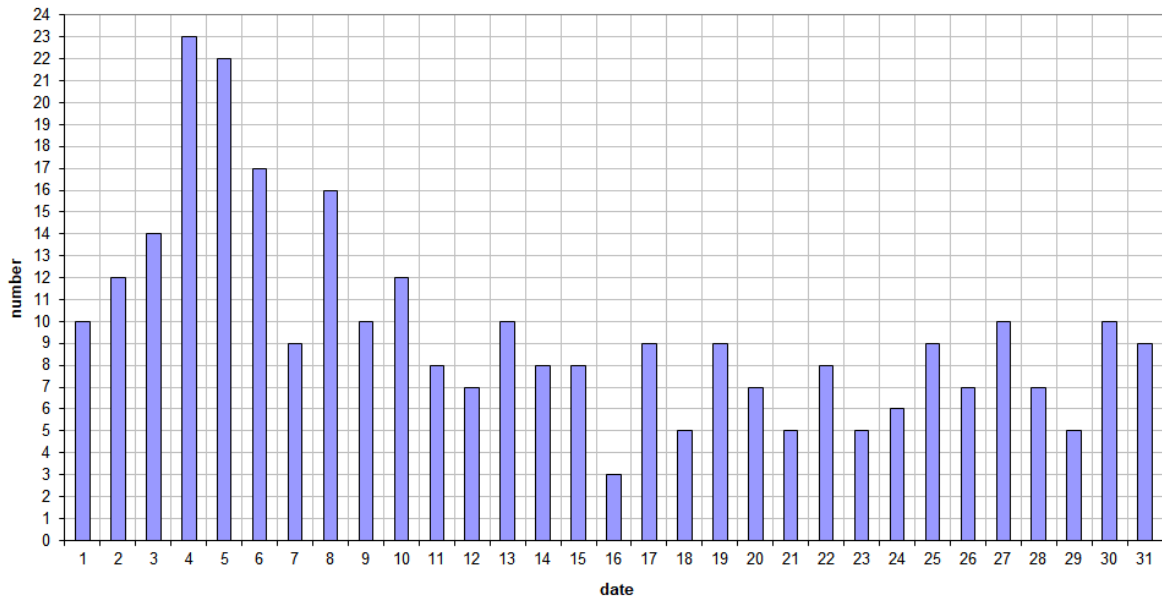*Felix Verbelen (Kampenhout)*

Figure 3 – The hourly numbers of "all" reflections counted automatically, and of manually counted "overdense" reflections, as observed here at Kampenhout (BE) on the frequency of our VVS-beacon (49.99 MHz) during April 2024.

49.99MHz - RadioMeteors April 2024
number of reflections >10 seconds per hour (weighted average)
Felix Verbelen (Kampenhout)
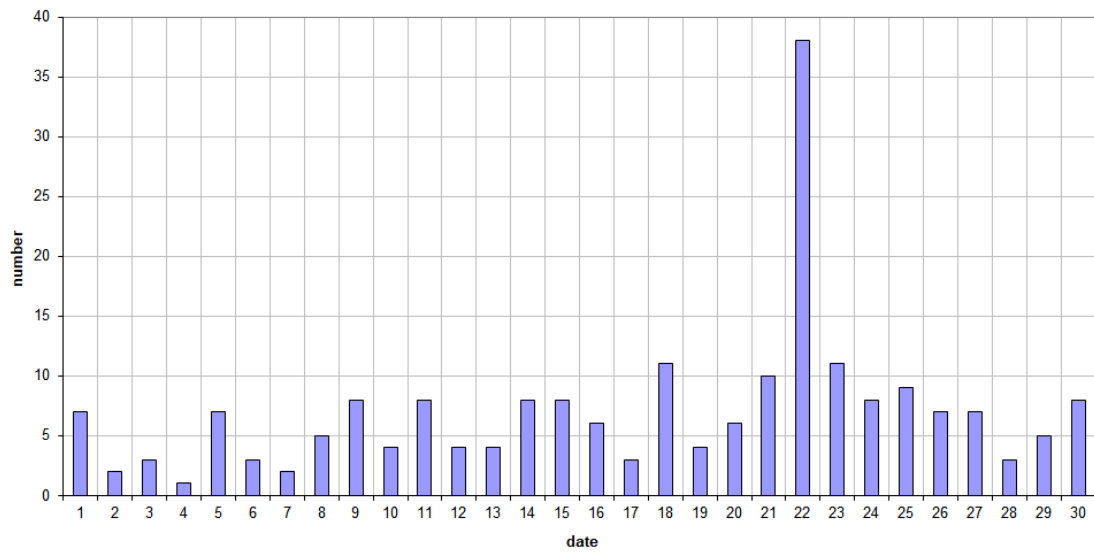
49.99MHz - RadioMeteors April 2024
hourly totals of overdense reflections longer than 1 minute
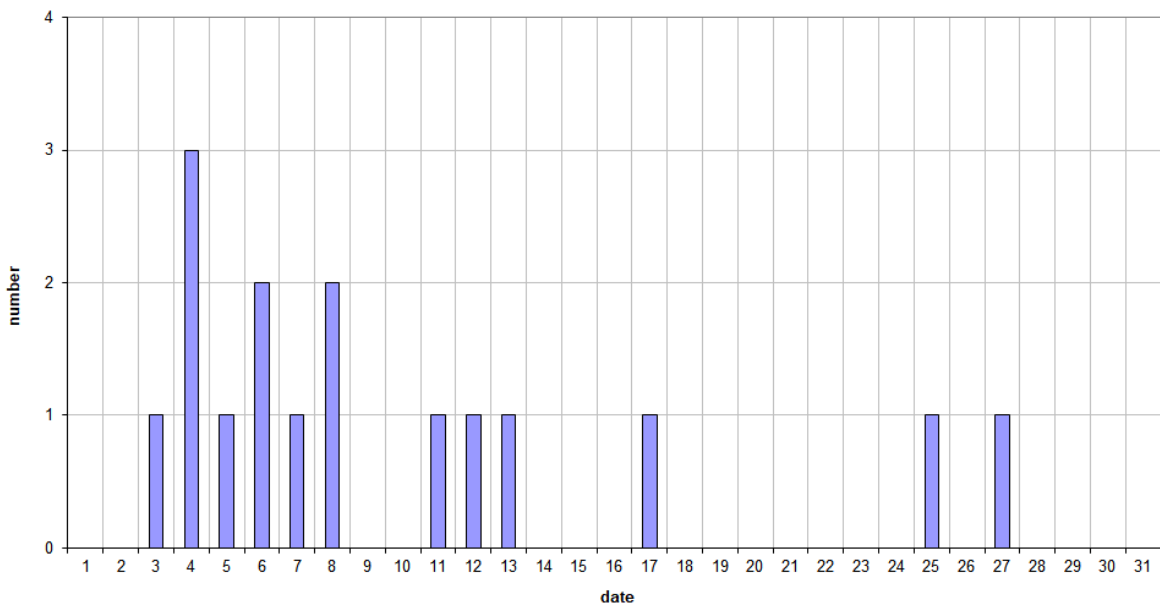*Felix Verbelen (Kampenhout/BE)*

Figure 4 – The hourly numbers of overdense reflections longer than 10 seconds and longer than 1 minute, as observed here at Kampenhout (BE) on the frequency of our VVS-beacon (49.99 MHz) during April 2024.

Figure 6 – Strong type III outbursts on 12 April.
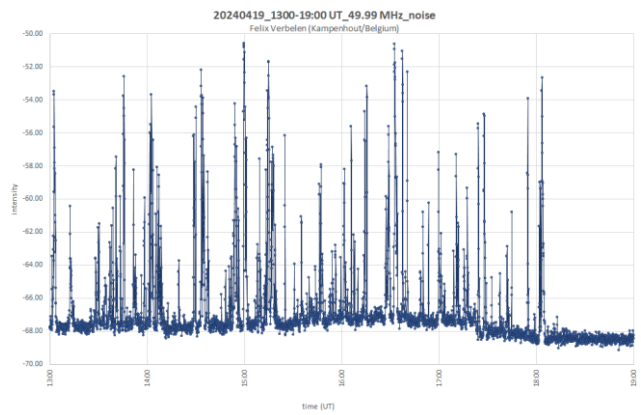
Figure 7 – Strong type III outbursts on 19 April.

Figure 5 – Strong lighting above our beacon on April 8th made meteor observations very difficult for some time.
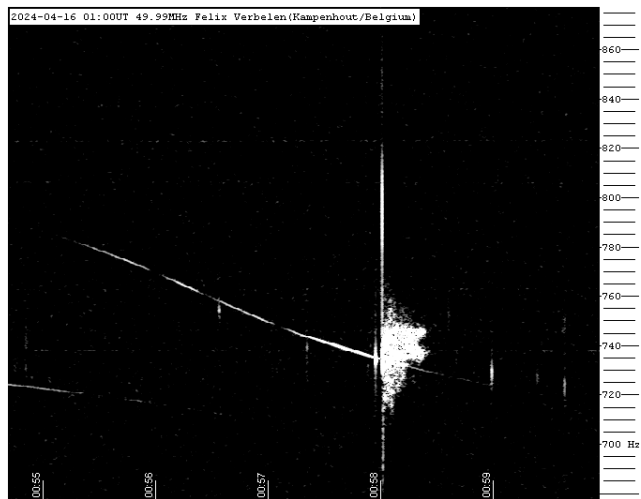
Figure 8 – Meteor echoes April 16, 01h00m UT.
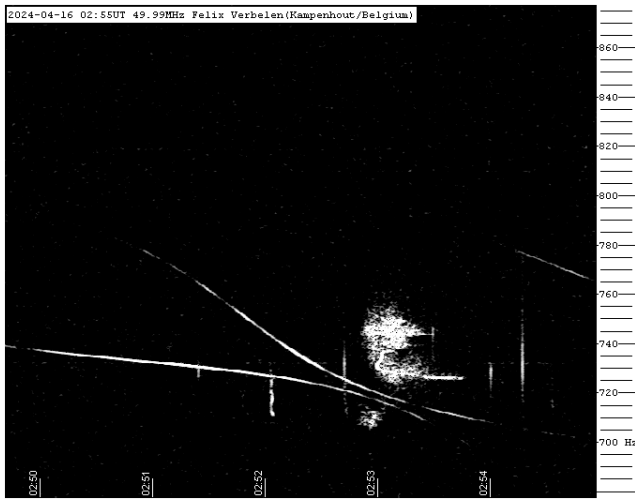
Figure 9 – Meteor echoes April 16, 02ʰ55ᵐ UT.
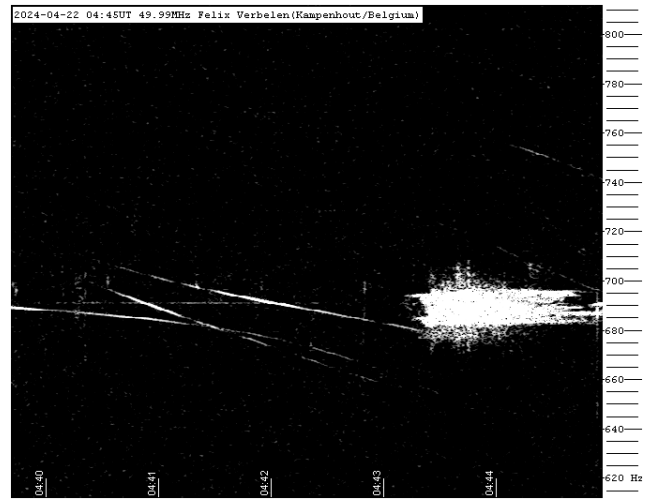
Figure 12 – Meteor echoes April 22, 04ʰ45ᵐ UT.
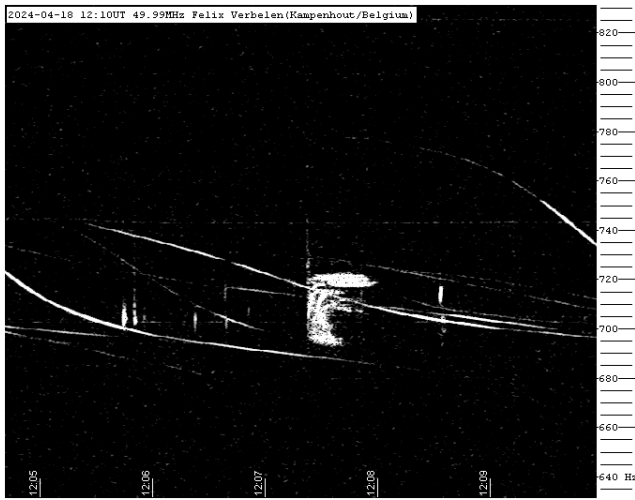
Figure 10 – Meteor echoes April 18, 12ʰ10ᵐ UT.
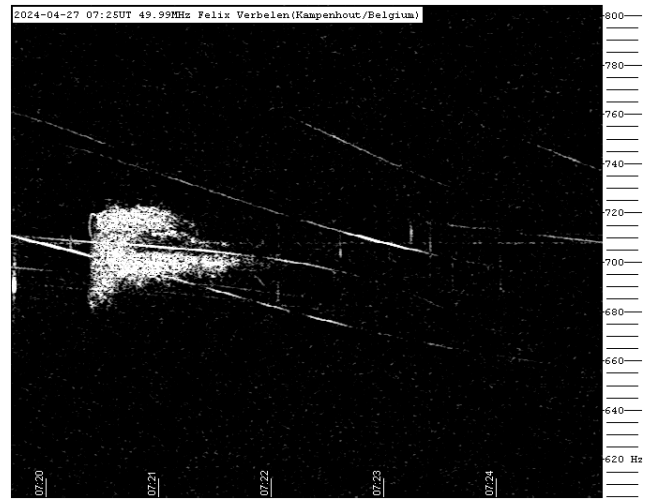
Figure 13 – Meteor echoes April 27, 07ʰ25ᵐ UT.
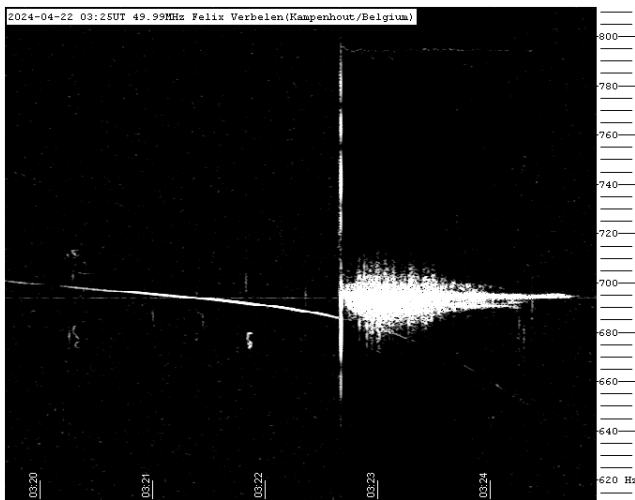
Figure 11 – Meteor echoes April 22, 03ʰ25ᵐ UT.

Figure 14 – Meteor echoes April 29, 05ʰ55ᵐ UT.

Radio meteors May 2024

Felix Verbelen

Vereniging voor Sterrenkunde & Volkssterrenwacht MIRA, Grimbergen, Belgium
felix.verbelen@gmail.com

An overview of the radio observations during May 2024 is given.

1   Introduction

The graphs show both the daily totals (*Figure 1 and 2*) and the hourly numbers (*Figure 3 and 4*) of "all" reflections counted automatically, and of manually counted "overdense" reflections, overdense reflections longer than 10 seconds and longer than 1 minute, as observed here at Kampenhout (BE) on the frequency of our VVS-beacon (49.99 MHz) during the month of May 2024.

The hourly numbers, for echoes shorter than 1 minute, are weighted averages derived from:

$$N(h) = \frac{n(h-1)}{4} + \frac{n(h)}{2} + \frac{n(h+1)}{4}$$

The past month has been anything but boring. Local interference and unidentified noise remained quite low for most of the month, but lightning activity was detected on 12 different days. Sometimes it was intense and lasting for hours, as on May 1, 12, 18, 19, and 26, significantly hindering meteor counting.

Also, the Sun was very active, with powerful outbursts almost daily, usually of type III, which sometimes hampered meteor recordings for several minutes (*Figures 5 to 7*).

On May 10 and 11 exceptionally powerful auroras were also visible from Belgium, the most intense being recorded on the frequency of our beacon (*Figures 8 to 10*).

During the second half of the month there were temporary problems with the transmission power of our beacon, but these apparently only had a minor impact on the observations.

The meteor activity was also particularly interesting. As expected, the eye-catchers were the eta-Aquariids that reached their maximum on May 4–6. Apparently, the long-lasting reflections (and therefore more massive meteoroids) came earlier than the shorter ones.

The last days of the month were notable for the suddenly increasing number of underdenses and short overdenses.

During the entire month 16 reflections longer than 1 minute were recorded. A selection of these, along with some other interesting reflections is included (*Figures 11 to 30*). More of these are available on request.

In addition to the usual graphs, you will also find the raw counts in cvs-format[10] from which the graphs are derived. The table contains the following columns: day of the month, hour of the day, day + decimals, solar longitude (epoch J2000), counts of "all" reflections, overdense reflections, reflections longer than 10 seconds and reflections longer than 1 minute, the numbers being the observed reflections of the past hour.

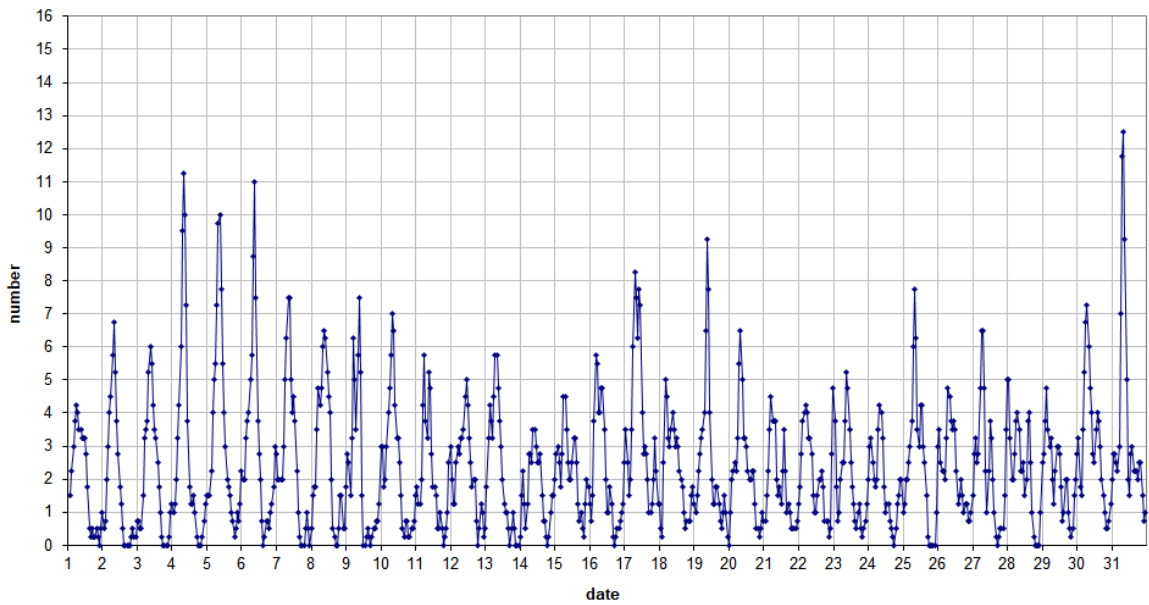[10] https://www.emeteornews.net/wp-content/uploads/2024/06/202405_49990_FV_rawcounts.csv

Figure 1 – The daily totals of "all" reflections counted automatically, and of manually counted "overdense" reflections, as observed here at Kampenhout (BE) on the frequency of our VVS-beacon (49.99 MHz) during May 2024.
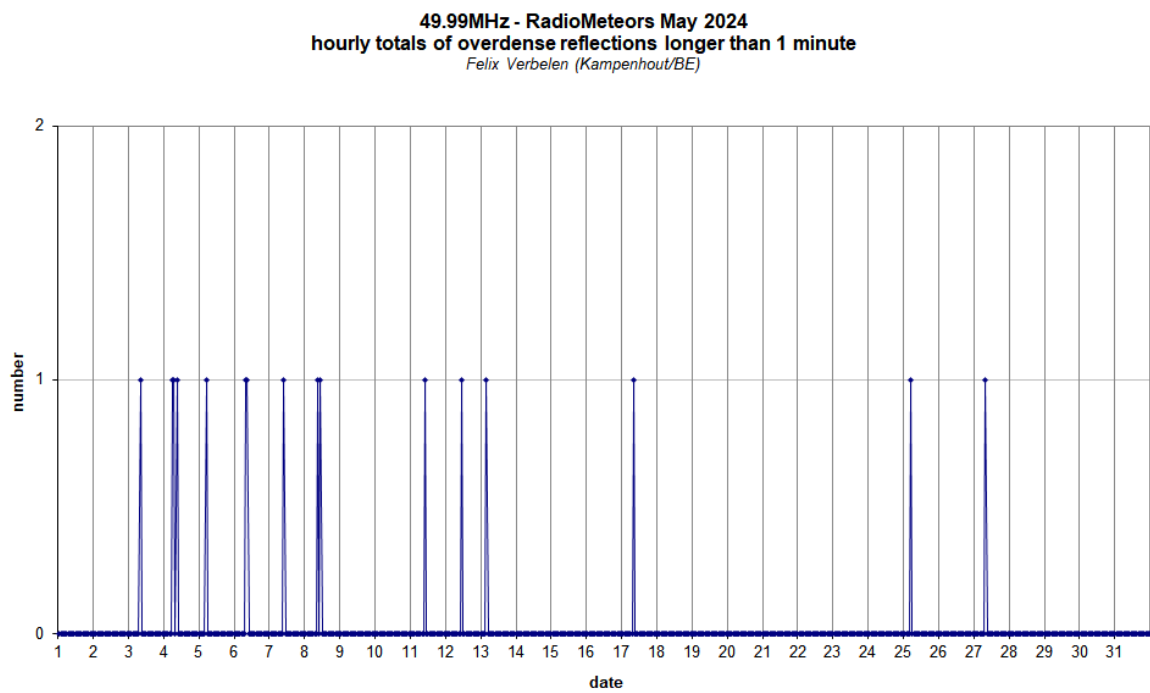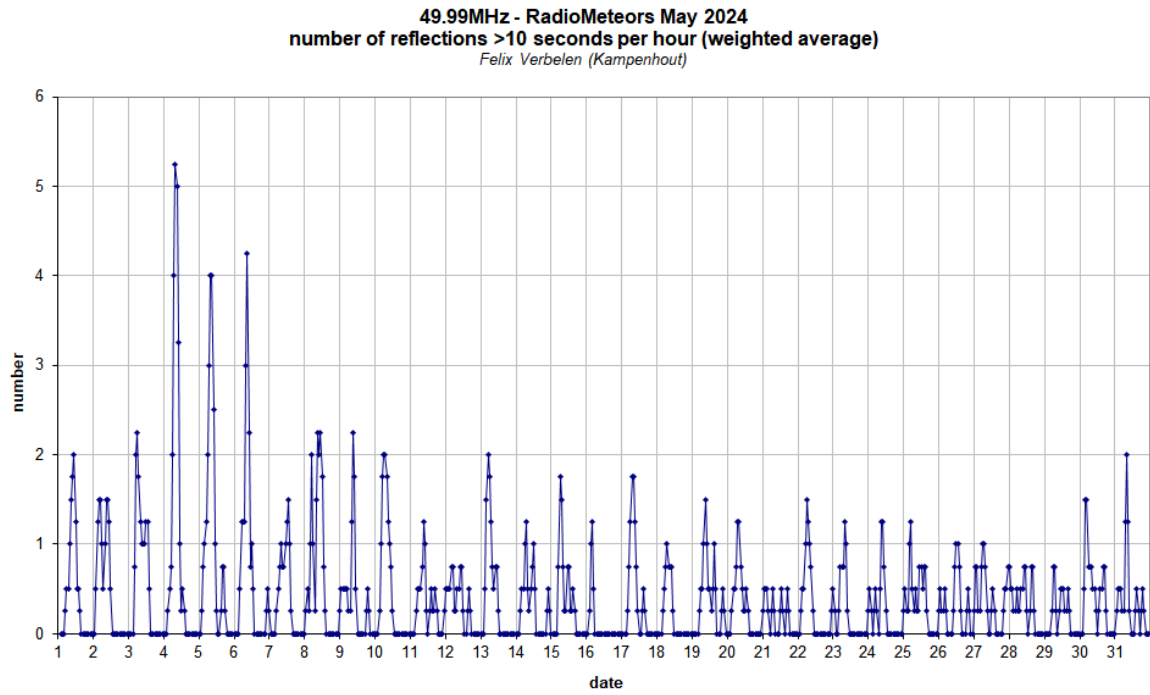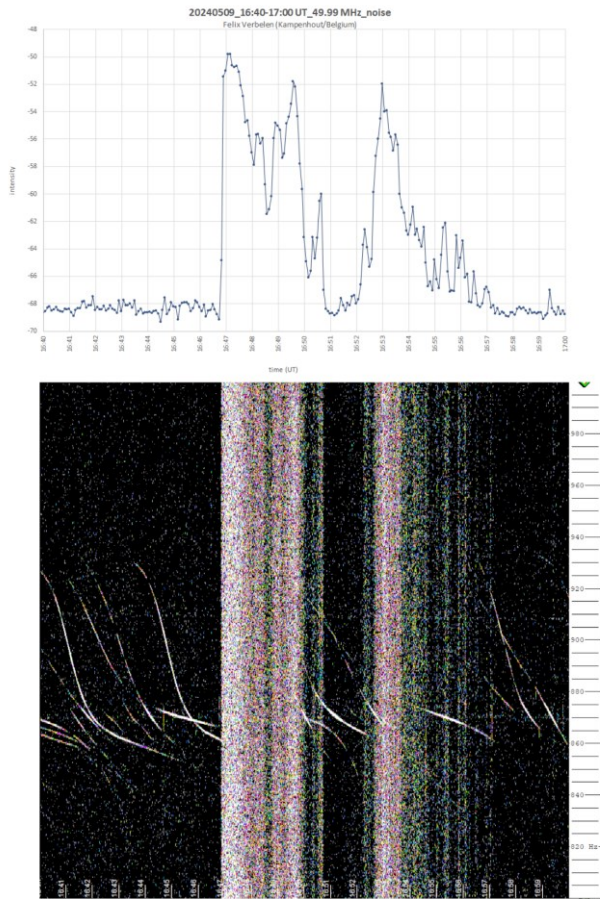
49.99MHz - RadioMeteors May 2024
daily totals of reflections longer than 10 seconds
Felix Verbelen (Kampenhout)

49.99MHz - RadioMeteors May 2024
daily totals of reflections longer than 1 minute
Felix Verbelen (Kampenhout)

Figure 2 – The daily totals of overdense reflections longer than 10 seconds and longer than 1 minute, as observed here at Kampenhout (BE) on the frequency of our VVS-beacon (49.99 MHz) during May 2024.

49.99 MHz - RadioMeteors May 2024
number of "all" refections per hour (weighted average) *(automatic count_Mettel5_7Hz)*
Felix Verbelen (Kampenhout)

49.99MHz - RadioMeteors May 2024
number of overdense reflections per hour (weighted average)
Felix Verbelen (Kampenhout)

Figure 3 – The hourly numbers of "all" reflections counted automatically, and of manually counted "overdense" reflections, as observed here at Kampenhout (BE) on the frequency of our VVS-beacon (49.99 MHz) during May 2024.

49.99MHz - RadioMeteors May 2024
number of reflections >10 seconds per hour (weighted average)
Felix Verbelen (Kampenhout)

49.99MHz - RadioMeteors May 2024
hourly totals of overdense reflections longer than 1 minute
Felix Verbelen (Kampenhout/BE)

Figure 4 – The hourly numbers of overdense reflections longer than 10 seconds and longer than 1 minute, as observed here at Kampenhout (BE) on the frequency of our VVS-beacon (49.99 MHz) during May 2024.

Figure 5 – Outbursts of the Sun hampered meteor observing for several minutes. 9 May 16ʰ40ᵐ – 17ʰ00ᵐ UT.
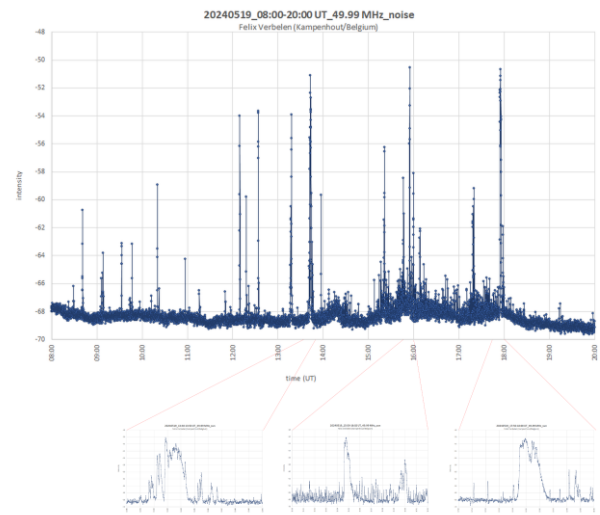
Figure 6 – Outbursts of the Sun hampered meteor observing for several minutes. 19 May 8ʰ00ᵐ – 20ʰ00ᵐ UT.
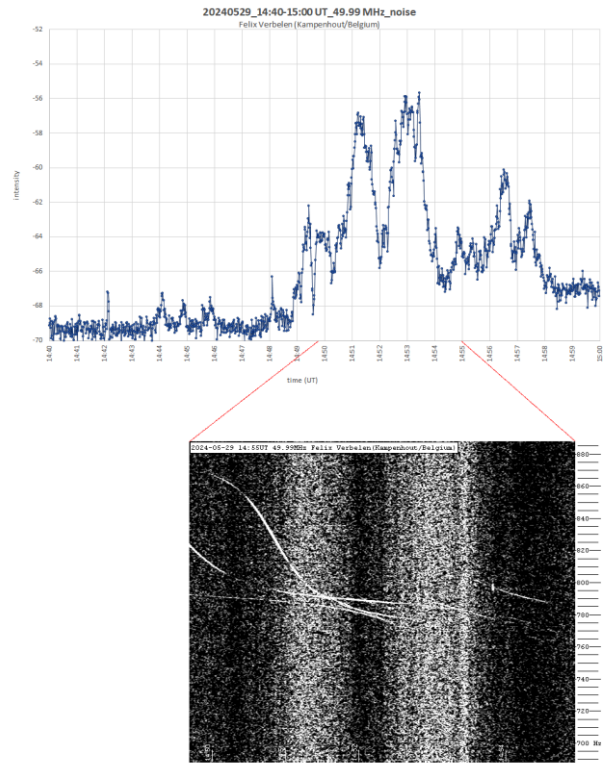
Figure 7 – Outbursts of the Sun hampered meteor observing for several minutes. 29 May 14ʰ40ᵐ – 15ʰ00ᵐ UT.
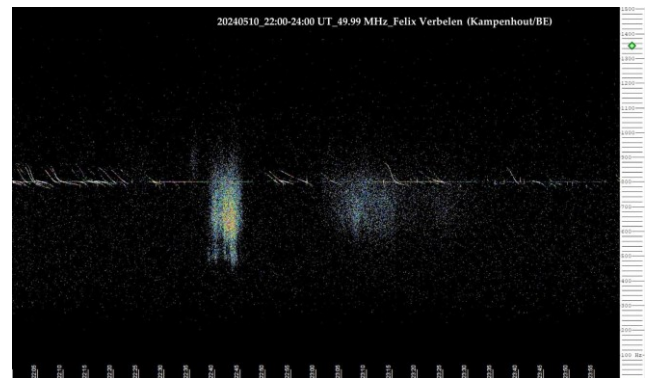
Figure 8 – On May 10 and 11 exceptionally powerful auroras were also visible from Belgium. 10 May 22ʰ00ᵐ – 24ʰ00ᵐ UT.
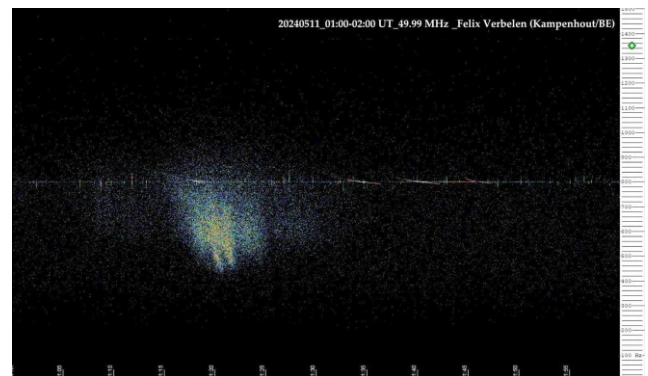
Figure 9 – On May 10 and 11 exceptionally powerful auroras were also visible from Belgium. 11 May 01ʰ00ᵐ – 02ʰ00ᵐ UT.
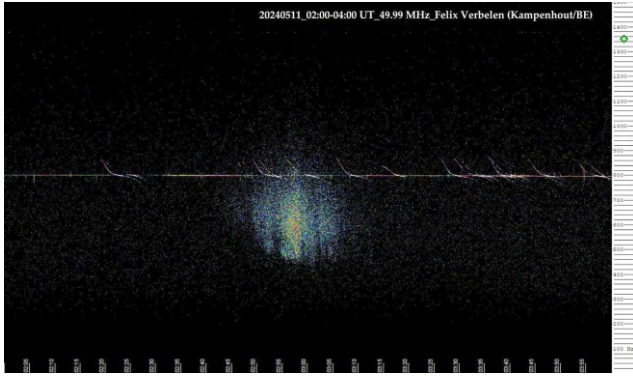
Figure 10 – On May 10 and 11 exceptionally powerful auroras were also visible from Belgium. 11 May 02^{h}00^m – 04^{h}00^m UT.

Figure 11 – Meteor echoes May 03, 06^{h}35^m UT.

Figure 12 – Meteor echoes May 03, 07^{h}45^m UT.
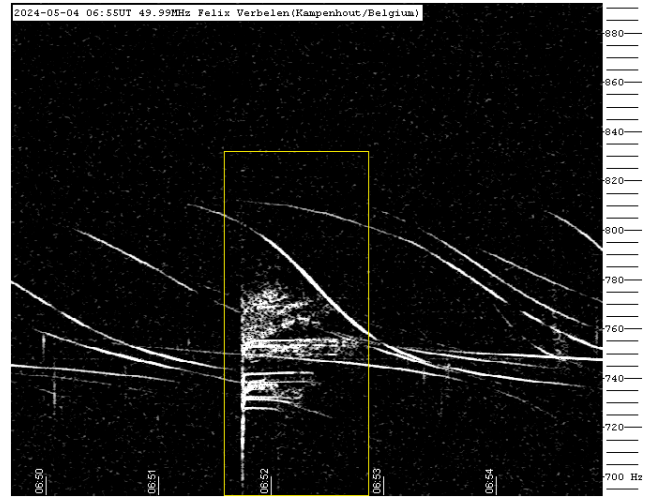
Figure 13 – Meteor echoes May 04, 06^{h}55^m UT.
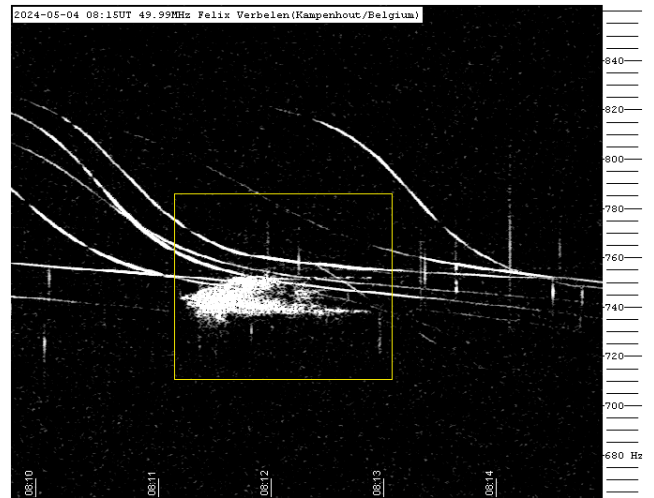
Figure 14 – Meteor echoes May 04, 08^{h}15^m UT.
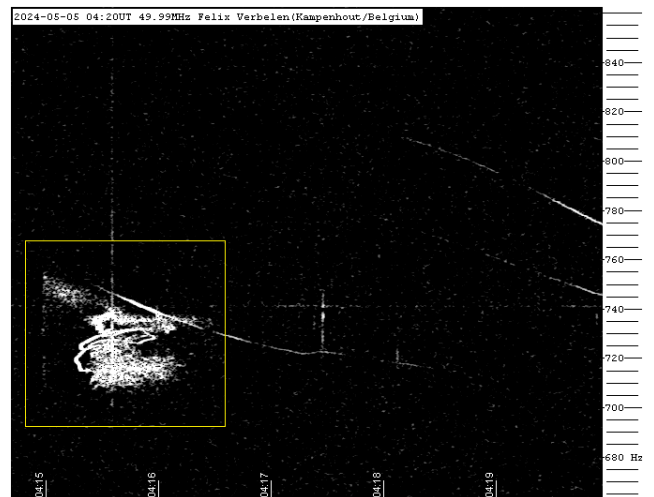
Figure 15 – Meteor echoes May 05, 04^{h}20^m UT.
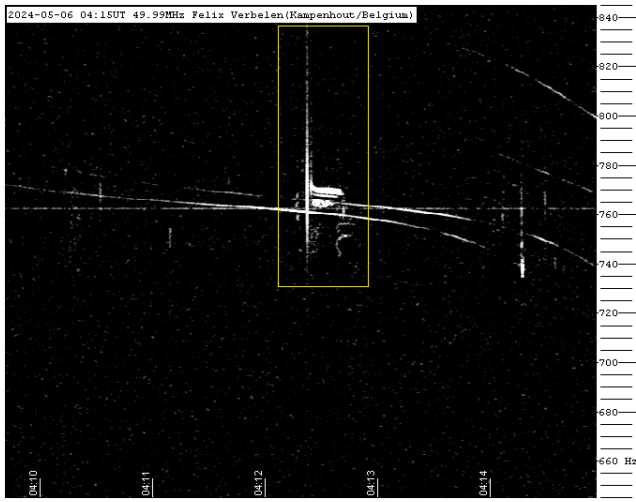
Figure 16 – Meteor echoes May 06, 04ʰ15ᵐ UT.
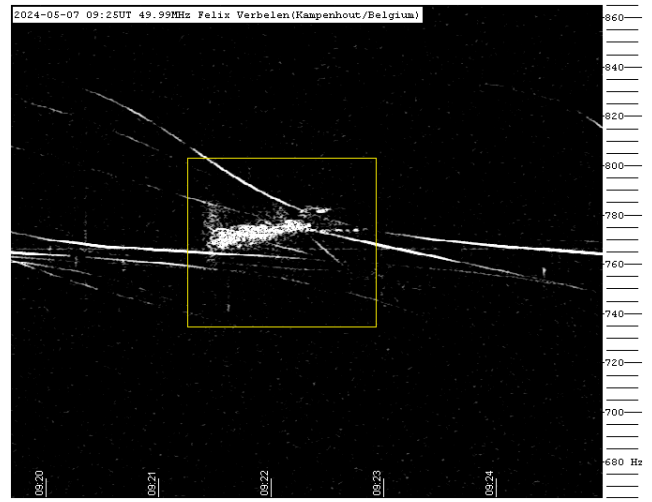
Figure 19 – Meteor echoes May 07, 09ʰ25ᵐ UT.
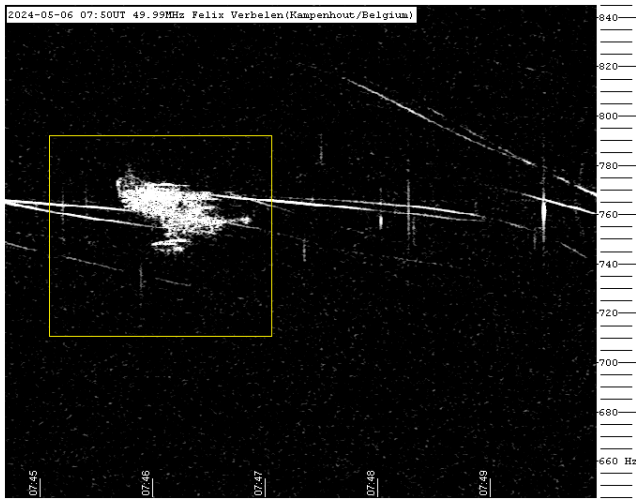
Figure 17 – Meteor echoes May 06, 07ʰ50ᵐ UT.
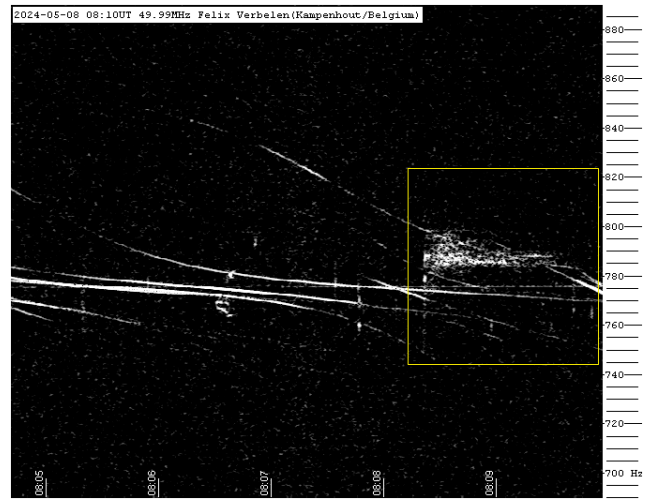
Figure 20 – Meteor echoes May 08, 08ʰ10ᵐ UT.
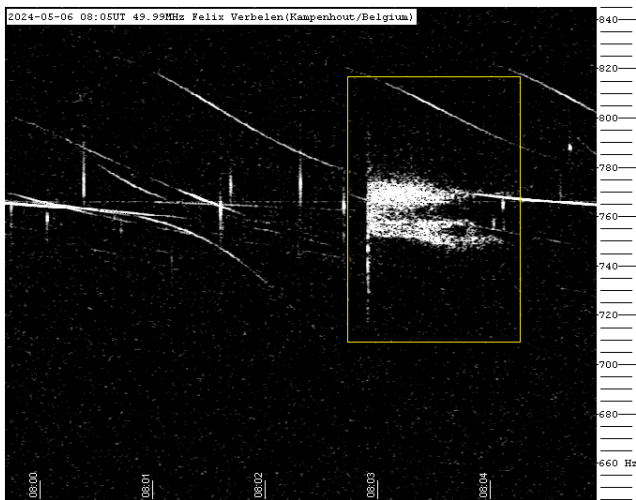
Figure 18 – Meteor echoes May 06, 08ʰ05ᵐ UT.
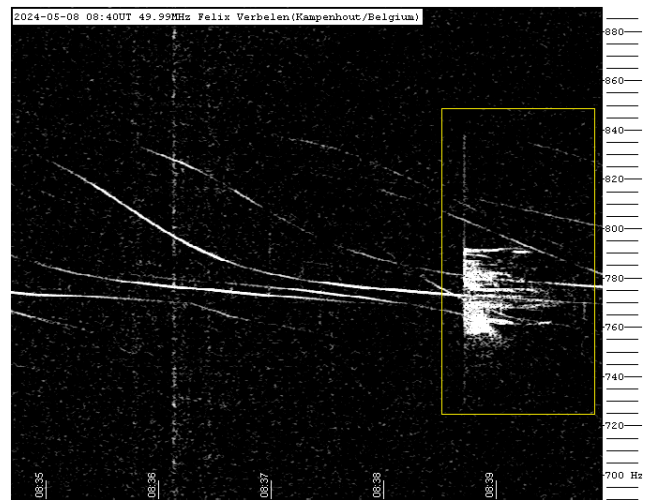
Figure 21 – Meteor echoes May 08, 08ʰ40ᵐ UT.
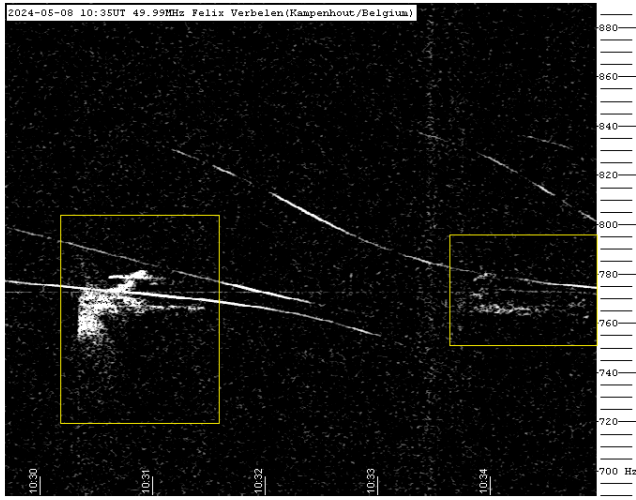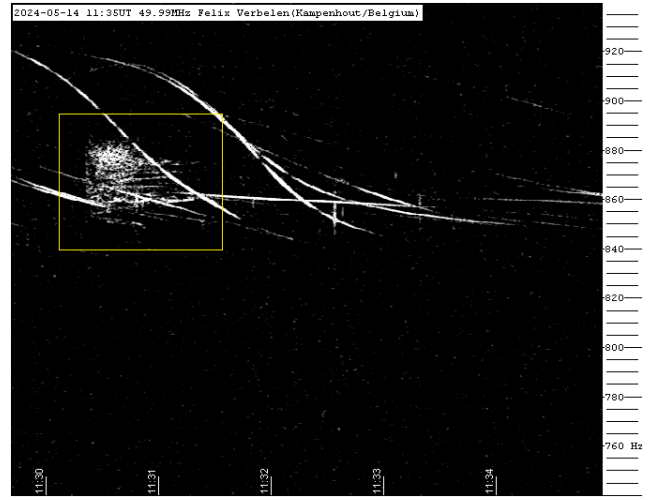
Figure 22 – Meteor echoes May 08, 10ʰ35ᵐ UT.
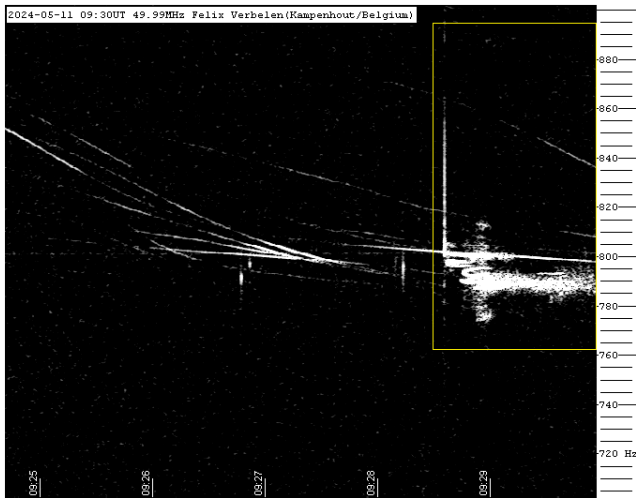

Figure 25 – Meteor echoes May 14, 11ʰ35ᵐ UT.
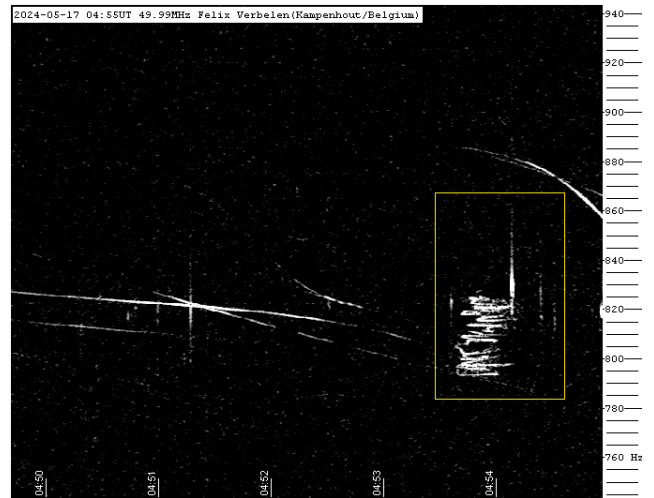

Figure 23 – Meteor echoes May 11, 09ʰ30ᵐ UT.

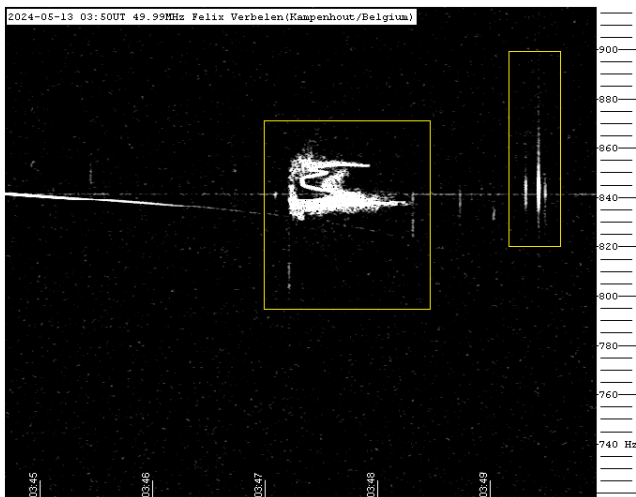*Figure 26* – Meteor echoes May 17, 04ʰ55ᵐ UT.

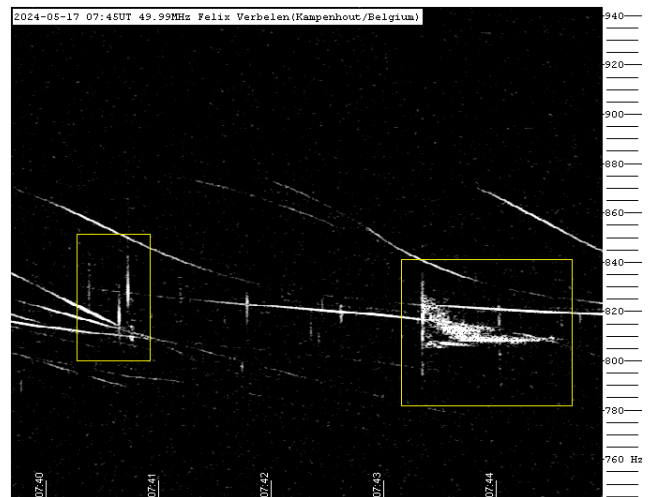*Figure 24* – Meteor echoes May 13, 03ʰ50ᵐ UT.
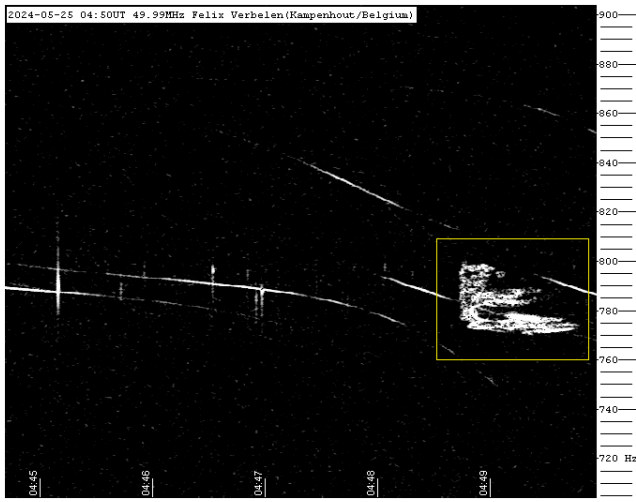

Figure 27 – Meteor echoes May 17, 07ʰ45ᵐ UT.

Figure 28 – Meteor echoes May 25, 04^{h}50^m UT.
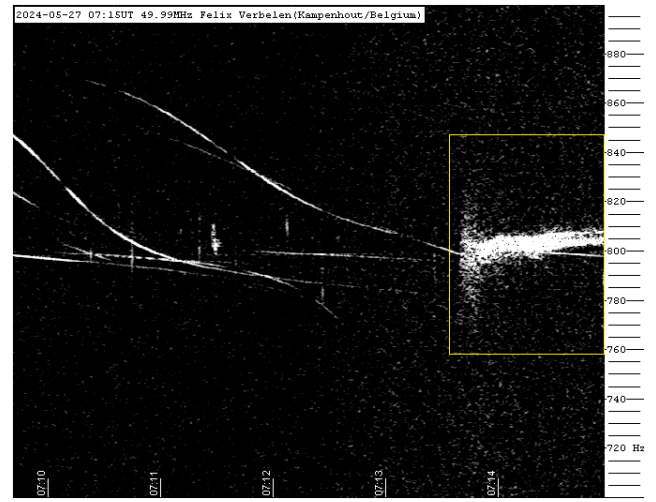

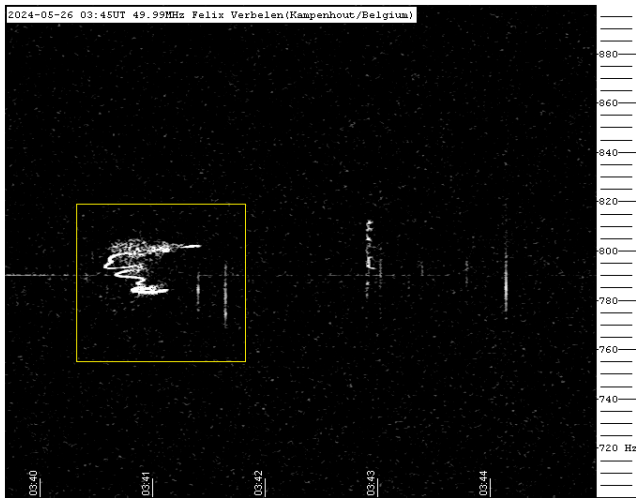*Figure 30* – Meteor echoes May 27, 07^{h}15^m UT.

Figure 29 – Meteor echoes May 26, 03^{h}45^m UT.

The Southwestern Europe Meteor Network: bright bolides observed from April to September 2023

J. M. Madiedo[1], J. L. Ortiz[1], J. Izquierdo[2], P. Santos-Sanz[1], J. Aceituno[3], E. de Guindos[3],
A. San Segundo[4], D. Ávila[5], B. Tosar[6], A. Gómez-Hernández[7], Juan Gómez-Martínez[7],
Antonio García[8], and A.I. Aimee[9]

[1] Departamento de Sistema Solar, Instituto de Astrofísica de Andalucía (IAA-CSIC), 18080 Granada, Spain
madiedo@cica.es, ortiz@iaa.es, psantos@iaa.es

[2] Departamento de Física de la Tierra y Astrofísica, Universidad Complutense de Madrid, 28040 Madrid, Spain
jizquierdo9@gmail.com

[3] Observatorio Astronómico de Calar Alto (CAHA), E-04004, Almería, Spain
aceitun@caha.es, guindos@caha.es

[4] Observatorio El Guijo (MPC J27), Galapagar, Madrid, Spain
mpcj27@outlook.es

[5] Estación de Meteoros de Ayora, Ayora, Valencia, Spain
David_ayora007@hotmail.com

[6] Casa das Ciencias. Museos Científicos Coruñeses. A Coruña, Spain
borjatosar@gmail.com

[7] Estación de Registro La Lloma, Olocau, Valencia, Spain
curso88@gmail.com

[8] Estación de Meteoros de Cullera (Faro de Cullera), Valencia, Spain
antonio.garcia88@joseantoniogarcia.com

[9] Southwestern Europe Meteor Network, 41012 Sevilla, Spain
swemn.server@gmail.com

We present in this report the analysis of some of the notable fireballs recorded in the framework of the Southwestern Europe Meteor Network from April to September 2023. They have been spotted from the Iberian Peninsula. Their peak brightness ranges from mag. –7 to mag. –14. Some of these bright meteors were meteorite-producing fireballs. Fireballs included in this work were linked to different sources: the sporadic background, major meteoroid streams, and poorly-known streams.

1 Introduction

The Southwestern Europe Meteor Network (SWEMN) conducts the SMART project (Spectroscopy of Meteoroids by means of Robotic Technologies), which started operation in 2006 to analyze the physical and chemical properties of meteoroids ablating in the Earth's atmosphere. For this purpose, we employ an array of automated cameras and spectrographs deployed at meteor-observing stations in Spain (Madiedo, 2014; Madiedo, 2017). This allows to derive the luminous path of meteors and the orbit of their progenitor meteoroids, and also to study the evolution of meteor plasmas from the emission spectrum produced by these events (Madiedo, 2015a; 2015b). SMART also provides important information for our MIDAS project, which is being conducted by the Institute of Astrophysics of Andalusia (IAA-CSIC) to study lunar impact flashes produced when large meteoroids impact the Moon (Madiedo et al., 2015; Madiedo et al., 2018; Madiedo et al., 2019; Ortiz et al., 2015).

This report describes the preliminary analysis of 11 bright meteors observed by our systems. This paper has been fully written by AIMEE (acronym for Artificial Intelligence with Meteoroid Environment Expertise) by taking into consideration the information found in the SWEMN fireball database (Madiedo et al., 2021; Madiedo et al., 2022).

2 Equipment and methods

The events presented here have been recorded by using Watec 902H2 and Watec 902 Ultimate cameras. Their field of view ranges from 62 × 50 degrees to 14 × 11 degrees. To record meteor spectra we have attached holographic diffraction gratings (1000 lines/mm) to the lens of some of these cameras. We have also employed digital CMOS color cameras (models Sony A7S and A7SII) operating in HD video mode (1920 × 1080 pixels). These cover a field of view of around 70 × 40 degrees. A detailed description of this hardware and the way it operates was given in previous works (Madiedo, 2017). Besides digital CMOS cameras manufactured by ZWO (model ASI185MC) were used. The

atmospheric paths of the events were triangulated by means of the SAMIA software, developed by J.M. Madiedo. This program employs the planes-intersection method (Ceplecha, 1987).

3 Analysis of the 2023 April 2 event

This extraordinary fireball was spotted on 2023 April 2, at $19^h28^m46.0 \pm 0.1^s$ UT (*Figure 1*). Its peak brightness was equivalent to an absolute magnitude of -13.0 ± 1.0. In the images it can be clearly seen how the meteoroid broke up into multiple fragments along the luminous trajectory of the event. The code assigned to the event in the SWEMN meteor database is SWEMN20230402_192846. A video containing images of the bright meteor and its trajectory in the atmosphere was uploaded to YouTube[11] . Many casual eyewitnesses could also observe the fireball.

Figure 1 – Stacked image of the SWEMN20230402_192846 meteor.

Atmospheric path, radiant and orbit

This fireball overflew the provinces of Madrid and Toledo (Spain). The luminous event began at an altitude $H_b = 87.4 \pm 0.5$ km. The bolide penetrated the atmosphere till a final height $H_e = 24.7 \pm 0.5$ km. The equatorial coordinates concluded for the apparent radiant are $\alpha = 165.40°$, $\delta = +65.96°$. The meteoroid collided with the atmosphere with an initial velocity $v_\infty = 13.5 \pm 0.3$ km/s. The calculated trajectory in our atmosphere of the bright meteor is shown in *Figure 2*. The orbit in the Solar System of the progenitor meteoroid is shown in *Figure 3*.

Table 1 – Orbital data (J2000) of the progenitor meteoroid before its encounter with our planet.

a (AU)	1.34 ± 0.05	ω (°)	192.2 ± 00.1
e	0.25 ± 0.02	Ω (°)	12.476124 ± 10^{-5}
q (AU)	0.9948 ± 0.0003	i (°)	11.4 ± 0.6

Figure 2 – Atmospheric path of the SWEMN20230402_192846 meteor, and its projection on the ground.
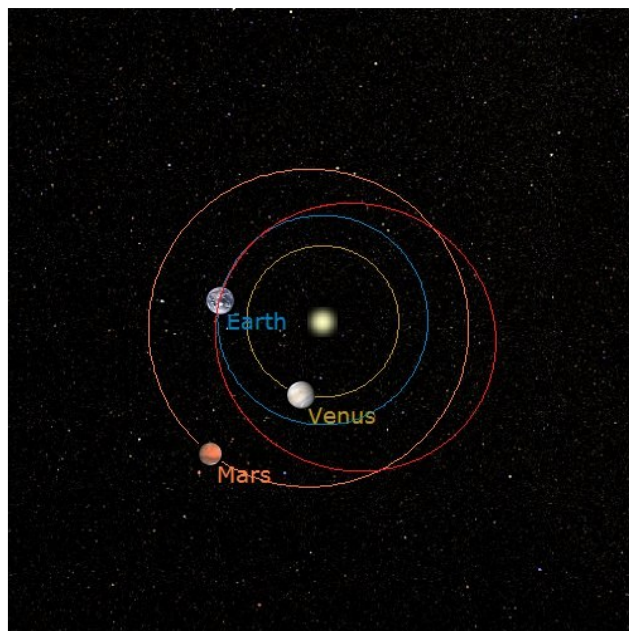

Figure 3 – Projection on the ecliptic plane of the orbit of the parent meteoroid of the SWEMN20230402_192846 meteor.

We named this fireball "Torrejon de Velasco", because the event was located over this locality during its initial phase. The orbital data of the progenitor meteoroid before its encounter with our planet have been listed in *Table 1*, and the geocentric velocity yields $v_g = 7.5 \pm 0.5$ km/s. From the value calculated for the Tisserand parameter with respect to Jupiter ($T_J = 4.84$), we found that the particle was moving on an asteroidal orbit before hitting our atmosphere. By taking into account this orbit and the radiant position, the event was generated by the sporadic background.

According to the analysis of the trajectory in the Earth's atmosphere it was obtained that the meteoroid was not

---

[11] https://youtu.be/u8Dgn8fcl1k

entirely ablated in the atmosphere. Consequently, a portion of it reached the ground as a meteorite.

4   Description of the 2023 April 17 event

This notable bright meteor was captured on 2023 April 17, at $3^h59^m21.0 \pm 0.1^s$ UT. Its peak brightness was equivalent to an absolute magnitude of -12.0 ± 1.0 (*Figure 4*). It exhibited a bright flare at the final phase of its trajectory in the atmosphere as a consequence of the sudden break-up of the meteoroid. It was included in the SWEMN meteor database with the identifier SWEMN20230417_035921. The bright meteor can be viewed on YouTube[12].

Figure 4 – Stacked image of the SWEMN20230417_035921 meteor.

Figure 5 – Atmospheric path of the SWEMN20230417_035921 meteor, and its projection on the ground.

Atmospheric path, radiant and orbit

Having analyzed the path in the atmosphere of the bolide it was deduced that this fireball overflew the province of Toledo (Spain). Its initial altitude was $H_b = 88.3 \pm 0.5$ km. The bolide penetrated the atmosphere till a final height $H_e = 62.0 \pm 0.5$ km. The equatorial coordinates of the apparent radiant yield $\alpha = 291.11°$, $\delta = +36.89°$. Besides, we found that the meteoroid impacted the atmosphere with

---

a velocity $v_\infty = 49.3 \pm 0.3$ km/s. The calculated luminous path of the event is shown in *Figure 5*. The orbit in the Solar System of the progenitor meteoroid is shown in *Figure 6*.

Table 2 – Orbital data (J2000) of the progenitor meteoroid before its encounter with our planet.

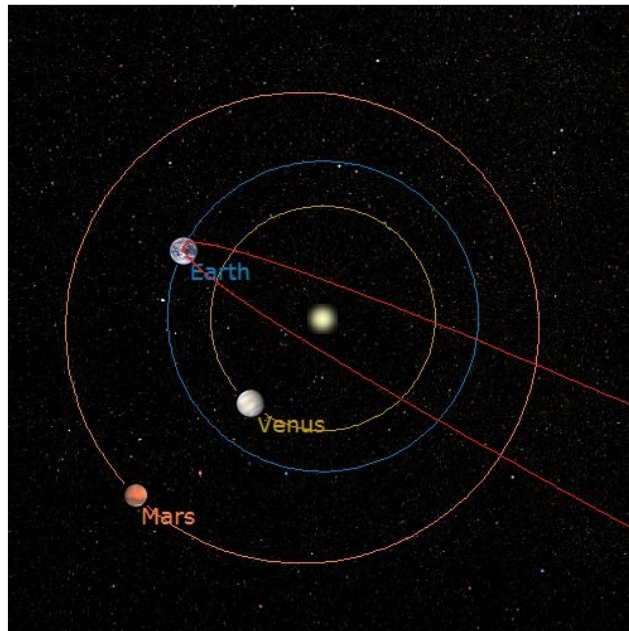| a (AU)	10.2 ± 2.3	ω (º)	171.2 ± 00.1
e	0.90 ± 0.02	Ω (º)	26.579585 ± 10^{-5}
q (AU)	0.99809 ± 0.00009	i (º)	83.7 ± 0.2

Figure 6 – Projection on the ecliptic plane of the orbit of the parent meteoroid of the SWEMN20230417_035921 meteor.

The fireball was named "Pulgar", because the bolide was located near the zenith of this locality during its initial phase. The parameters of the heliocentric orbit of the parent meteoroid before its encounter with our planet have been included in *Table 2*. The value calculated for the geocentric velocity was $v_g = 47.9 \pm 0.3$ km/s. According to the value derived for the Tisserand parameter with respect to Jupiter ($T_J = 0.64$), the particle followed a cometary (HTC) orbit before entering our atmosphere. By taking into account these parameters and the calculated radiant position, the event was linked to the April Lyrids (IAU meteor shower code LYR#0006). The maximum activity of this meteor shower can be observed around April 22. Its proposed progenitor body is C/1861 G1 (Thatcher) (Jenniskens et al., 2016).

5   Analysis of the 2023 August 3 event

This bright meteor was recorded on 2023 August 3 at $22^h10^m08.0 \pm 0.1^s$ UT from the meteor-observing stations located at Huelva, La Hita (Toledo), Calar Alto, Sierra Nevada, La Sagra (Granada), and Sevilla (*Figure 7*). The peak luminosity the bolide, which displayed a bright flare at the terminal stage of its atmospheric trajectory, was equivalent to an absolute magnitude of -7.0 ± 1.0. This

flare arose as a consequence of the sudden disruption of the meteoroid. The identifier given to the bright meteor in the SWEMN meteor database is SWEMN20230803_221008. A video containing images of the bolide and its trajectory in the atmosphere was uploaded to YouTube[13].
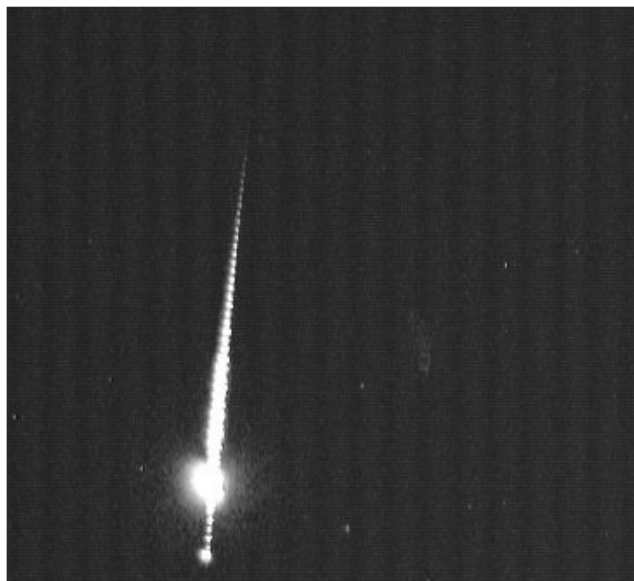

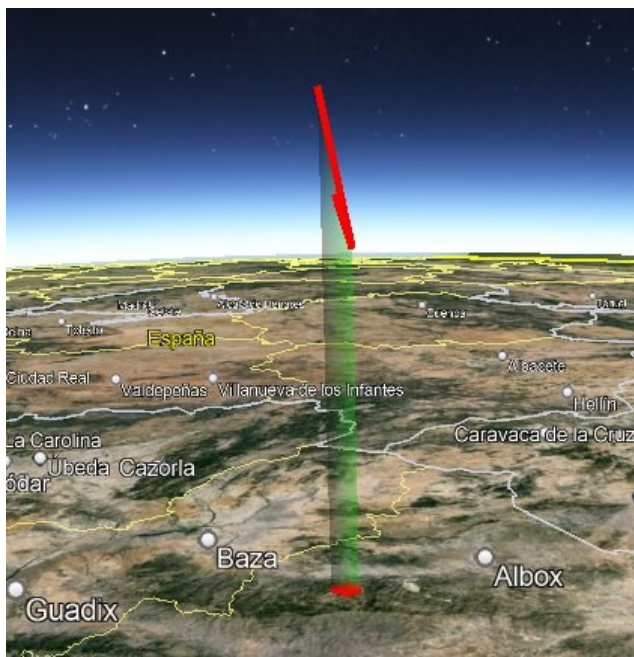*Figure 7* – Stacked image of the SWEMN20230803_221008 meteor.

Figure 8 – Atmospheric path of the SWEMN20230803_221008 meteor, and its projection on the ground.

Atmospheric path, radiant and orbit

The calculation of the trajectory in the atmosphere of the event allowed to deduce that this bolide overflew the province of Almería (south of Spain). The luminous event began at an altitude $H_b = 93.3 \pm 0.5$ km. The event penetrated the atmosphere till a final height $H_e = 65.6 \pm 0.5$ km. The apparent radiant was located at the equatorial coordinates $\alpha = 268.60°$, $\delta = +37.23°$. The entry velocity in the atmosphere inferred for the progenitor meteoroid was $v_\infty = 19.3 \pm 0.2$ km/s. *Figure 8* shows the obtained path in

the atmosphere of the bolide. The orbit in the Solar System of the progenitor meteoroid is shown in *Figure 9*.

Table 3 – Orbital data (J2000) of the progenitor meteoroid before its encounter with our planet.

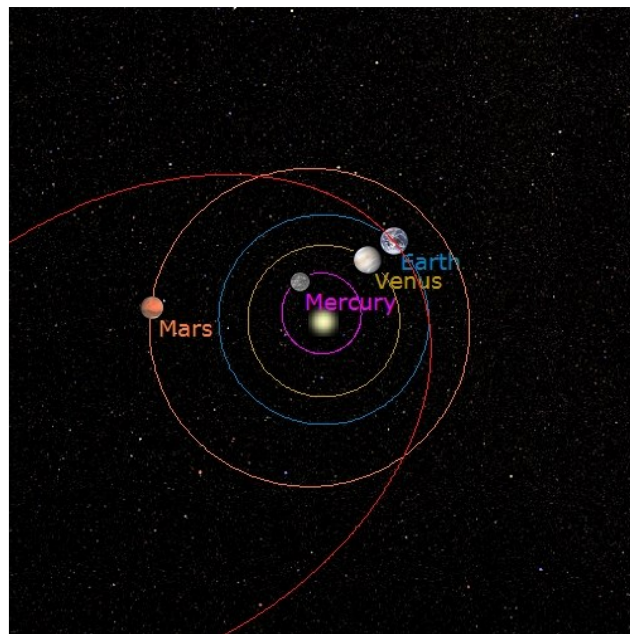|			
a (AU)	3.1 ± 0.1	ω (º)	200.34 ± 00.04
e	0.68 ± 0.01	Ω (º)	130.992686 ± 10^{-5}
q (AU)	0.9890 ± 0.0002	i (º)	21.3 ± 0.2

Figure 9 – Projection on the ecliptic plane of the orbit of the parent meteoroid of the SWEMN20230803_221008 meteor.

The name given to the bolide was "La Mojonera", because the event was located over this locality during its initial phase. The parameters of the heliocentric orbit of the parent meteoroid before its encounter with our planet are listed in *Table 3*. The geocentric velocity obtained for the particle yields $v_g = 15.9 \pm 0.2$ km/s. From the value obtained for the Tisserand parameter with respect to Jupiter ($T_J = 2.73$), we found that before striking the Earth's atmosphere the particle was moving on a cometary (JFC) orbit. These values and the derived radiant position do not correspond with any of the meteoroid streams included in the IAU meteor database. So, it was concluded that the fireball was produced by a sporadic meteoroid.

6   Description of the 2023 August 13 event

This bright bolide was captured on 2023 August 13 at $0^h24^m53.0 \pm 0.1^s$ UT from the meteor-observing stations located at Huelva, La Hita (Toledo), Calar Alto, Sierra Nevada, and La Sagra (Granada). The peak brightness the event, which showed different flares along its atmospheric path, was equivalent to an absolute magnitude of $–9.0 \pm 1.0$ (*Figure 10*). These flares took place as a consequence of the sudden disruption of the meteoroid. The fireball was included in our meteor database with the unique identifier

---

[13] https://youtu.be/HckGbR3EyXk

SWEMN20230813_002453. A video about this event can be viewed on YouTube[14].

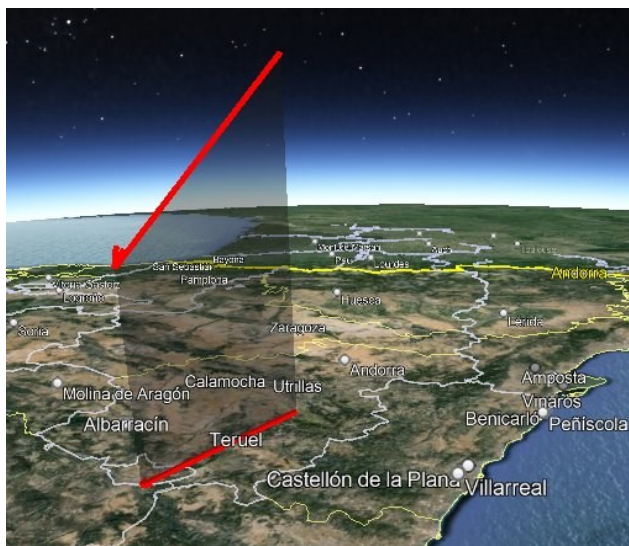*Figure 10* – Stacked image of the SWEMN20230402_192846 meteor.

Figure 11 – Atmospheric path of the SWEMN20230402_192846 meteor, and its projection on the ground.

Atmospheric path, radiant and orbit

The analysis of the path in the atmosphere of the fireball allowed to infer that this bolide overflew the provinces of Teruel, Valencia, and Cuenca (Spain). The meteoroid started ablating at a height $H_b = 132.1 \pm 0.5$ km, and the fireball penetrated the atmosphere till a final height $H_e = 72.7 \pm 0.5$ km. The apparent radiant was located at the equatorial coordinates $\alpha = 44.89º$, $\delta = +57.16º$. The entry velocity in the atmosphere found for the progenitor meteoroid was $v_\infty = 60.4 \pm 0.3$ km/s. The calculated atmospheric trajectory of the bright meteor is shown in *Figure 11*. The orbit in the Solar System of the progenitor meteoroid is shown in *Figure 12*.

Table 4 – Orbital data (J2000) of the progenitor meteoroid before its encounter with our planet.

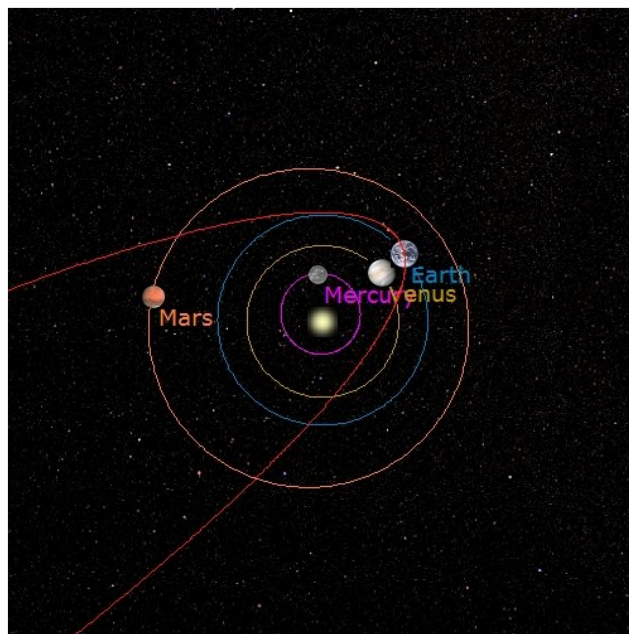| a (AU)	12.4 ± 3.9	ω (º)	154.3 ± 00.4
e	0.92 ± 0.02	Ω (º)	139.714997 ± 10^{-5}
q (AU)	0.9654 ± 0.0008	i (º)	113.8 ± 0.1

Figure 12 – Projection on the ecliptic plane of the orbit of the parent meteoroid of the SWEMN20230402_192846 meteor.

The orbital data of the parent meteoroid before its encounter with our planet are listed in *Table 4*. The geocentric velocity obtained for the particle yields $v_g = 59.2 \pm 0.3$ km/s. The Tisserand parameter with respect to Jupiter ($T_J = –0.06$) reveals that the meteoroid followed a cometary (HTC) orbit before hitting our atmosphere. These data and the calculated radiant location confirm that the bolide was linked to the Perseids (IAU meteor shower code PER#0007). Since the Perseids reach their peak on August 12, this event was spotted near this activity peak. The proposed meteor body of this parent shower is 109P/Swift-Tuttle (Jenniskens et al., 2016).

7   Analysis of the 2023 August 14 fireball

This bright bolide was captured on 2023 August 14, at $4^h21^m39.0 \pm 0.1^s$ UT, from the SWEMN meteor-observing stations located at Huelva, La Hita (Toledo), Calar Alto, Sierra Nevada, La Sagra (Granada), and Sevilla. Its peak luminosity was equivalent to an absolute magnitude of $–9.0 \pm 1.0$ (*Figure 13*). It displayed different flares along its luminous path as a consequence of the sudden break-up of the meteoroid. The unique identifier given to the bolide in the SWEMN meteor database is SWEMN20230814_042139. The fireball can be viewed on YouTube[15].

---

[14] https://youtu.be/SjfpjOOBVrA

[15] https://youtu.be/5-v4bEr2tdM

Figure 13 – Stacked image of the SWEMN20230814_042139 meteor.
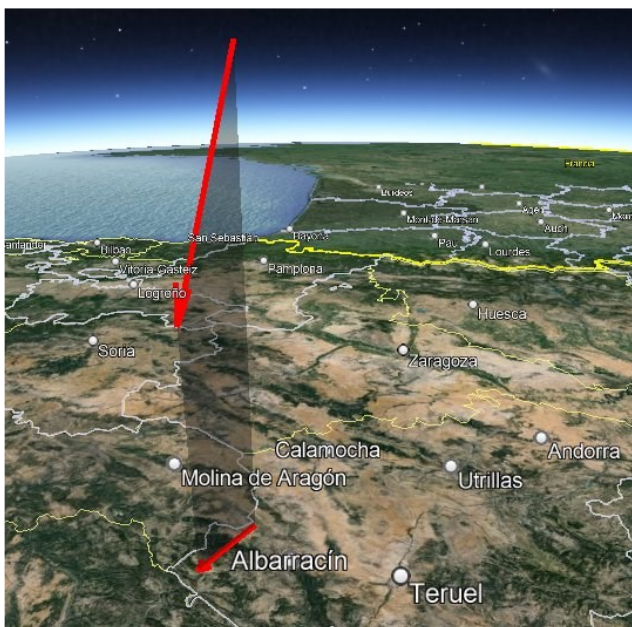

Figure 14 – Atmospheric path of the SWEMN20230814_042139 meteor, and its projection on the ground.

Atmospheric path, radiant and orbit

This fireball overflew the province of Teruel (Spain). The luminous event began at an altitude $H_b = 130.8 \pm 0.5$ km. The bolide penetrated the atmosphere till a final height $H_e = 71.3 \pm 0.5$ km. The apparent radiant was located at the equatorial coordinates $\alpha = 50.33º$, $\delta = 56.77º$. The entry velocity in the atmosphere deduced for the parent meteoroid was $v_\infty = 60.7 \pm 0.4$ km/s. The calculated trajectory in the atmosphere of the event is shown in *Figure 14*. The orbit in the Solar System of the progenitor meteoroid is shown in *Figure 15*.

Table 5 – Orbital data (J2000) of the progenitor meteoroid before its encounter with our planet.

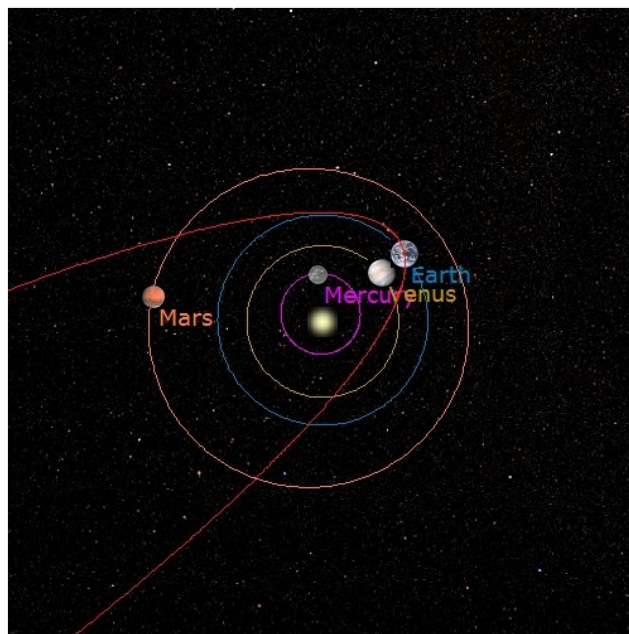| a (AU)	13.2 ± 5.8	ω (º)	149.9 ± 0.6
e	0.92 ± 0.03	Ω (º)	140.83286 ± 10^{-5}
q (AU)	0.947 ± 0.001	i (º)	115.1 ± 0.2

Figure 15 – Projection on the ecliptic plane of the orbit of the parent meteoroid of the SWEMN20230814_042139 meteor.

The bright meteor was named "Guadalaviar", since the fireball overflew this locality during its final phase. The orbital data of the parent meteoroid before its encounter with our planet have been listed in *Table 5*, and the geocentric velocity yields $v_g = 59.5 \pm 0.4$ km/s. Before impacting our atmosphere, the particle was moving on a cometary orbit. These values and the calculated radiant location confirm that the bolide was linked to the Perseids (IAU code PER#0007). This meteor shower has its maximum activity around August 12, and its proposed progenitor body is 109P/Swift-Tuttle (Jenniskens et al., 2016).

8   The 2023 August 15 bolide

We captured this bright bolide from our meteor-observing stations located at Huelva, La Hita (Toledo), Calar Alto, Sierra Nevada, La Sagra (Granada), and Sevilla (*Figure 16*). The fireball was spotted on 2023 August 15, at $3^h23^m42.0 \pm 0.1^s$ UT. The bright meteor, that showed a bright flare at the final stage of its path in the atmosphere, had a peak absolute magnitude of -8.0 ± 1.0. This flare appeared as a consequence of the sudden disruption of the meteoroid. The code given to the fireball in the SWEMN meteor database is SWEMN20230815_032342. A video about this bolide was uploaded to YouTube[16].

---

[16] https://youtu.be/ILqBGvOXuPQ

Figure 16 – Stacked image of the SWEMN20230815_032342 meteor.
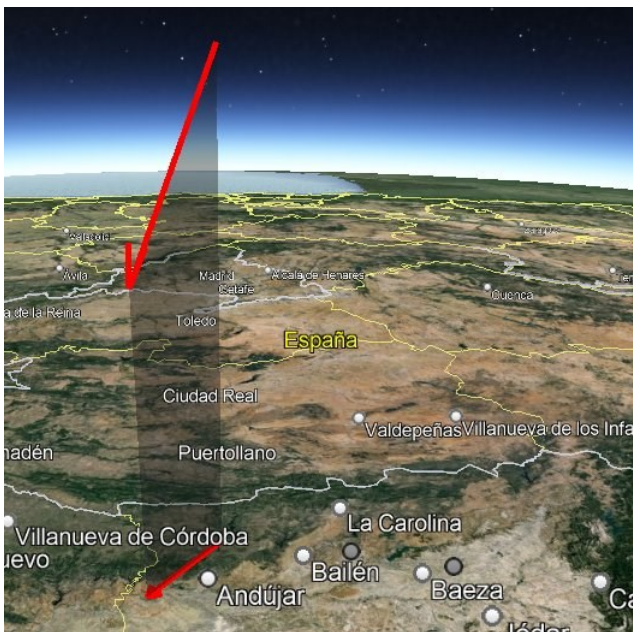

Figure 17 – Atmospheric path of the SWEMN20230815_032342 meteor, and its projection on the ground.

Atmospheric path, radiant and orbit

It was found from the analysis of the trajectory in the atmosphere of the event that this bright meteor overflew the province of Jaén (south of Spain). The meteoroid started ablating at a height $H_b = 119.9 \pm 0.5$ km, and the terminal point of the luminous path was located at a height $H_e = 75.6 \pm 0.5$ km. From the analysis of the atmospheric path, we also inferred that the apparent radiant was located at the position $\alpha = 52.24°$, $\delta = +55.43°$. The pre-atmospheric velocity concluded for the meteoroid yields $v_\infty = 61.3 \pm 0.4$ km/s. *Figure 17* shows the obtained path in the atmosphere

[17] https://youtu.be/Xo55urDSRdE

of the bolide. The orbit in the Solar System of the progenitor meteoroid is shown in *Figure 18*.

Table 6 – Orbital data (J2000) of the progenitor meteoroid before its encounter with our planet.

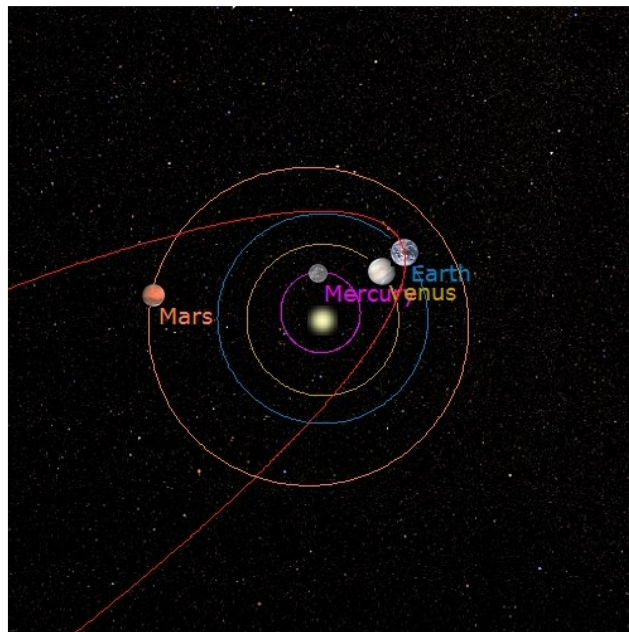| a (AU)	10.6 ± 3.8	ω (°)	148.7 ± 0.2
e	0.91 ± 0.03	Ω (°)	141.75464 ± 10^{-5}
q (AU)	0.942 ± 0.001	i (°)	117.6 ± 0.2

Figure 18 – Projection on the ecliptic plane of the orbit of the parent meteoroid of the SWEMN20230815_032342 meteor.

This bolide was named "La Lancha", because the event overflew this locality during its initial phase. The parameters of the heliocentric orbit of the progenitor meteoroid before its encounter with our planet are listed in *Table 6*, and the geocentric velocity yields $v_g = 60.1 \pm 0.4$ km/s. The meteoroid was moving on a cometary orbit before striking the Earth's atmosphere. These data and the calculated radiant location confirm that the fireball was generated by the Perseids (IAU shower code PER#0007). This meteor shower reaches its peak around August 12, and its proposed parent body is 109P/Swift-Tuttle (Jenniskens et al., 2016).

9   Analysis of the 2023 August 20 event

This breathtaking event was captured on 2023 August 20, at $1^h56^m32.0 \pm 0.1^s$ UT (*Figure 19*). It had a peak absolute magnitude of -14.0 ± 1.0. It was included in the SWEMN meteor database with the identifier SWEMN20230820_015632. A video with images of the event and its luminous path was uploaded to YouTube[17].

Atmospheric path, radiant and orbit

This bolide overflew Morocco. Its initial altitude was $H_b = 96.7 \pm 0.5$ km. The bright meteor penetrated the atmosphere till a final height $H_e = 31.4 \pm 0.5$ km. The

equatorial coordinates of the apparent radiant yield $\alpha = 308.00°$, $\delta = +27.44°$. The entry velocity in the atmosphere obtained for the progenitor meteoroid was $v_\infty = 16.9 \pm 0.3$ km/s. The calculated trajectory in our atmosphere of the bright meteor is shown in *Figure 20*. The orbit in the Solar System of the progenitor meteoroid is shown in *Figure 21*.

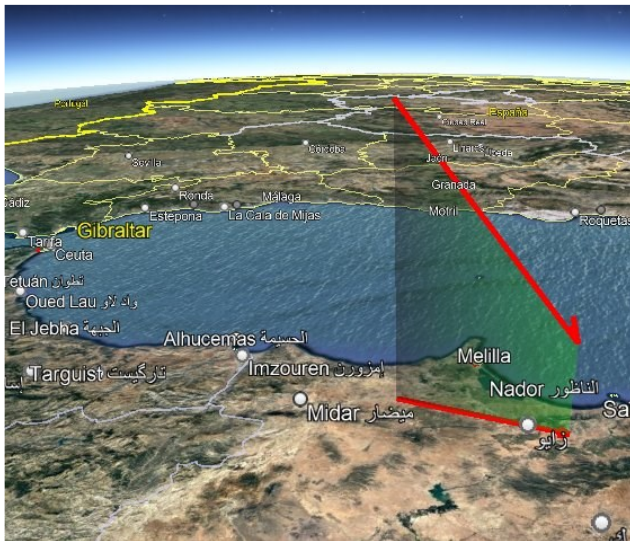*Figure 19* – Stacked image of the SWEMN20230820_015632 meteor.

Figure 20 – Atmospheric path of the SWEMN20230820_015632 meteor, and its projection on the ground.

Table 7 – Orbital data (J2000) of the progenitor meteoroid before its encounter with our planet.

a (AU)	1.63 ± 0.03	ω (°)	232.1 ± 00.7
e	0.45 ± 0.01	Ω (°)	146.496235 ± 10^{-5}
q (AU)	0.889 ± 0.004	i (°)	15.6 ± 0.4

Table 7 shows the parameters of the orbit in the Solar System of the progenitor meteoroid before its encounter with our planet. The geocentric velocity of the meteoroid was $v_g = 13.1 \pm 0.4$ km/s. According to the value derived for the Tisserand parameter with respect to Jupiter ($T_J = 4.15$), the particle followed an asteroidal orbit before striking the atmosphere. These values and the derived

radiant coordinates confirm that the bolide was produced by the sporadic background.
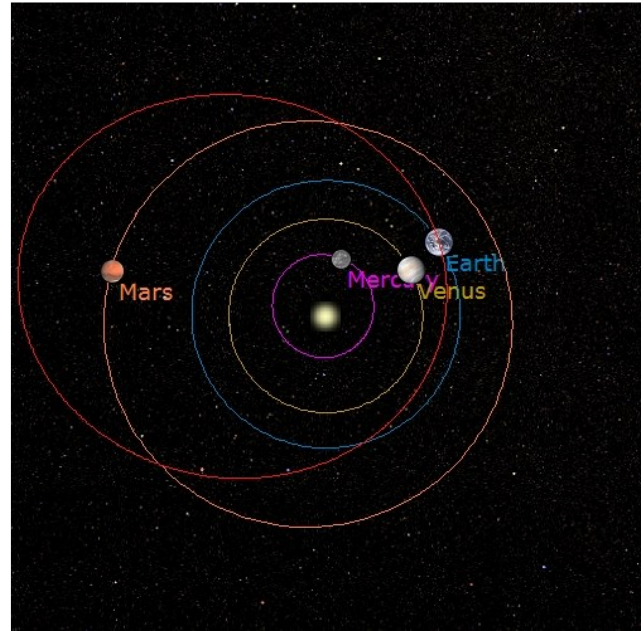

Figure 21 – Projection on the ecliptic plane of the orbit of the parent meteoroid of the SWEMN20230820_015632 meteor.

10 Analysis of the 2023 August 25 bolide

This bright event was spotted by our systems on 2023 August 25, at $23^h51^m38.0 \pm 0.1^s$ UT. Its maximum luminosity was equivalent to an absolute magnitude of -7.0 ± 1.0 (*Figure 22*). It showed several flares along its trajectory in the atmosphere as a consequence of the sudden disruption of the meteoroid. The unique identifier assigned to the event in the SWEMN meteor database is SWEMN20230825_235138. The bolide can be viewed on YouTube[18].

Figure 22 – Stacked image of the SWEMN20230825_235138 meteor.

Atmospheric path, radiant and orbit
This bright meteor overflew the provinces of Sevilla and Cádiz (south of Spain). The luminous event began at an altitude $H_b = 103.6 \pm 0.5$ km. It penetrated the atmosphere

---

[18] https://youtu.be/C3nrara_y5Q

till a final height $H_e = 64.5 \pm 0.5$ km. The position found for the apparent radiant corresponds to the equatorial coordinates $\alpha = 273.73°$, $\delta = +62.38°$. Besides, we obtained that the meteoroid impacted the atmosphere with a velocity $v_\infty = 24.9 \pm 0.3$ km/s. The calculated atmospheric trajectory of the bolide is shown in *Figure 23*. The orbit in the Solar System of the progenitor meteoroid is shown in *Figure 24*.

Table 8 – Orbital data (J2000) of the progenitor meteoroid before its encounter with our planet.

a (AU)	3.3 ± 0.2	ω (°)	182.93 ± 00.06
e	0.69 ± 0.01	Ω (°)	152.197295 ± 10^{-5}
q (AU)	1.01021 ± 0.00003	i (°)	35.4 ± 0.3

Figure 23 – Atmospheric path of the SWEMN20230825_235138 meteor, and its projection on the ground.
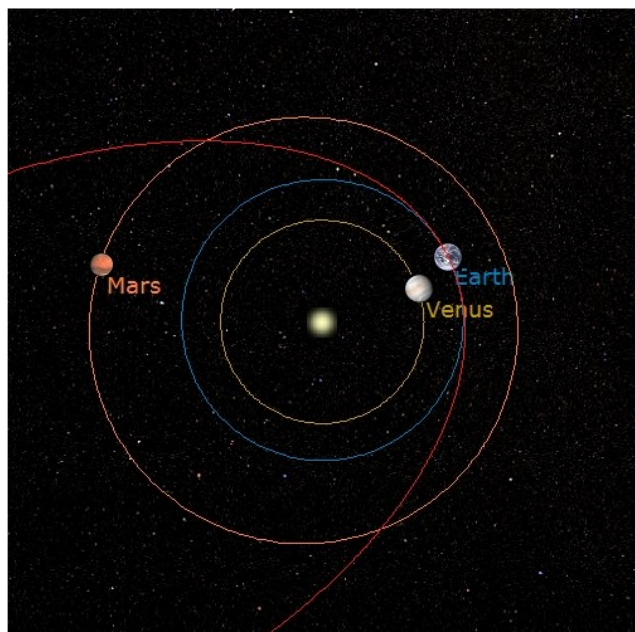
Figure 24 – Projection on the ecliptic plane of the orbit of the parent meteoroid of the SWEMN20230825_235138 meteor.

The name given to the event was "Los Izquierdos", since the bright meteor overflew this locality during its final phase. The parameters of the heliocentric orbit of the

progenitor meteoroid before its encounter with our planet have been listed in *Table 8*, and the geocentric velocity derived in this case was $v_g = 22.5 \pm 0.3$ km/s. The Tisserand parameter with respect to Jupiter ($T_J = 2.49$) shows that the particle was moving on a cometary (JFC) orbit before impacting the atmosphere. By taking into account these parameters and the derived radiant location, the bolide was produced by the κ-Cygnids (IAU code KCG#0012).

11 Analysis of the 2023 September 8 event

On 2023 September 8, at $21^h40^m19.0 \pm 0.1^s$ UT, our meteor stations captured this imposing fireball. It had a peak absolute magnitude of -13.0 ± 1.0 (*Figure 25*), and showed a series of flares along its trajectory in our atmosphere as a consequence of the sudden disruption of the meteoroid. The recordings clearly reveal that the meteoroid broke up into multiple pieces along the meteor path. The identifier assigned to the fireball in the SWEMN meteor database is SWEMN20230908_214019. The event can be viewed on YouTube[19]. Many casual eyewitnesses could also observe the fireball.
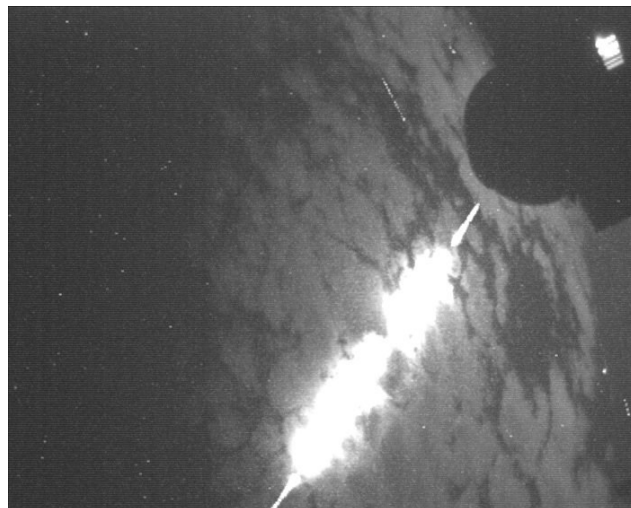

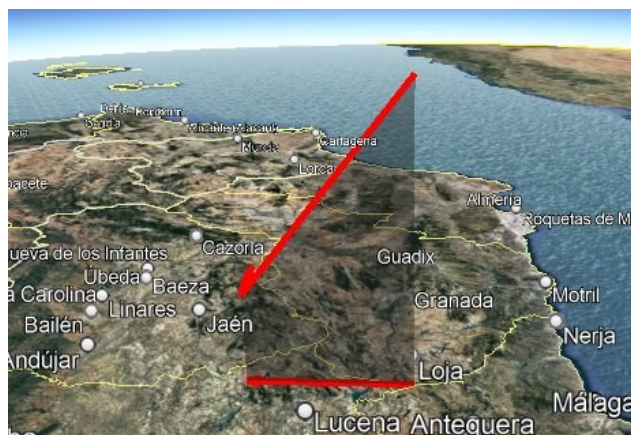*Figure 25* – Stacked image of the SWEMN20230908_214019 meteor.

Figure 26 – Atmospheric path of the SWEMN20230908_214019 meteor, and its projection on the ground.

---

[19] https://youtu.be/spBAIMkBl_0

Atmospheric path, radiant and orbit

By calculating the atmospheric path of the bolide it was deduced that this event overflew the provinces of Granada and Córdoba (south of Spain). The luminous event began at an altitude $H_b = 87.8 \pm 0.5$ km. The bolide penetrated the atmosphere till a final height $H_e = 26.4 \pm 0.5$ km. The equatorial coordinates of the apparent radiant yield $\alpha = 306.24º$, $\delta = -0.44º$. The pre-atmospheric velocity obtained for the meteoroid yields $v_\infty = 15.6 \pm 0.0$ km/s. The calculated trajectory in our atmosphere of the bright meteor is shown in *Figure 26*. The orbit in the Solar System of the progenitor meteoroid is shown in *Figure 27*.

Table 9 – Orbital data (J2000) of the progenitor meteoroid before its encounter with our planet.

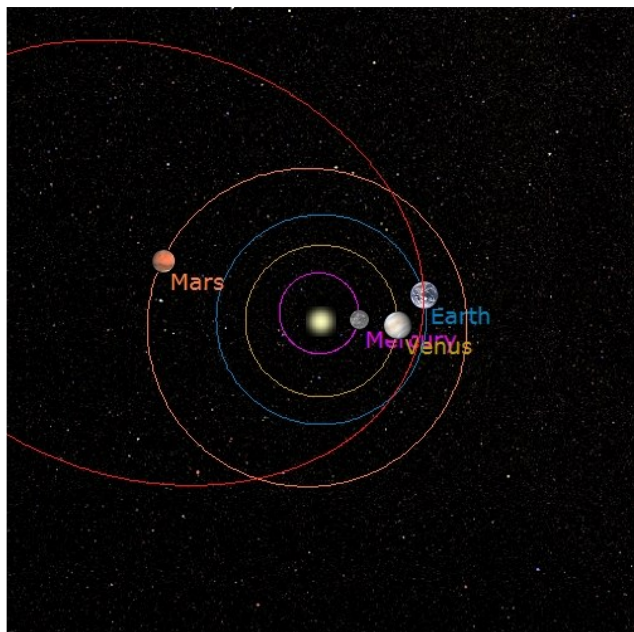|			
a (AU)	2.70 ± 0.01	ω (º)	212.6 ± 00.2
e	0.650 ± 0.001	Ω (º)	165.646847 ± 10^{-5}
q (AU)	0.9446 ± 0.0006	i (º)	3.66 ± 0.01

Figure 27 – Projection on the ecliptic plane of the orbit of the parent meteoroid of the SWEMN20230908_214019 meteor.

Table 9 shows the orbital parameters of the progenitor meteoroid before its encounter with our planet. The geocentric velocity of the meteoroid was $v_g = 11.0 \pm 0.0$ km/s. The value found for the Tisserand parameter referred to Jupiter ($T_J = 3.02$) reveals that before striking the Earth's atmosphere the particle was moving on an asteroidal orbit. These values and the derived radiant position confirm that the bolide was linked to the sporadic background.

As a result of the analysis of the terminal point of the trajectory in the Earth's atmosphere we deduced that the event was a potential meteorite-producer. Therefore, part of the meteoroid survived the ablation process and reached the ground.

---

[20] https://youtu.be/g83GewguLvY

12 The 2023 September 13 meteor

This imposing event was recorded by our cameras at $2^h06^m36.0 \pm 0.1^s$ UT on 2023 September 13 (*Figure 28*). The maximum luminosity the bright meteor, which showed different flares along its trajectory in our atmosphere, was equivalent to an absolute magnitude of -14.0 ± 1.0. These flares occurred as a consequence of the sudden disruption of the meteoroid. The recordings clearly reveal that the meteoroid was fragmented into a series of pieces along the meteor trajectory. The code assigned to the event in the SWEMN meteor database is SWEMN20230913_020636. A video about this bright meteor was uploaded to YouTube[20].

Figure 28 – Stacked image of the SWEMN20230913_020636 meteor.

Atmospheric path, radiant and orbit

It was concluded by calculating the trajectory in the atmosphere of the event that this bright meteor overflew the provinces of Granada and Jaén (south of Spain). The ablation process of the meteoroid began at a height $H_b = 99.1 \pm 0.5$ km, with the terminal point of the luminous phase located at a height $H_e = 36.2 \pm 0.5$ km. The equatorial coordinates of the apparent radiant yield $\alpha = 353.94º$, $\delta = -2.87º$. Besides, we found that the meteoroid collided with the atmosphere with a velocity $v_\infty = 24.7 \pm 0.2$ km/s. *Figure 29* shows the calculated trajectory in our atmosphere of the bright meteor. The orbit in the Solar System of the progenitor meteoroid is shown in *Figure 30*.

Table 10 – Orbital data (J2000) of the progenitor meteoroid before its encounter with our planet.

a (AU)	2.41 ± 0.05	ω (º)	90.27 ± 00.09
e	0.764 ± 0.007	Ω (º)	349.754328 ± 10^{-5}
q (AU)	0.568 ± 0.002	i (º)	1.13 ± 0.01

Figure 29 – Atmospheric path of the SWEMN20230913_020636 meteor, and its projection on the ground.
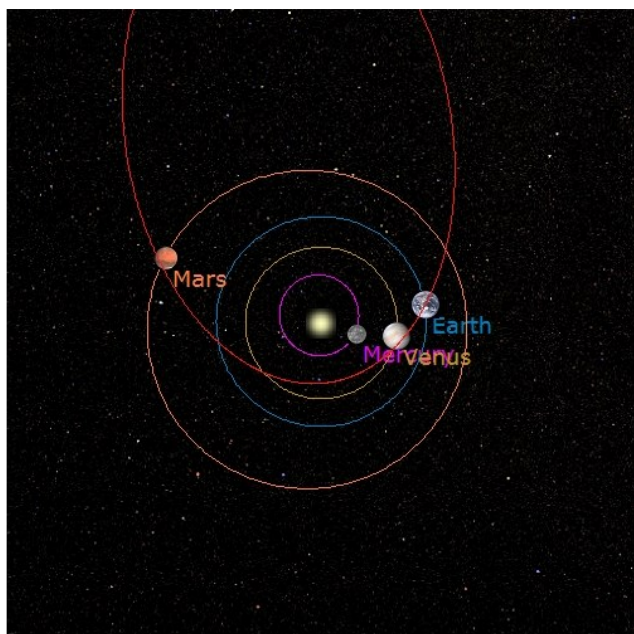

Figure 30 – Projection on the ecliptic plane of the orbit of the parent meteoroid of the SWEMN20230913_020636 meteor.

This event was named "Moraleda de Zafayona", because the fireball overflew this locality during its initial phase. The parameters of the heliocentric orbit of the progenitor meteoroid before its encounter with our planet can be found in *Table 10*. The geocentric velocity of the meteoroid was $v_g = 22.3 \pm 0.2$ km/s. According to the value found for the Tisserand parameter with respect to Jupiter ($T_J = 3.04$), the particle was moving on an asteroidal orbit before colliding with our planet's atmosphere. By taking into account these values and the calculated radiant position, the fireball was generated by the sporadic component.

13 Analysis of the 2023 September 27 fireball

We recorded this striking fireball from the meteor-observing stations located at Huelva, La Hita (Toledo), Calar Alto, Sierra Nevada, La Sagra (Granada), and Sevilla (*Figure 31*). The bright meteor was spotted on 2023 September 27, at $3^h27^m04.0 \pm 0.1^s$ UT. Its peak luminosity was equivalent to an absolute magnitude of -12.0 ± 1.0. The images clearly show that the meteoroid was fragmented into several pieces along the meteor trajectory. It was added to the SWEMN meteor database with the code SWEMN20230927_032704. The bolide can be viewed on YouTube[21].

Figure 31 – Stacked image of the SWEMN20230927_032704 meteor.
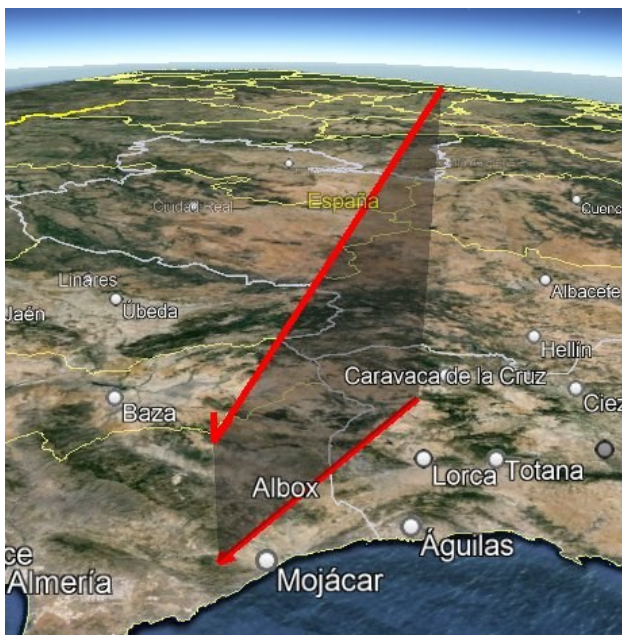

Figure 32 – Atmospheric path of the SWEMN20230927_032704 meteor, and its projection on the ground.

Atmospheric path, radiant and orbit

This bolide overflew the provinces of Murcia and Almería (south of Spain). Its initial altitude was $H_b = 97.6 \pm 0.5$ km. The event penetrated the atmosphere till a final height $H_e = 35.2 \pm 0.5$ km. The equatorial coordinates of the apparent radiant yield $\alpha = 207.83°$, $\delta = +83.89°$. The pre-atmospheric velocity obtained for the meteoroid yields $v_\infty = 35.6 \pm 0.3$ km/s. The calculated luminous path of the

---

[21] https://youtu.be/noUZeXshhm0

bolide is shown in *Figure 32*. The orbit in the Solar System of the progenitor meteoroid is shown in *Figure 33*.
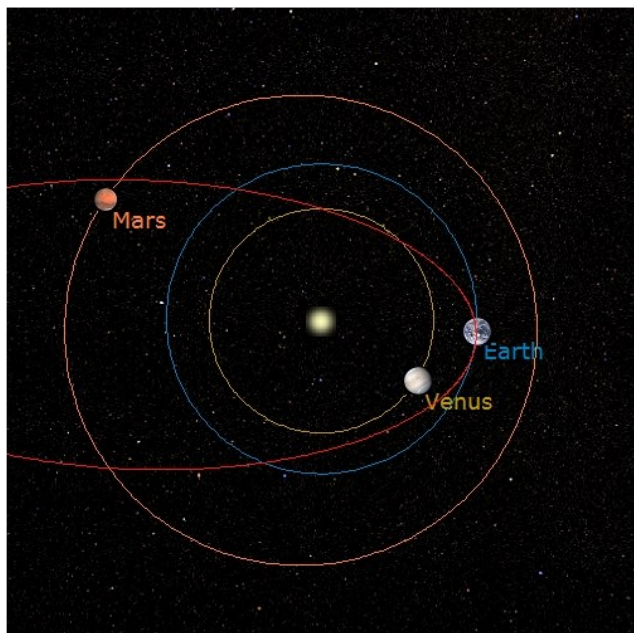

Figure 33 – Projection on the ecliptic plane of the orbit of the parent meteoroid of the SWEMN20230927_032704 meteor.

Table 11 – Orbital data (J2000) of the progenitor meteoroid before its encounter with our planet.

a (AU)	2.19 ± 0.07	ω (º)	170.5 ± 00.2
e	0.54 ± 0.01	Ω (º)	183.455694 ± 10⁻⁵
q (AU)	0.9976 ± 0.0001	i (º)	59.6 ± 0.3

The name given to the fireball was "Cortijo Grande", because the bright meteor was located over this locality during its final phase. *Table 11* shows the parameters of the orbit in the Solar System of the progenitor meteoroid before its encounter with our planet. The value calculated for the geocentric velocity was $v_g = 33.8 \pm 0.3$ km/s. From the value obtained for the Tisserand parameter referred to Jupiter ($T_J = 2.92$), we found that before entering our planet's atmosphere the particle was moving on a cometary (JFC) orbit. By taking into account these data and the calculated radiant location, the bolide was linked to the ε-Ursae Minorids (IAU code EPU#1044).

14 Conclusions

We have analyzed in this paper some of the most important bolides recorded by our meteor-observing stations between April and September 2023. Their peak absolute luminosity ranges from mag. –7 to mag. –14.

We have discussed the "Torrejon de Velasco" bolide, that was recorded on April 2. The peak magnitude of this sporadic, which overflew the provinces of Madrid and Toledo (Spain), was –13.0. The progenitor meteoroid was moving on an asteroidal orbit before hitting our planet's atmosphere. This deep-penetrating fireball reached an ending altitude of about 24 km. The analysis of the ending point of the luminous path indicates that the meteoroid was

not completely destroyed in the atmosphere. So, this meteor event was a potential meteorite-producer.

The next bolide presented here was a bright meteor recorded on April 17 that was named "Pulgar". The peak magnitude of this April Lyrid (LYR#0006), which overflew Toledo, was –12.0. Before impacting our planet's atmosphere the meteoroid was moving on a cometary (HTC) orbit.

We have also described an event that was recorded on August 3 named "La Mojonera". Its peak absolute magnitude was –7.0. The meteor event was produced by a sporadic meteoroid and overflew the province of Almería (south of Spain). This meteoroid followed a cometary (JFC) orbit before impacting our atmosphere.

On August 13 our systems recorded a bright meteor that reached a peak absolute magnitude of –9.0. It belonged to the Perseids (PER#0007). This bolide overflew the provinces of Teruel, Valencia, and Cuenca (Spain). The particle was moving on a cometary (HTC) orbit before entering our planet's atmosphere. This report also includes two more remarkable Perseids spotted over Spain on August 14 and August 15, respectively.

The next event discussed here was a fireball recorded on August 20. This sporadic fireball had a peak absolute magnitude of –14.0 and overflew Morocco. The progenitor meteoroid followed an asteroidal orbit before striking our atmosphere. At the terminal stage of its luminous phase this deep-penetrating meteor event was located at an altitude of about 31 km.

We have also discussed a κ-Cygnid fireball recorded on August 25 that was named "Los Izquierdos". Its peak magnitude was –7.0. The bolide overflew the provinces of Sevilla and Cádiz (south of Spain). The parent meteoroid followed a cometary (JFC) orbit before colliding with the Earth's atmosphere.

Another potential meteorite-dropper was the bolide recorded on September 8. Its peak absolute magnitude was –13.0. The fireball was produced by a sporadic meteoroid and overflew the provinces of Granada and Córdoba (south of Spain). Its parent meteoroid was moving on an asteroidal orbit before colliding with our atmosphere. At the ending stage of its luminous phase this deep-penetrating meteor event was located at a height of about 26 km.

The "Moraleda de Zafayona" event, that was recorded on September 13, reached a peak magnitude of –14.0 and was associated with the sporadic background. This fireball overflew the provinces of Granada and Jaén (south of Spain). Before impacting our atmosphere, the progenitor meteoroid was moving on an asteroidal orbit. At the ending stage of its luminous phase this deep-penetrating bolide was located at a height of about 36 km.

And the last event described here was the "Cortijo Grande" fireball, that was recorded on September 27. This ε-Ursae Minorid (EPU#1044) meteor had a peak absolute

magnitude of –12.0 and overflew the provinces of Murcia and Almería (southeast of Spain). Its parent meteoroid was moving on a cometary (JFC) orbit before striking the Earth's atmosphere. At the ending stage of its luminous phase this deep-penetrating meteor was located at an altitude of about 35 km.

Acknowledgment

References

Borovička J. (1993). "A fireball spectrum analysis". *A&A*, **279**, 627–645.

Ceplecha Z. (1987). "Geometric, dynamic, orbital and photometric data on meteoroids from photographic fireball networks". *Bull. Astron. Inst. Cz.*, **38**, 222–234.

Jenniskens P., Nénon Q., Albers J., Gural P. S., Haberman B., Holman D., Morales R., Grigsby B. J., Samuels D. and Johannink C. (2016). "The established meteor showers as observed by CAMS". *Icarus*, **266**, 331–354.

Madiedo J. M. (2014). "Robotic systems for the determination of the composition of solar system materials by means of fireball spectroscopy". *Earth, Planets & Space*, **66**, 70.

Madiedo J. M. (2017). "Automated systems for the analysis of meteor spectra: The SMART Project". *Planetary and Space Science*, **143**, 238–244.

Madiedo J. M. (2015a). "Spectroscopy of a κ-Cygnid fireball afterglow". *Planetary and Space Science*, **118**, 90–94.

Madiedo J. M. (2015b). "The ρ-Geminid meteoroid stream: orbits, spectroscopic data and implications for its parent body". *Monthly Notices of the Royal Astronomical Society*, **448**, 2135–2140.

Madiedo J. M., Ortiz J. L., Organero F., Ana-Hernández L., Fonseca F., Morales N. and Cabrera-Caño J. (2015). "Analysis of Moon impact flashes detected during the 2012 and 2013 Perseids". *A&A*, **577**, A118.

Madiedo J. M., Ortiz J. L. and Morales N. (2018). "The first observations to determine the temperature of a lunar impact flash and its evolution". *Monthly Notices of the Royal Astronomical Society*, **480**, 5010–5016.

Madiedo J. M., Ortiz J. L., Morales N. and Santos-Sanz P. (2019a). "Multiwavelength observations of a bright impact flash during the 2019 January total lunar eclipse". *Monthly Notices of the Royal Astronomical Society*, **486**, 3380–3387.

Madiedo J. M., Ortiz J. L., Izquierdo J., Santos-Sanz P., Aceituno J., de Guindos E., Yanguas P., Palacian J., San Segundo A., and Avila D. (2021). "The Southwestern Europe Meteor Network: recent advances and analysis of bright fireballs recorded along April 2021". *eMetN Meteor Journal*, **6**, 397–406.

Madiedo J. M., Ortiz J. L., Izquierdo J., Santos-Sanz P., Aceituno J., de Guindos E., Yanguas P., Palacian J., San Segundo A., Avila D., Tosar B., Gómez-Hernández A., Gómez-Martínez J., and García A. (2022). "The Southwestern Europe Meteor Network: development of new artificial intelligence tools and remarkable fireballs observed from January to February 2022". *eMetN Meteor Journal*, **7**, 199–208.

Ortiz J. L., Madiedo J. M., Morales N., Santos-Sanz P. and Aceituno F. J. (2015). "Lunar impact flashes from Geminids: analysis of luminous efficiencies and the flux of large meteoroids on Earth". *Monthly Notices of the Royal Astronomical Society*, **454**, 344–352.

Segon D., Andreic Z., Korlevic K., Novoselnik F., Vida D. and Skokic I. (2013). "8 new showers from Croatian Meteor Network data". *WGN, Journal of the International Meteor Organization*, **41**, 70–74.

Contributors:

- Aceituno J.
- Aimee A.I.
- Ávila D.
- Baggaley J.
- Barbieri L.
- Breukers M.
- Campell-Burns P.
- Cooper T.
- de Guindos E.
- Devillepoix H.
- Garcia A.
- Gómez-Hernández A.
- Gómez-Martínez J.
- Holman D.
- Izquierdo J.
- Jenniskens P.
- Johannink C.
- Koseki M.
- Madiedo J.M.
- Moskovitz N.
- Odeh M.
- Ortiz J.L.
- Pilorz S.
- Roggemans P.
- Rollinson D.
- Samuels D.
- San Segundo A.
- Santos-Sanz P.
- Scott J.
- Tosar B.
- Verbelen F.